INFRARED APERTURE SYNTHESIS IMAGING OF CLOSE BINARY STARS WITH THE IOTA

A Thesis Presented

by

STEFAN KRAUS

Submitted to the Graduate School of the
University of Massachusetts Amherst in partial fulfillment
of the requirements for the degree of

MASTER OF SCIENCE

Revised Edition February 2004

Department of Astronomy

DEDICATION

Gewidmet

meiner Mutter

Dedicated

to my Mother

INFRARED APERTURE SYNTHESIS IMAGING OF CLOSE BINARY STARS WITH THE IOTA

A Thesis Presented

by

STEFAN KRAUS

Approved as to style and content by:

F. Peter Schloerb, Chair

Ronald Snell, Member

Grant Wilson, Member

Ronald Snell, Department Head
Department of Astronomy

ACKNOWLEDGMENTS

Above all, I would like to thank my supervisor "PETE" SCHLOERB who introduced me into the whole subject from the very basics. With his pleasant nature, he was always available to give encouragement and advice which is especially noteworthy since he's involved in a much larger project. Thanks also for reading this thesis and giving constructive suggestions for improvements!

This work would have been impossible without the excellent condition of the IOTA facility. So my tribute to the whole IOTA team!

The complete crew of the astronomy department was very hospitable over the year covering my work. Graduate Director JOHN KWAN was very keen to help me hurdle all bureaucratic obstacles for my graduation. My special thanks to him and the entire faculty. An important part of the vital life in the department are the graduate students who are always good for social activities. Last but not least, best thanks to them for making my stay such as pleasant!

This work was financially supported by NSF grant AST-0138303.

ABSTRACT

INFRARED APERTURE SYNTHESIS IMAGING OF CLOSE BINARY STARS WITH THE IOTA

SEPTEMBER 2003

STEFAN KRAUS, VORDIPLOM, RUPRECHT-KARLS-UNIVERSITÄT HEIDELBERG

M.S., UNIVERSITY OF MASSACHUSETTS AMHERST

Directed by: Professor F. Peter Schloerb

We present the first aperture synthesis maps from the *Infrared Optical Telescope Array* (IOTA) atop Mt. Hopkins, Arizona. During observation runs in November 2002 and March 2003 PETER SCHLOERB and myself obtained interferograms of the close binary systems Capella (α Aur) and λ Vir in the H band. This work covers the whole data reduction process from the raw data to the final maps including different algorithms for visibility and closure phase estimation. A special instrumental effect in our data required the use of advanced methods for visibility estimation which led to the implementation of a method based on the continuous wavelet transformation and to the development of a new fringe envelope fitting algorithm. The results confirm the overall stability and performance of the IOTA facility.

We fitted models of binary stars with uniform disks to our data and were able to track the movement of the Capella giants over the 14° arc covered by the observed five days in November 2002 with a precision better than one mas. Together with the data from March 2003 we confirm the orbit published by (Hum94) and derived uniform disk diameters $D_{Aa} = (8.4 \pm 0.2)$ mas; $D_{Ab} = (6.3 \pm 0.7)$ mas and the intensity ratio of the components to be $(I_{Ab}/I_{Aa})^{\text{H band}} = (1.44 \pm 0.23)$. Using additional information from the literature, we derived the effective temperatures $T_{Aa} = (5020^{+100}_{-90})$ K, $T_{Ab} = (5730^{+220}_{-180})$ K for the G8 III and G1 III component. For λ Vir we measured the positions of the unresolved components and determined the intensity ratio to be $(I_B/I_A)^{\text{H band}} = (2.1 \pm 0.2)$.

Aperture synthesis maps of Capella and λ Vir were produced using both the *conventional hybrid mapping* and *difference mapping* imaging strategies. To obtain a superior coverage of the uv plane we performed a

coordinate transformation which compensates the orbital motion of the Capella components. The produced maps confirm the results from the model fits and converge independently from any model with a resolution of 5 mas and better.

Contents

List of Figures

List of Tables

Chapter 1

Introduction

1.1 Historical Remarks

In the history of astronomy, progress has often been driven by revolutions in instrumentation. It is assumed that the telescope was invented in the Netherlands in the early 17th century. The first patent application for a telescope with lenses by HANS LIPPERHEY is dated on October 1608. GALILEO GALILEI (1564-1642) used such a telescope and published important observations, which were interpreted as strong evidence for the revolutionary Copernican system. JAMES GREGORY (1638-1675) designed a new type of telescope which used a mirror instead of lenses, and a few years later SIR ISAAC NEWTON (1642-1727) built the first of those reflector telescopes. Reflecting telescopes may be built with much larger aperture, which results in a larger light collecting area so that fainter objects may be observed. Moreover the aperture defines the ultimate angular resolution θ of a single telescope. Observing at a wavelength λ with a telescope of diameter D, the effect of diffraction limits the resolution to the RAYLEIGH criterion (BelTh)

$$\theta = 1.22\lambda/D \tag{1.1}$$

Currently, the largest optical telescopes have segmented mirrors with diameters D of 10.0m (Keck twins, Mouna Kea, Hawaii) or monolithic mirrors with 8.2m (VLT, Cerro Paranal, Chile).

Usually, the aperture is not the limiting factor for the angular resolution of a ground-based telescope. Most telescopes are limited by the atmospheric conditions. The terrestrial atmosphere consists of a turbu-

lent mixture of regions with different temperatures and densities. This structure is primarily induced by the cycle of day-night and heating from the ground, and since the refractive index of the atmosphere depends on its temperature, star light passing through the atmosphere suffers random scattering which distorts the stellar image. The random nature of this *seeing* effect produces a Gaussian distributed "seeing disk" which is determined by a characteristic scale r_0 over which the incoming wave front suffers no distortion. This *coherence radius* r_0 shows a dependence $r_0 \sim \lambda^{6/5}$ on the wavelength (Pan98). There is also a *coherence time* t_0 for which the temporal changing variations can be assumed to be "frozen". (Bus88) gives typical values of $t_0 = 10$ms and $r_0 = 10$cm for the V band.

Following (Pan98), the seeing ε depends on r_0 as $\varepsilon = 0.98\lambda/r_0$, so even under excellent conditions, the seeing spreads the image of a point source in the optical to more than 1.1" typically. Therefore, great efforts have been taken to reduce the influence of the atmosphere. In 1970, a first success was reached by ANTOINE LABEYRIE with the method of Speckle interferometry. Later this method was improved in the KNOX-THOMPSON-method and in Speckle Masking Interferometry. Those speckle techniques use extremely short integration times to "freeze" the atmospheric turbulence, thus limiting the sensitivity of this method for imaging. Later, accompanied to the technological progress, adaptive optics (AO) systems were built to remove atmospheric wave front distortion through the use of simple tip-tilt mirrors as well as more complex systems using deformable mirrors. The use of AO systems allows the full sensitivity of a telescope to be achived and these systems have now pushed the resolution of ground-based telescopes even to the diffraction limit as demonstrated by VLT-MACAO (Hub03) most recently. However, even in the long term there are no concepts for single-dish-telescopes larger than 100m (see OWL design study). Therefore, a conceptual turn has to be taken to gain further resolution in optical astronomy.

In 1868, ARMAND FIZEAU (1819-1896) suggested an interferometric method to measure stellar diameters by placing a mask with two holes in front of a telescope's aperture. In 1872 and 73, first observations by EDOUARD STÈPHAN with the 80cm reflector at the Observatoire de Marseille obtained an upper limit of $0.158''$ for the diameter of stars (Qui01). ALBERT ABRAHAM MICHELSON (1852-1931) was the first who succeded using interferometric methods for astronomical observations. Using the $12''$-telescope on Lick Observatory he measured the diameters of the Galilean satellites in 1891 (Mic1891). In 1919, he made the first measurement of the angular diameter of a star (Betelgeuse) with the Hooker Telescope on Mount Wilson Observatory (Rar). MICHELSON installed a 20-foot beam on top of the $100''$ telescope with two moveable, flat mirrors. The interferometric pattern (the *fringe*) had to be located by the observer manually. Then the

observer estimated the brightness of this pattern (the *visibility*). This procedure was repeated for different baselines. Finally the diameters of seven stars could be measured by MICHELSON and his collaborators.

The first interferometric observation of the close binary star Capella was made by JOHN AUGUSTUS ANDERSON in December 1919 (And20). Since the technological challenges to build larger optical interferometers were enormous, interferometry became more and more a branch of radioastronomy in the following decades. Those attempts in radioastronomy lead to the development of the intensity interferometry method by HANBURY BROWN and TWISS, which they also applied to optical wavelengths in 1974. In 1974, ANTOINE LABEYRIE succeeded in combining the light of two individual telescopes, spaced 12m apart.

Although optical interferometers may be built with large dimensions to achieve high resolution they still are affected by the earth's atmosphere. The path length through the atmosphere above each of the telescopes is constantly changing, which means that although the *amplitude* of the fringe pattern may be measured, it's *phase* is continually changing. This latter property is an essential part of making an image with an interferometer by the process known as "aperture synthesis". Thus, two telescope optical interferometers are insufficient to carry out imaging experiments. Fortunately, developments of the radio VLBI community showed that a third telescope in the configuration could yield sufficient new information to make an image, and these techniques known collectively as *Hybrid mapping* are now being adapted to optical interferometry.

The first image of the surface of a star was made in 1990 when DAVID BUSCHER et al. (Bus90) presented the first surface map of Betelgeuse. Another important milestone was achieved in 1995, when JOHN BALDWIN et al. presented the first optical aperture synthesis map using Capella as the target (Bal96). Those observations were done with the *Cambridge Optical Aperture Synthesis Telescope (COAST)* at $\lambda = 830$nm. The longest baseline for this measurement was 6.1m. Four years later, JOHN S. YOUNG presented an infrared ($\lambda = 1.3\mu$m) map of Capella in his dissertation (You99).

Long baseline interferometry continues to be a very active field with many new instruments coming online. For this thesis we attempt to achieve the new milestone of creating an aperture synthesis image of Capella with the *Infrared Optical Telescope Array (IOTA)*.

1.2 Outline of my thesis

In 1988, the Smithsonian Astrophysical Observatory (SAO), Harvard University, the University of Massachusetts (UMass), the University of Wyoming and MIT/Lincoln Laboratory came to the agreement to build a two-telescope Michelson interferometer with a maximum baseline of 38m. The *Infrared Optical*

Telescope Array (IOTA) observed first stellar fringes in December 1993. In 2000 a third telescope completed the current configuration of IOTA on top of Mount Hopkins, Arizona.

IOTA is one of the few facilities with aperture synthesis capabilities in the near infrared. However, as of this writing, no aperture synthesis image has been created with this instrument. The goal of my thesis is to develop a data reduction procedure which gives IOTA those imaging capabilities. To do this, it is important initially to observe target stars with well known properties such that the final results could be validated with earlier observations. We decided to choose Capella as our primary target. The orbit of this binary is very well known (Hum94) and as mentioned earlier there is already a map by COAST (You99). On the other hand, Capella is more resolved by our interferometer than in any previous synthesis aperture observations making the final image potentially useful once the performance of this instrument is understood.

This thesis is structured as follows: After the introductory remarks of this chapter, we describe the basic principles of long baseline interferometry in chapter 2 briefly. Chapter 3 gives an overview of the technical design of the IOTA observatory and connects the theory of the interferometer to the IOTA facility.

We obtained data on the IOTA site in two observation runs in November 2002 and March 2003, each lasting one week. In chapter 4 we report details of those runs and the observed targets. Chapter 5 contains the main part of my work, which is a data reduction procedure to extract the two most important interferometric quantities from the IOTA-scans: The contrast of the fringe pattern (the *visibility*) and the atmosphere invariant *closure phase*. For the visibility estimation, three different methods are examined: One algorithm is based on the fitting of the fringe envelope to the data in the time domain, another on the fitting of the fringe power in frequency space and the third on the measurement of the power in the continuous wavelet transform (CWT) of the data.
In chapter 6 and 7 we interpret those measured quantities scientifically, first by fitting binary star models to the data and then by generating a model independent hybrid map. The thesis closes with some remarks on the performance of the IOTA facility in chapter 8 and our conclusions (Chapter 9).
Two appendices contain the detailed observation logs and a short manual for the implementation of my data reduction software followed by the bibliography.

All computations were carried out with stand-alone applications, written in C and compiled with gcc-linux. For graphical visualizations during the computation process PGPLOT was implemented. Fast Fourier transforms were calculated using FFTW. More details about the applications can be found in Appendix B. The graphics presented in this thesis were generated with SM, XFig and Matlab. The document itself was prepared using LaTeX.

Chapter 2

Theory of Long Baseline Interferometry

2.1 Basics of Interferometry

We understand light as an electromagnetic wave propagating according to the laws of classical electrodynamics. The most fundamental equations in electrodynamics are the MAXWELL equations, from which one can derive the HELMHOLTZ wave equation (Weg03). One solution for this equation is the monochromatic, time-independent planar wave $\Psi(\vec{x})$. Adopting the formalism of (Lüh01), the propagation of this planar wave through the source-free vacuum can be expressed as

$$\psi(\vec{x},t) = \Psi(\vec{x})e^{-\imath(ckt+\phi)} \tag{2.1}$$

with the *wave number k* and the relation $k = 2\pi\nu/c = 2\pi/\lambda$ where c denotes the speed of light in the vacuum, ν is the frequency and λ the wavelength. ϕ is the *phase* of the wave.

With optical detectors we measure not ψ but the absolute square of this complex wavefunction, which is the *intensity I* of the light:

$$I(\vec{x},t) = |\psi(\vec{x},t)|^2 \tag{2.2}$$

Therefore, the superposition of two electromagnetic waves $\psi_1(\vec{x_1},t_1)$ and $\psi_2(\vec{x_2},t_2)$ is given by the absolute value squared of the sum of both wave functions. Since every measurement needs a finite sampling time, we

have to average over a period much longer than the frequency of the wave, which gives

$$\begin{aligned} I_{12}(\vec{x}_1,\vec{x}_2,t_1,t_2) &= \langle|\psi_1(\vec{x}_1,t_1)+\psi_2(\vec{x}_2,t_2)|^2\rangle \\ &= \langle(\psi_1(\vec{x}_1,t_1)+\psi_2(\vec{x}_2,t_2))\,(\psi_1^*(\vec{x}_1,t_1)+\psi_2^*(\vec{x}_2,t_2))\rangle \\ &= \langle|\psi_1(\vec{x}_1,t_1)|^2\rangle+\langle|\psi_2(\vec{x}_2,t_2)|^2\rangle+2\Re\left(\langle\psi_1(\vec{x}_1,t_1)\psi_2^*(\vec{x}_2,t_2)\rangle\right) \\ &= I_1(\vec{x}_1,t_1)+I_2(\vec{x}_2,t_2)+2\Re\left(\langle\psi_1(\vec{x}_1,t_1)\psi_2^*(\vec{x}_2,t_2)\rangle\right) \end{aligned} \tag{2.3}$$

where ψ^* is the complex conjugate of ψ and $\Re(\psi)$ ($\Im(\psi)$) denotes the real (imaginary) part of this complex function. The last term $\langle\psi_1(\vec{x}_1,t_1)\psi_2^*(\vec{x}_2,t_2)\rangle =: \Gamma_{12}(\vec{x}_1,\vec{x}_2,t_1,t_2)$ is called the *mutual intensity* (Lüh01) or *mutual coherence function*. Using the assumption of a temporary stationary wave front we define $\Gamma_{12}(\vec{x}_1,\vec{x}_2,t_1,t_2) =: \Gamma_{12}(t_1-t_2)$. The mutual coherence function is useful as a measure of the coherence of the signal, but it is more convenient to use the *complex degree of coherence*

$$\gamma_{12}(t) := \frac{\Gamma_{12}(t)}{\sqrt{\Gamma_{11}(0)\Gamma_{22}(0)}} \tag{2.4}$$

This function is normalized on the intensity as demonstrated clearly in (Lüh01).

If the two waves are *uncorrelated*, γ_{12} will vanish. But when the two light waves are *coherent*, *interference* can be observed. This may happen in the case of self-coherence by superposing the same wave at different times. There are two different cases of self-coherence: For *temporal self-coherence* the same wave will interfere at the same place $x_1 = x_2$, but at different times t_1 and t_2. The other case is *spatial self-coherence*, where $t_1 = t_2$.

Spatial self-coherence is realized in YOUNG*'s double slit* experiment. This famous experiment has a special position in physics since it demonstrates the wave nature of light. Here it may be used to introduce the basic ideas of a MICHELSON Stellar Interferometer.

The basic setup of YOUNG's experiment is shown in figure 2.1. Let's consider a plane, quasi-monochromatic light wave which is incident from the direction of the unit-vector $\vec{r}$ on an opaque screen with two narrow slits in it. The width of the slits is assumed to be much smaller than the separation of the slits. The position of the slits is $\vec{x}_1$, $\vec{x}_2$ such that the separation can be expressed as $\vec{B} = \vec{x}_1 - \vec{x}_2$. Parallel to the opaque screen, a detector screen is mounted. From the principle of HUYGENS-FRESNEL it follows that behind the two slits, the electromagnetic wave will propagate as spherical waves.

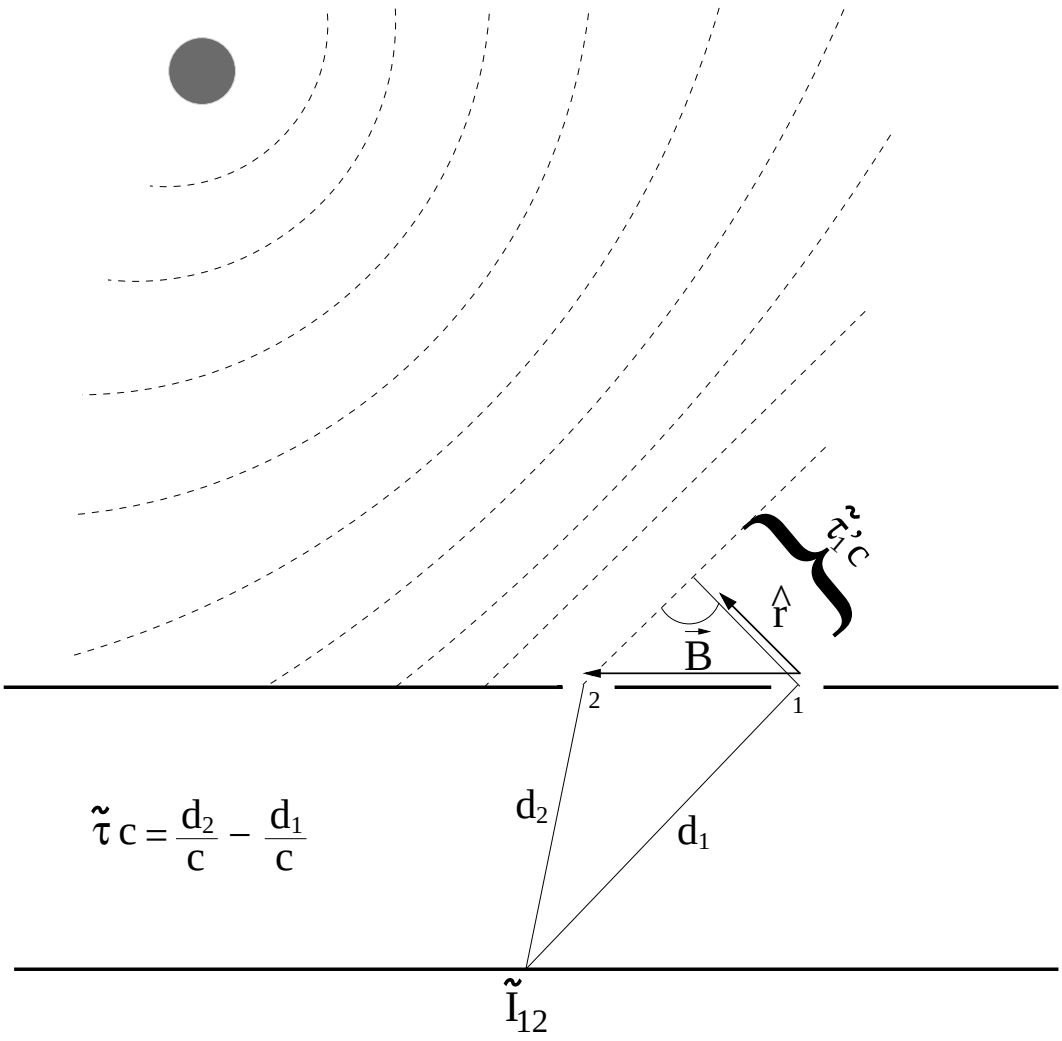

Figure 2.1: Setup of YOUNG's double slit experiment.

Assuming that the distance between the two screens is much larger than $|B|$, basic two-dimensional geometry lead to the relation

$$\vec{B}\vec{r}/c =: B_\perp/c =: \tilde{\tau}' \tag{2.5}$$

where $B_\perp$ is the *projected baseline* which can be also expressed using the zenith angle z as $B_\perp = |\vec{B}|\cos(z)$.

The wave front will reach the two slits at different times $\tilde{\tau}'_1$ and $\tilde{\tau}'_2$. After passing the slits, the rays will reach the detector screen with different path delays and intensities $\tilde{I}_1$ and $\tilde{I}_2$. The position on the screen can be expressed in term of an additional *optical path delay* $\tilde{\tau}$ so we define the *total path delay* $\tau := \tilde{\tau}'_2 - \tilde{\tau}'_1 + \tilde{\tau}$ for convenience.

Using (2.3), the measured intensity on the detector screen is

$$\begin{aligned}
\tilde{I}_{12}(\tau) &= \tilde{I}_1 + \tilde{I}_2 + 2\Re\left(\Gamma_{12}(\tau)e^{i\phi}\right) && (2.6)\\
&= \tilde{I}_1 + \tilde{I}_2 + 2\sqrt{\tilde{I}_1\tilde{I}_2}|\gamma_{12}(\tau)|\cos\phi && (2.7)\\
&= \tilde{I}_1 + \tilde{I}_2 + 2\sqrt{\tilde{I}_1\tilde{I}_2}\Re\left(e^{i(ck\tau-\phi)}\right) && (2.8)\\
&= \tilde{I}_1 + \tilde{I}_2 + 2\sqrt{\tilde{I}_1\tilde{I}_2}\cos(ck\tau-\phi) && (2.9)
\end{aligned}$$

Obviously, the pattern on the detector screen is a cosine *fringe* pattern whose frequency is inversely proportional to the wavelength of the incident frequency.

To separate the varying term in equation (2.9), we define the response R as in (BelTh)

$$R = \frac{\tilde{I}_{12}(\tau) - \tilde{I}_1 - \tilde{I}_2}{2\sqrt{\tilde{I}_1\tilde{I}_2}} = \cos\left(2\pi\nu\tau - \phi\right) \tag{2.10}$$

All concepts introduced in this section for the double slit hold for a Michelson Stellar Interferometer as well. Figure 2.2 shows that the two telescopes take the position of the slits and the light is not projected on a screen but combined in a beam combiner in this configuration. Technical details will be discussed in chapter 3. In the next section the response for a non-monochromatic light will be calculated.

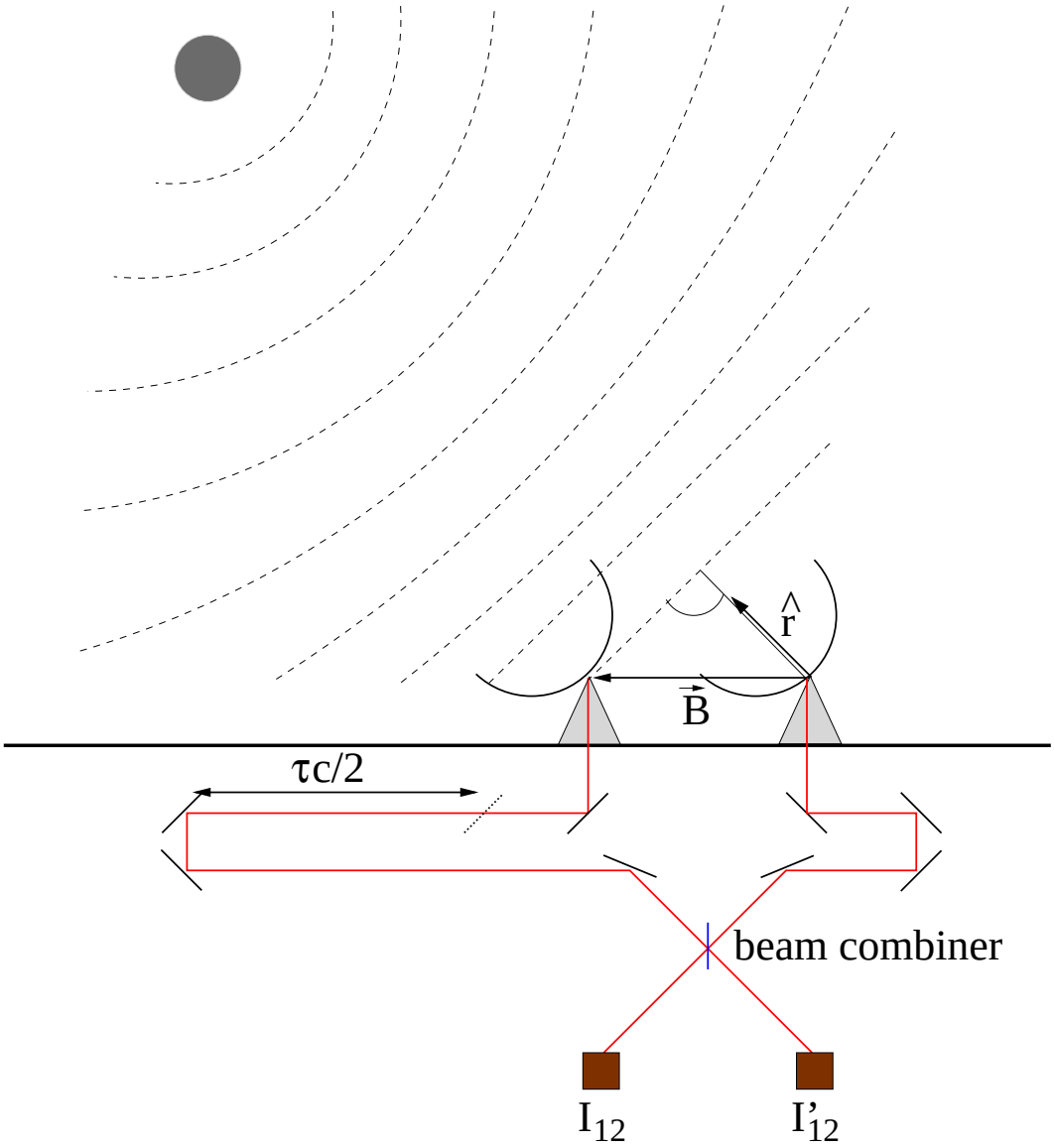

Figure 2.2: A MICHELSON stellar interferometer with a beam combiner (blue) and two detectors (brown).

2.2 Effect of Spectral Bandwidth Filters

Since astronomical objects radiate over a broad range of the electromagnetic spectrum, it is necessary to generalize the results from the last section for non-monochromatic light. To obtain a well defined frequency range it is common to use standardized bandwidth-filters which have a rectangular shape in the ideal case. Let's define the rectangular filter with

$$F(\nu) = \begin{cases} 1 & : \quad \nu_0 - \frac{\Delta\nu}{2} < \nu < \nu_0 + \frac{\Delta\nu}{2} \\ 0 & : \quad \text{otherwise} \end{cases} \tag{2.11}$$

So we can just average the response over the bandwidth of F as the transmission function

$$\begin{aligned} R_F &:= \frac{\int_{-\infty}^{\infty} RF\,d\nu}{\int_{-\infty}^{\infty} d\nu} \\ &= \frac{1}{\Delta\nu}\int_{\nu_0-\frac{\Delta\nu}{2}}^{\nu_0+\frac{\Delta\nu}{2}} R d\nu \\ &= \frac{1}{2\pi\Delta\nu\tau - \phi}\sin(2\pi\nu\tau - \phi)\Big|_{\nu_0+\frac{\Delta\nu}{2}}^{\nu_0-\frac{\Delta\nu}{2}} \\ &= \cos(2\pi\nu_0\tau - \phi)\,\frac{1}{\pi\Delta\nu\tau - \phi}\,\sin(\pi\Delta\nu\tau - \phi) \\ &\equiv \cos(2\pi\nu_0\tau - \phi)\,\mathrm{sinc}(\pi\Delta\nu\tau - \phi) \end{aligned} \tag{2.12}$$

With this filter, the fringe will show a $\cos(\tau)$ modulation and a $\mathrm{sinc}(\pi\Delta\nu\tau)$ *envelope*. The envelope is symmetric around $\pi\Delta\nu\tau = \phi$. By measuring the amplitude and position of this central *white light fringe* the visibility and the phase can be obtained directly in principle. The white light fringe is defined as the fringe whose phase is independent of wavelength.

2.3 Two Sources and the Bandwidth Smearing Effect

Now we may introduce a second source. The intensities of the rays I_1 and I_2 which are incident from different directions $\hat{r}_1$, $\hat{r}_2$ may be different as well. With this setup we have two different total path delays τ_1 and τ_2 which means when we sum the resulting responses $R_{F,1}$ and $R_{F,2}$ together

$$R_{F,12} = I_1\cos(2\pi\nu_0\tau_1 - \phi_1)\,\mathrm{sinc}(\pi\Delta\nu\tau_1 - \phi_1) + I_2\cos(2\pi\nu_0\tau_2 - \phi_2)\,\mathrm{sinc}(\pi\Delta\nu\tau_2 - \phi_2) \tag{2.13}$$

a) Unresolved Binary
($I_1 = 2I_2$)

b) Completely Resolved Binary
($I_1 = I_2$)

c) The Bandwidth Smearing Effect
($I_1 = 2I_2$)

d) Two Fringes
($I_1 = 2I_2$)

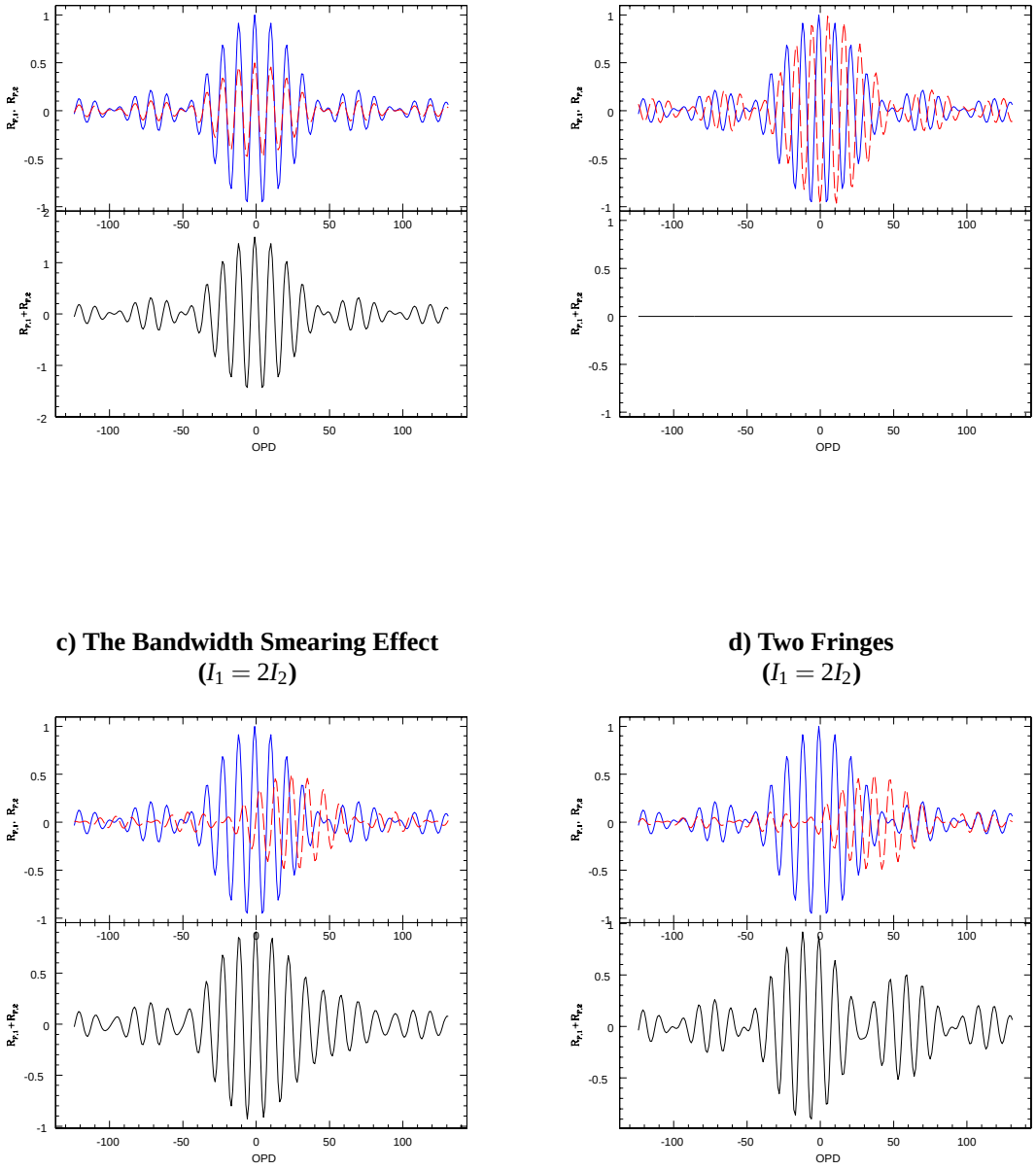

Figure 2.3: Simulated Responses for binary sources with different separations *s* (*s* is increasing from the upper left to the lower right). The individual fringe packages (red and blue) are shown in the upper part of each plot.

we will get the superposition of two white light fringes which are shifted against each other. Neglecting the shift due to the phase difference $\phi_{ij} := \phi_i - \phi_j$ for a moment, we can examine the dependence of $R_{F,12}$ on the angular separation of the two sources $s := \cos^{-1}(\vec{r}_1\vec{r}_2)$. As soon as $B_\perp \cos(s)$ becomes comparable to k^{-1} (making the assumption that $s \ll 1$ such that $B_{\perp,1} = B_{\perp,2} \equiv B_\perp$), the two fringe packages will come out of phase so they don't add up perfectly any more. For $B_\perp \ll k$, the source is *unresolved* (see figure 2.3 a)), otherwise it is *resolved*. So we obtain an equation comparable to (1.1) using the estimation $Bk\cos\theta \approx 1$

$$\theta \sim \lambda/B \tag{2.14}$$

With the phase difference $\Delta\tau = \tau_2 - \tau_1 = 2\pi$ and $I_1 = I_2$, the source will be completely resolved as shown in figure 2.3 b). When the difference exceeds 2π significantly, an effect called *Bandwidth Smearing* can be observed: The envelope of the resulting fringe package may be deformed significantly. By increasing $\Delta\tau$ even more, two separate fringe packages can be observed (see figure 2.3 d)).

From equation (2.14) one may deduce the two common ways to improve the *resolution* θ of a Michelson Interferometer: The baseline can be increased and/or a shorter wavelength can be chosen.

2.4 Interferometric Observables

Since the response in (2.13) can vary only in a certain range we may specify the borders of this range: $R_{min} = \min(R_{F,12}(\tilde{\tau}))$ and $R_{max} = \max(R_{F,12}(\tilde{\tau}))$. Finally, the *fringe contrast* or *visibility* is defined as

$$V = \frac{R_{max} - R_{min}}{R_{max} + R_{min}} \tag{2.15}$$

The case with the lowest visibility can be reached by $I_1 = I_2 = I$ such that $0 \leq V \leq 1$. On the other hand is $V = 1$ for an unresolved source.

With the definition of (2.15), we neglect the phase ϕ_{21} which obtains additional information about the source. Therefore it is common to define the *complex visibility*

$$\mathbb{V} = Ve^{i\phi_{21}} \in \mathbb{C} \tag{2.16}$$

Using this elegant formalism, the visibility V is just given by the length of the vector in the complex plane $V = |\mathbb{V}|$ while the phase is $\phi_{21} = \tan^{-1}(\Re(\mathbb{V})/\Im(\mathbb{V}))$. A very useful property of this formalism is it's

additivity.

2.5 The VAN-CITTERT-ZERNIKE Theorem

The VAN-CITTERT-ZERNIKE theorem (Sha92) relates the complex visibility to the Fourier transform $\mathcal{F}()$ of the irradiance distribution and vice versa

$$\mathbb{V}(u,v) = \int_{-\infty}^{\infty} I(x,y) e^{-\imath k(ux+vy)} dxdy =: \mathcal{F}(I(x,y)) \tag{2.17}$$

The new coordinates are in frequency space and are defining the uv-plane, where u is the projection of $B_\perp$ onto the x axis and v is the projection of $B_\perp$ onto the y axis and (u,v) are measured in meters.

2.6 Closure Relations

Due to corruption of the signal by the atmosphere, the phases cannot be measured directly from the ground. ROGERS proposed in 1974 (Weiss) to use the simultaneous phase-measurements of three or more telescopes to obtain the *Closure Phase* Φ. Φ is invariant under all atmospheric disturbance as the following considerations show.

Using N telescopes for a observation will result in $N(N+1)/2$ baselines and the same number of measured visibilities and phases. But the disturbance of the atmosphere on those baselines is not independent. Each telescope X may be affected by an arbitrary atmospheric *piston* which can be described as an additional delay ζ_X. Considering the case with $N = 3$, the measured phase φ_{XY} between telescope X and Y becomes

$$\begin{aligned} \varphi_{AB} &= \phi_{AB} + \zeta_A - \zeta_B \\ \varphi_{BC} &= \phi_{BC} + \zeta_B - \zeta_C \\ \varphi_{CA} &= \phi_{CA} + \zeta_C - \zeta_A \end{aligned} \tag{2.18}$$

But the closure phase computed from the measured phases is independent of ζ_X as in

$$\Phi = \varphi_{AB} + \varphi_{BC} + \varphi_{CA} \tag{2.19}$$

$$= \phi_{AB} + \phi_{BC} + \phi_{CA} \tag{2.20}$$

where the sign convention is that the baseline vectors close a triangle or loop (see figure 2.4). A necessary assumption is that this measurement is done within a time interval smaller than the actual coherence time of the atmosphere so that the phase of the fringe is well defined (see chapter 1). For an array of N telescopes, $(N-1)(N-2)/2$ closure phases may be defined which contain a fraction $(N-2)/N$ of the complete phase information (BelTh). For $N > 3$ an *Amplitude Closure Relation* can be obtained to place constraints on the measured visibility amplitudes as well.

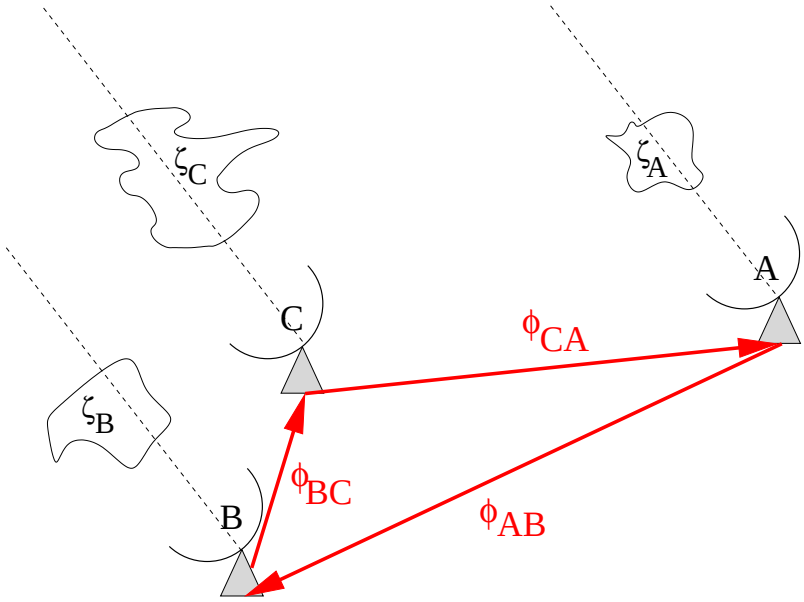

Figure 2.4: Defi nition of the vector directions in the closure phase triangle.

2.7 Fundamentals of Modelling

It is of practical benefit to derive the visibility and phase functions of simple brightness distributions analytically. Those functions may be used later to fit models to the measured data. It was shown in section 2.1 that for a point source $V = 1$ and $\Phi = 0$.

2.7.1 Model of a Uniform and Limb-darkened Disk

Equation (2.17) can be used to calculate the visibility function for a disk with radius $\Theta = D/2$ and a uniform brightness distribution I. To simplify the calculations let's assume a circular stellar disk even if this may be an inadequate assumption for some rapidly rotating stars (deS03). A parameterization in spherical coordinates

leads to

$$\begin{aligned}
\mathbb{V}_{UD}(\Theta) &= \int_{-\Theta}^{\Theta}\int_{0}^{\pi} I(r,\vartheta)e^{\imath krB_\perp\cos\vartheta}rdrd\vartheta \\
&= 2I_{UD}\int_{0}^{\Theta}\int_{0}^{\pi} e^{\imath krB_\perp\cos\vartheta}rdrd\vartheta \\
&= 2\pi I_{UD}\int_{0}^{\Theta} J_0(rkB_\perp)rdr \\
&= \frac{2\pi I_{UD}}{B_\perp^2k^2}\int_{0}^{k\Theta B_\perp} zJ_0(z)dz \\
&= I_{UD}2\pi\Theta^2\frac{J_1(k\Theta B_\perp)}{k\Theta B_\perp}
\end{aligned} \tag{2.21}$$

with the BESSEL functions of first kind and zeroth (J_0) and first order (J_1). I_{UD} is the intensity integrated over the whole disk. Taking the real part (BelTh) and doing the normalization lead to

$$V_{UD}(\Theta) = 2\frac{J_1(k\Theta B_\perp)}{k\Theta B_\perp} \tag{2.22}$$

Of course, the simplification that $I(r,\vartheta)$ doesn't depend on the radius r is unrealistic since most stars are expected to be limb darkened. Thus a correction for the limb darkening is often applied to the fitted stellar radii to get the limb darkened diameter Θ_{LD} of a star. The exact value of this correction factor $\rho = \Theta_{LD}/\Theta$ depends strongly on the used stellar model so that this problem cannot be solved analytically. (Dav00) presents a useful correction diagram based on models for five different stellar surface temperatures. For the H-band this correction factor lies between $1.01 < \rho < 1.03$.

There are also empirical approaches like the MICHELSON-PEASE limb darkening function (BelTh) which express the intensity over a spherical star disk with radius Θ as function of the radius r

$$\frac{I(r/\Theta)}{I(0)} = \left[1-\left(\frac{r}{\Theta}\right)^2\right]^\xi \tag{2.23}$$

It is shown (Hes97) that this powerlaw results in the following visibility function

$$V_{LD}(\Theta) = \Gamma(\xi-1)2^\xi\frac{J_1(k\Theta B_\perp)}{(k\Theta B_\perp)^\xi} = \Gamma(\xi-1)\left(\frac{2}{k\Theta B_\perp}\right)^{\xi-1}V_{UD}(\Theta) \tag{2.24}$$

which can be fitted to visibility curves.

2.7.2 Model of a Binary Star

A very useful property of Fourier space is it's additivity. So V and Φ can be easily derived even for a binary system with resolved uniform disks.

Let's consider a binary system with two resolved uniform bright disks and angular radii Θ_1, Θ_2. The separation of the two components may be s and the position angle β. It is reasonable to choose for the origin of the coordinate system the "center of light" of the sources with the brighter (primary) component closer to the origin. So the distances to the origin become

$$r_1 = s\frac{I_2}{I_1+I_2} \tag{2.25}$$

$$r_2 = s\frac{I_1}{I_1+I_2} \tag{2.26}$$

Now we transform to the Cartesian coordinate system

$$\vec{x}_1 = r_1\begin{pmatrix}\cos\beta\\ \sin\beta\end{pmatrix} \qquad \vec{x}_2 = r_2\begin{pmatrix}\cos(\beta+\pi)\\ \sin(\beta+\pi)\end{pmatrix} \tag{2.27}$$

this gives the visibility

$$\mathbb{V}(\vec{x}_1,\vec{x}_2) = \frac{1}{I_1+I_2}\left(\mathbb{V}(\Theta_1)I_1 e^{-ik\vec{B}\vec{x}_1} + \mathbb{V}(\Theta_2)I_2 e^{-ik\vec{B}\vec{x}_2}\right) \tag{2.28}$$

Now it is straight forward to show that

$$V^2(\vec{x}_1,\vec{x}_2) = V^2(\Theta_1) + V^2(\Theta_2) + 2V^2(\Theta_1)V^2(\Theta_2)\cos(k\vec{B}(\vec{x}_2-\vec{x}_1)) \tag{2.29}$$

For the measured closure phase one can derive analogous

$$\Phi(\vec{x}_1,\vec{x}_2) = \tan^{-1}\left(\sum_{XY=\{AB;BC;CA\}}\frac{I_1\cos(k\vec{B}\vec{x}_1)+I_2\cos(k\vec{B}\vec{x}_2)}{I_1\sin(k\vec{B}\vec{x}_1)+I_2\sin(k\vec{B}\vec{x}_2)}\right) \tag{2.30}$$

For unresolved stars the intensity ratio of a binary star can be calculated from the visibility extrema (see (BelTh))

$$\frac{I_1}{I_2} = \frac{1+V_{min}}{1-V_{min}} \tag{2.31}$$

2.8 Fundamentals of Mapping

In principle, the VAN-CITTERT-ZERNIKE theorem (2.17) can be inverted to obtain the source intensity distribution on the sky. However, in practice the map that is produced depends on the sampling of the uv-plane that is made during data collection. We may define the *dirty map* to be

$$I(x,y) = \int_{-\infty}^{\infty} S(u,v)\mathbb{V}(u,v)e^{ik(ux+vy)}dudv =: \mathcal{F}^{-1}(S * \mathbb{V}) \tag{2.32}$$

where $S(u,v)$ is the sampling function which expresses the coverage of the uv-plane for a particular set of observations. We can use the Kronecker δ-function to define S in terms of the (u,v)-coordinates of the i'th of n observations

$$S(u,v) = \sum_{i=1}^{n} \delta(u-u_i)\delta(v-v_i) \tag{2.33}$$

Beside the observed points of the uv-plane one may use the fact that the Fourier transform of the sky brightness distribution (as a real function) is hermitian ($\mathbb{V}(-u,-v) = \mathbb{V}^*(u,v)$) from which follows $V(u,v) = V(-u,-v)$. Since the dirty map is a convolution of the real source distribution with the instrument response, we have to make a deconvolution with the Fourier transform of the sampling distribution defined as the *dirty beam*

$$DB = \mathcal{F}^{-1}(S) \tag{2.34}$$

The *dirty map* is then given by

$$DM = CM * DB = \mathcal{F}^{-1}(S * \mathbb{V}) \tag{2.35}$$

so a deconvolution will reconstruct the desired *clean map CM*. Those relations are discussed in more detail in (Sch93).

2.8.1 Rotation-Compensating Coordinate Transformation

To obtain a better uv-plane coverage on a binary system with known orbit one may rotate and contract/expand the (u,v) coordinates in such a way that the movement of the binary components is compensated. Therefore one has to choose an arbitrary reference position. To keep the correction small we used the position of the components at the medial time t_{ref} of the observed binary orbit arc as reference point (with separation $s(t_{ref})$ and position angle $\beta(t_{ref})$). Then the transformation from (u,v) to the corrected (u',v') coordinates is

performed in spherical coordinates

$$\begin{aligned} \alpha(t) &= \tan^{-1}(u(t)/v(t)) \\ \begin{pmatrix} u'(t) \\ v'(t) \end{pmatrix} &= B_{\perp} \frac{s(t)}{s(t_{ref})} \begin{pmatrix} \sin(\alpha(t) - [\beta(t) - \beta(t_{ref})]) \\ \cos(\alpha(t) - [\beta(t) - \beta(t_{ref})]) \end{pmatrix} \end{aligned} \tag{2.36}$$

Chapter 3

IOTA Design

Figure 3.1: The Infrared Optical Telescope Array at FRED WHIPPLE Observatory.

The Infrared Optical Telescope Array (IOTA) is located at FRED WHIPPLE Observatory at an elevation of 2,564m (Tra01) atop Mount Hopkins, Arizona. In it's current configuration, there are three telescopes which can be moved on an L-shaped track with 15m and 35m long arms. The shorter arm is oriented to the south-east and carries telescope B. Perpendicular to that, telescope A can be moved along the 35m north-east base-

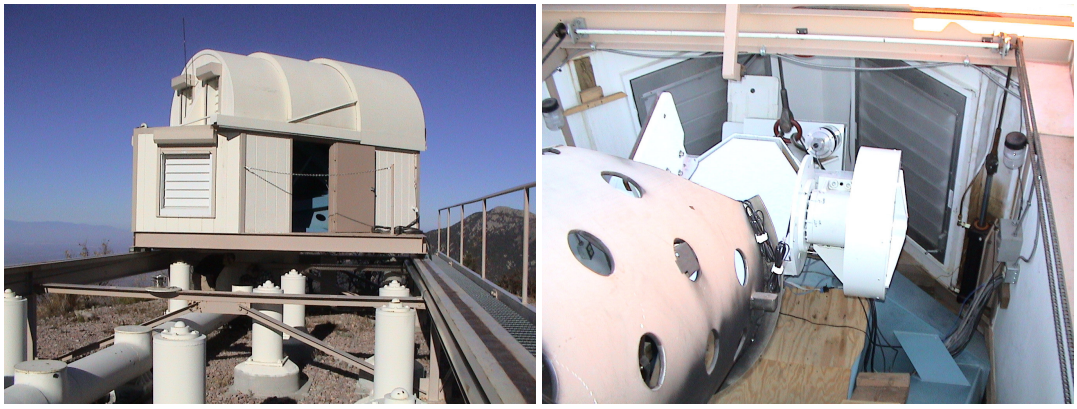

Figure 3.2: *Left:* The dome of telescope A in closed position. *Right*: The siderostat which feeds the CASSEGRAIN optics (the tube to the left).

line. The third telescope C can be mounted on each of the stations along the north-east baseline. The spacings between those stations are multiples of 197 inches (= 5.0038m) and 277 inches (= 7.0358m) (Col99), the length of a IOTA-baseline can be varied between 5m$\leq B_{XY} \leq$ 38m. Normally one refers to the position of the telescopes in a rough notation where the position of the telescopes is given in meters on each track (e. g. $A = ne35, B = se15, C = ne10$ is the configuration shown in figure 3.1). To define the baselines more precisely it is necessary to fit the baseline vectors $\vec{B}_{XY} = x_X - x_Y$ for $(X,Y) = \{(A,C);(B,C);(A,B)\}$ to a large number of measured delay line offsets (Col99).

The telescopes themselves are CASSEGRAIN telescopes with parabolic f/2.5 45cm primary mirrors which are fed by 45x86cm siderostats under an angle of 30°. The 10x focused parallel beam which leaves the CASSEGRAIN optics passes a flat mirror whose alignment is controlled by a star tracker. Once the loop of the star tracker is closed, this tip-tilt adaptive optics uses piezo motors to compensate the atmospheric induced motion of the image with a frequency comparable to $1/t_0$. Beside that, it is possible to flip a mirror in the beam to feed a wide-field (20′) CCD TV-camera whose image can be used for star acquisition.

Next the beam enters an evacuated pipe which contains the two *long delay lines* (each 28m long). For telescope C the beam passes the feed and corner mirror and enters the *long delay 2* (LD2) from which it is directed by the exit mirror towards the optical table. The beam from telescope A and B passes the same configuration of mirrors but the observer may choose which of these is delayed by *long delay 1* (LD1). The configuration with telescope A fixed and telescope B on LD1 is refered to as the *South Delayed Case*

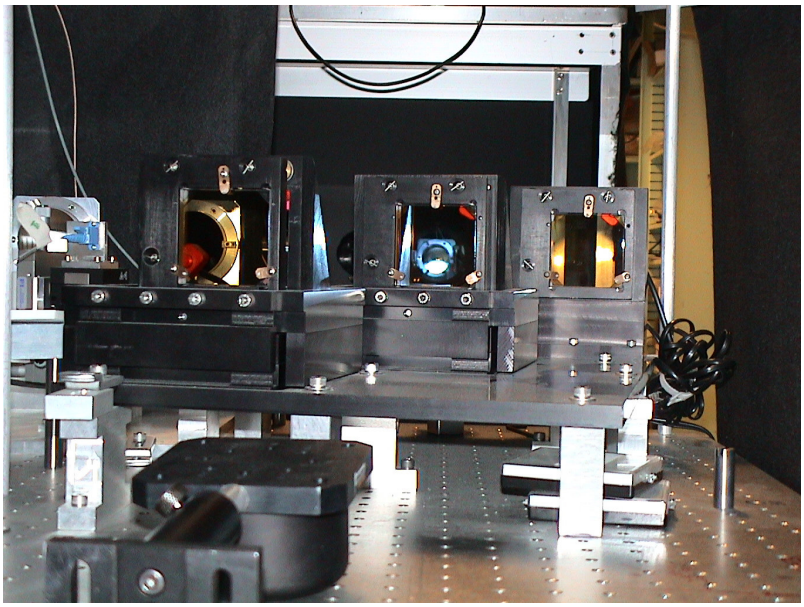

Figure 3.3: The beam splitter as seen from the tubes where the beam is leaving the vacuum tanks. The three beam-splitters deflecting the infrared part of the beam to the mirrors on the left where the light is coupled into fibers. Through the beam-splitter in the middle we see one of the three mirrors which are deflecting the visual light into the star trackers.

otherwise it is the *North Delayed Case*. The tracking of the long delays is controlled by the software automatically (Tra00). Behind the long delays are two short delay lines (SD1, SD2) in the optical path. They are used to scan carefully through the optical path delay and to locate the fringes. Using the notation from chapter 2, τ is the delay containing external as well as internal delays. $\tilde{\tau}$ is then going to be adjusted with LD1/LD2 and SD1/SD2 in order to locate the white light fringe at $\tau = 0$.

On the optical table, a beam-splitter separates the visual and infrared components of the beam (see figure 3.3). The visual light passes the beam-splitter and is finally focused on three different quadrants of the 32x32 pixel-CCD-chip of the star tracker. The infrared component of the beam is coupled into six optical fibers. An advantage of fiber interferometers is the spatial filtering such that phase irregularities in the wave-front are converted into amplitude fluctuation that can be corrected for (Mon01). At IOTA, the light is combined by IONIC3 two-beam combiners (Tra02) which provide in analogy to equation (2.9) the interferometric output (Mon01)

$$\begin{aligned} I_{XY}(\tau) &= I_X + I_Y + 2\sqrt{I_X I_Y}\cos(ck\tau - \phi_{YX}) \\ I'_{XY}(\tau) &= I_X + I_Y - 2\sqrt{I_X I_Y}\cos(ck\tau - \phi_{YX}) \end{aligned} \tag{3.1}$$

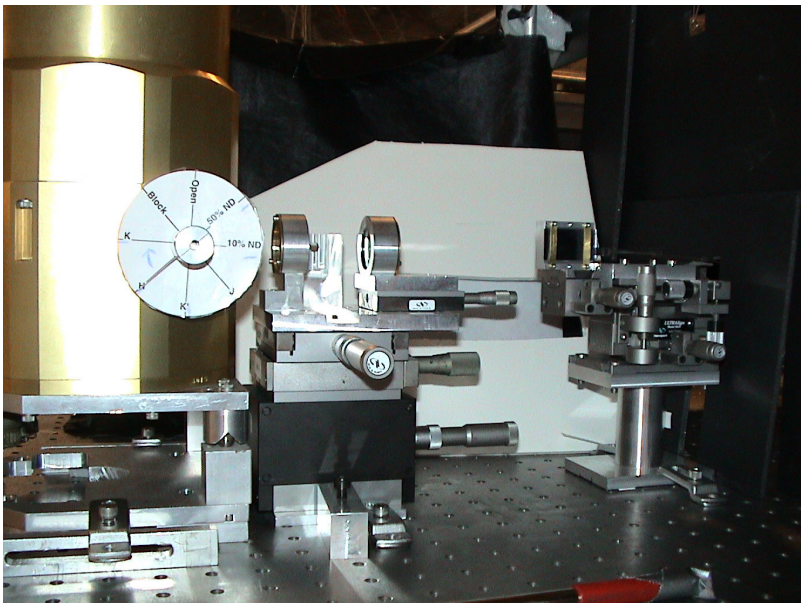

Figure 3.4: The IONIC3 beam combiners (to the right) and the PICNIC camera (to the left).

Table 3.1: Combinations of the three telescopes on the six pixels of PICNIC

Pixel	North Delayed Case	South Delayed Case
0	A C	B C
1	A C	B C
2	B C	A C
3	B C	A C
4	A B	B A
5	A B	B A

where a perfectly balanced coupling is assumed. Using the equations (2.12) and (2.10) it can be shown that this is equivalent to

$$\begin{aligned} I_{XY}(\tau) &= I_X + I_Y + 2VR_F\sqrt{I_X I_Y} \\ I'_{XY}(\tau) &= I_X + I_Y - 2VR_F\sqrt{I_X I_Y} \end{aligned} \tag{3.2}$$

where a perfectly balanced coupling is assumed.

This interferometric output is focused onto the detector of the *PICNIC* camera for all three baselines. The actual allocation of the baselines to the individual PICNIC pixels depends on the configuration North/South delayed case and can be seen in table 3.1.

Technical features of this low-noise HgCdTe camera are four individually controlled 128x128 pixel quadrants and a high (better than 50%) quantum efficiency in the near infrared ($0.8-2.5\mu$m). But most essential is that the camera is able to measure all six signals within a time frame smaller than the coherence time. It is reasonable for the observer to adjust some of the camera parameters in dependence of the atmospheric conditions. The most important camera parameters are N_{reads} (which is the number of times an individual pixel is read for averaging), N_{loops} (which is the number of times a readout is repeated for averaging) and N_{scan} (which is the number of readouts during one scan). Under bad atmospheric conditions it might be reasonable to decrease N_{reads}.

To scan through the fringe package, the optical delay is changed by the piezos on two baselines. Therefore the *optical path delay* (OPD) of a scan is determined by the mechanical stroke L' of a swipe of the piezo scanners. Using the equation $OPD = 2L'/cos(10^\circ)$ by (Mil99) and the value $L' \approx 25\mu$m for SD2 from the headerfiles, then the optical path becomes $L \approx 50\mu$m. SD1 samples with twice that value ($\approx 100\mu$m) and the third baseline with the difference 100μm-50μm$=$ 50μm. So SD1 is scanned at twice the frequency than the other two baselines.

The camera is also equipped with three broadband filters for the J, H and K' band (Pedre). For very bright objects there are neutral density filters with different efficiencies (e. g. ND 3% and ND 25%). In its current configuration, the limiting magnitude for IOTA to measure fringes is about $7\overset{m}{.}0$ in the H-band (Pedre). The six intensities measured on PICNIC (North Delayed Case: [I_{AC}, I'_{AC}, I_{BC}, I'_{BC}, I_{AB}, I'_{AB}]; South Delayed Case: [I_{BC}, I'_{BC}, I_{AC}, I'_{AC}, I_{BA}, I'_{BA}]) are finally saved in datafiles together with headerfiles. The data reduction of those files is going to be examined in chapter 5.

Chapter 4

Observations

4.1 Observation Runs

The data used for this thesis was taken by PETER SCHLOERB and myself in two observation runs, each lasting about one week. In the first run from the 11th to the 16th of November 2002, we concentrated on the close binary star Capella. Another goal of this first observation run was to observe calibrator stars in a high frequency to confirm the overall stability of the instrument. During the week, the atmospheric conditions were improving continuously up to the last night (2002Nov16) when seeing was worsening again.

The beginning of the second run was strongly affected by bad weather conditions such that data could only be taken between the 21st and 24th of March 2003. During this run we observed a large variety of different objects. We placed emphasis on the spectroscopic binary λ Vir for which a period of 206.64d was measured (Hof82). The same reference refutes reports of an 1.93017d period ((Abt61), (Tok97)). This object was already observed by some other members of the IOTA-community, so we tried to provide additional data to allow an orbit fit. Table 4.2 lists the objects and the number of observations which have been done.

The complete observation logs, presented in Appendix A show our observing procedure: Before and directly after each target star we observed calibrator stars to calibrate resolved objects with point sources (in the ideal case). When data acquisition on one star is completed, it is part of the observation sequence to take a set of four additional files with two or all of the beams shuttered out. Later in data reduction, those files can be used to correct for imbalanced beam combination or other asymmetries.

For most observations we used the H band filter which is mounted on one of the filterwheels of the PICNIC camera. This standard filter provides a rectangular window centered at $\lambda_0 = 1.65\mu$m with width $\Delta\lambda = 0.30\mu$m (Mil99). For test purposes we used a 1.65μm narrow band filter as well. A summary of all observed objects is given in table 4.2.

4.2 Capella

The apparent magnitude of $0\overset{m}{.}041$ (Kri90) makes Capella the sixth brightest star on the whole sky. Assuming the parallax of (77.29 ± 0.89) mas measured by Hipparcos (Simbad) one can determine the distance of the spectroscopic binary system to $d = (12.94 \pm 0.15)$ pc.
The system is very well studied. Already the first spectroscopic measurements in 1899 by CAMPBELL (Cam1899) revealed it's nature as a binary star. Since then it was studied intensively over the whole accessible range of the electromagnetic spectrum. The components of the system are classified as G8 III (for Capella Aa) and G1 III (for Capella Ab) giants (Joh02). More detailed spectroscopic measurements revealed the rotational periods of the components itself (Str01). The hotter Ab component rotates with (8.64 ± 0.09)d period, which makes it asynchronous to the binary rotation whereas the cooler Aa component rotates synchronously with a period of 104.022d (Hum94).

The evolutionary state of the two components is very interesting. Both stars have approximately the same mass ($M_{Aa} = (2.69 \pm 0.06)M_\odot$; $M_{Ab} = (2.56 \pm 0.04)M_\odot$ (Hum94)) and comparable diameters ($r_{Aa} = (8.5 \pm 0.1)$ mas; $r_{Ab} = (6.4 \pm 0.3)$ mas) but significantly different evolutionary states. Capella Aa is a Helium burning giant whereas the hotter and more active Ab component is located in the Hertzsprung gap (Joh02). It is counter-intuitive that the hotter G1 III star and not the late-type component is the more active star. Since there is strong evidence (Cha96) for this hypothesis, one must expect more starspots and chromospherical activity on Capella Ab.

The brightness-ratio, I_{Ab}/I_{Aa}, of the two components in the optical seems to be very close, but not exactly equal, to one. In the past there were contradictory conclusions about which of the components is the brighter one (Cha96). Within the last decade high-precision measurements came to the conclusion that Ab is the brighter component in the visual. Ratios for different wavelenghts are:

Table 4.1: Orbital Elements for Capella (Hum94)

Parameter	Capella
a [mas]	56.47 ± 0.05
e	0.0000 ± 0.0002
i [°]	137.18 ± 0.05
Ω (2000.0) [°]	40.8 ± 0.1
T_0 [JD]	2447528.45 ± 0.02
P [days]	104.022 ± 0.002

$$
\begin{aligned}
I_{Ab}/I_{Aa}(140nm)^{1} &\approx 0.06 \\
I_{Ab}/I_{Aa}(275nm)^{1} &\approx 0.25 \\
I_{Ab}/I_{Aa}(450nm)^{2} &\approx 0.77 \quad (\Delta m = (+0\overset{m}{.}28 \pm 0\overset{m}{.}10)) \\
I_{Ab}/I_{Aa}(467nm)^{3} &\approx 0.81 \quad (\Delta m = (+0\overset{m}{.}23)) \\
I_{Ab}/I_{Aa}(547nm)^{3} &\approx 0.92 \quad (\Delta m = (+0\overset{m}{.}09)) \\
I_{Ab}/I_{Aa}(550nm)^{2} &\approx 0.87 \quad (\Delta m = (+0\overset{m}{.}15 \pm 0\overset{m}{.}05)) \\
I_{Ab}/I_{Aa}(643nm)^{4} &\approx 0.93 \quad (\Delta m = (+0\overset{m}{.}08)) \\
I_{Ab}/I_{Aa}(800nm)^{2} &\approx 1.05 \quad (\Delta m = (-0\overset{m}{.}05 \pm 0\overset{m}{.}05)) \\
I_{Ab}/I_{Aa}(830nm)^{5} &\approx 1.11 \\
I_{Ab}/I_{Aa}(1300nm)^{6} &\approx 1.4
\end{aligned}
$$

These measurements will be used later within chapter 6 for comparison with our results.

In the 1920's ANDERSON and MERRILL derived orbital elements for the α Aur system. A very high precision orbit of Capella using optical interferometry was provided by (Hum94) (see table 4.2). This orbit was confirmed by COAST measurements from (Bal96) and (You99) and will be checked for consistency with the measured IOTA data in chapter 6.

Beside the aperture synthesis maps by COAST in the visual and near-infrared there is an image taken with the Faint Object Camera on the Hubble Space Telescope which just separates the components at ultraviolet wavelengths (You02).

[1] from (You02)
[2] from (Hum94)
[3] from BAGNUOLO & SOWELL 1988 (Hum94)
[4] from STRASSMEIER & FEKEL 1990 (Hum94)
[5] from (Bal96)
[6] from (You99)

Table 4.2: Observed Objects. $2\Theta := D$ gives stellar diameter; a is the major semi-axis for binary systems.

Object	Other Designations	Purpose	Expected Appearance of Object for IOTA	No. of observations		No. of different nights		Color & Symbol in plots
				Nov. '02	March '03	Nov. '02	March '03	
α Aur	Capella	Target	Binary ($a = 56.47$ mas)[1]	18	1	6	1	black (×)
|	HD 34029		2 components (4 known)					
δ Aur	HD 40035	Calib.	Disk $D = (2.48 \pm 0.026)$ mas[2]	11	3	4	2	blue (×)
β Aur	HD 40183	Calib.	Binary ($a = 3.3 \pm 0.1$ mas)[3]	10	-	4	-	red (×)
α Cas	HD 3712	Calib.	Disk $D = (6.25 \pm 0.31)$ mas[4]	5	-	5	-	green (×)
α Cyg	HD 197345	Calib.	Disk $D = (2.53 \pm 0.61)$ mas[4]	2	-	2	-	yellow (×)
α Lyn	HD 80493	Calib.	Disk $D = (9.24 \pm 1.02)$ mas[4]	1	-	1	-	cyan (×)
κ Per	HD 19476	Calib.	Disk $D = (2.78 \pm 0.03)$ mas[4]	1	-	1	-	magenta (×)
λ Vir	HD 125337	Target	Binary	-	11	-	4	blue (•)
|			2 Components (3 known)					
HD 126035		Calib.	(?)	-	17	-	4	green (⋆)
HD 158352		Target	YSO	-	6	-	3	cyan (⋆)
δ Crt	HD 98430	Target	Disk (?)	-	5	-	4	red (•)
HR 2152		Calib.	(?)	-	2	-	1	red (⋆)
HR 3621		Calib.	(?)	-	2	-	1	blue (⋆)
HD 157856		Calib.	(?)	-	2	-	2	yellow (⋆)
HD 159170		Calib.	(?)	-	2	-	2	magenta (⋆)
75 Cnc	HD 78418	Target	Binary	-	2	-	1	magenta (•)
β CMi		Calib.	Disk $D = (0.79 \pm 0.03)$ mas[4]	-	1	-	1	green (•)
λ Hya	HD 88284	Target	Binary ($a = 15.18$ mas)[6]	-	1	-	1	cyan (•)
41 Oph	HD 156266	Target	Binary	-	1	-	1	yellow (•)

[1] (Hum94) [2] (Bor02) [3] (Hum95) [4] (Ric02) [5] (Tok97) [6] (Pou03)

Chapter 5

Data Reduction

5.1 Basic Processing

During data acquisition the scans are written in datafiles, each containing $N_{datafile}$ number of scans. Each of those scans consists of N_{scan} readouts each with six pixel values from type double. In November we decided to save 500 scans in each datafile. In the data reduction process all scans in a datafile are reduced separately first. After that the quantities from the separate scans are averaged to decrease the statistical error for the visibility and closure phase measurement. At this point we make the assumption that none of those quantities is changing significantly during the acquisition of one data file, which lasts typically several minutes. As we will see later, this assumption doesn't hold for highly resolved objects. So we choose $N_{datafile} = 200$ for the observation run in March.

The PICNIC camera provides an integrated signal over each scan and resets only at the beginning of a scan. A faster decline in the signal corresponds to a higher flux. By differentiating the raw complementary signals $I_{XY,raw}$ and $I'_{XY,raw}$ from the baseline between telescope X and Y we obtain $I_{XY} = \frac{dI_{XY,raw}}{d\tau}$ and $I'_{XY} = \frac{dI'_{XY,raw}}{d\tau}$. Then the difference of the two signals is calculated to eliminate the atmospheric "common mode" noise. To obtain the *reduced intensity* I_{red} this difference is normalized. Then the arbitrary offset is removed by subtracting the mean such that a fringe package will oscillate in the range $[-1,+1]$ around zero. Naturally this relation doesn't hold for noise. So with a low signal to noise ratio (SNR) the measured signal may

exceed this range (see e. g. figure 5.1 b)). To formalize those steps we may write

$$I_{\mathrm{red}}(\tau) = \frac{I_{XY}(\tau) - I'_{XY}(\tau)}{I_{XY}(\tau) + I'_{XY}(\tau)} - \langle \frac{I_{XY}(\tau) - I'_{XY}(\tau)}{I_{XY}(\tau) + I'_{XY}(\tau)} \rangle \tag{5.1}$$

Of course, the sampling by the camera is discrete so we may denote the time between two readouts as $\delta\tau$.

5.2 Properties of our Data

Figure 5.1 shows some typical scans from our observation run which demonstrate different conditions. The top row shows nice fringes obtained under good seeing whereas the second row demonstrates worse observational conditions. Already during data acquisition we mentioned a disturbing effect and will refer to it as *Resonance Effect*: Beside the fringe peak there is an arbitrary number of additional peaks at lower and higher frequencies. To verify that those additional peaks (like in figure 5.1c) are not due to noise we provide power spectra averaged over 500 scans in figure 5.2. Those peaks are symmetrical around the fringe frequency and are produced by mechanical resonance of the piezo scanners. The amplitude of this effect is varying over the whole range from undetectable to completely dominating, but the effect is typically significantly weaker on the baseline which samples with doubled frequency.

Also in time space one can seen an interesting effect: Sometimes there seem to be fluctuations of the frequency within the fringe package. Quite often this effect observed in time space may be correlated with the earlier mentioned resonance problem. Another reasonable explanation is that the atmospheric piston effect changes the light path above the individual telescopes which may result in frequency changes within the scan as well. For highly resolved objects like Capella the fringe might be complex due to the nature of the source structure (see chapter 2.3). An extreme case can be seen in figure 5.3.

The resonance effect described above requires special treatment and data reduction procedures that are beyond the standard repertoire. For example, to estimate the visibility the routine procedure would be to measure the power of the fringe in the power spectrum of the scan. However it turned out that this approach did not lead to satisfying results. Therefore other routines needed to be developed and were implemented. In the following we present the different procedures and the results demonstrated on the representative data shown in figure 5.1.

a) Good Conditions (Example: α Cas):

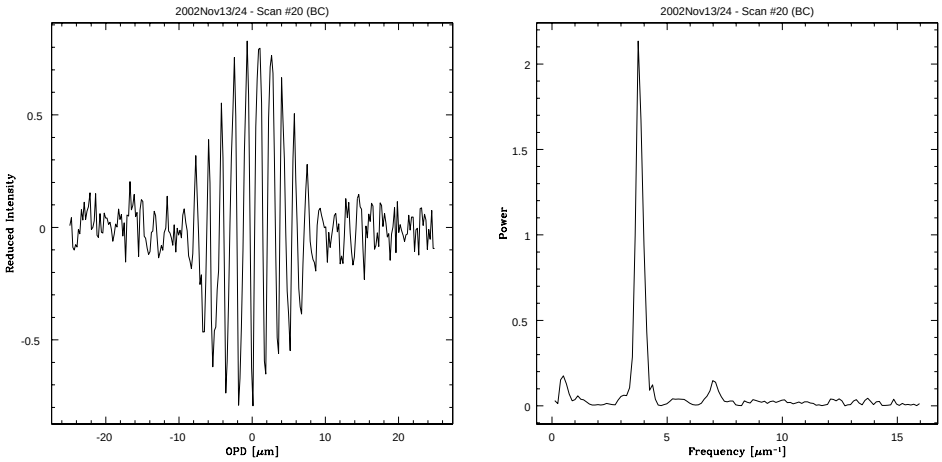

b) Bad Signal-Noise (Example: δ Aur):

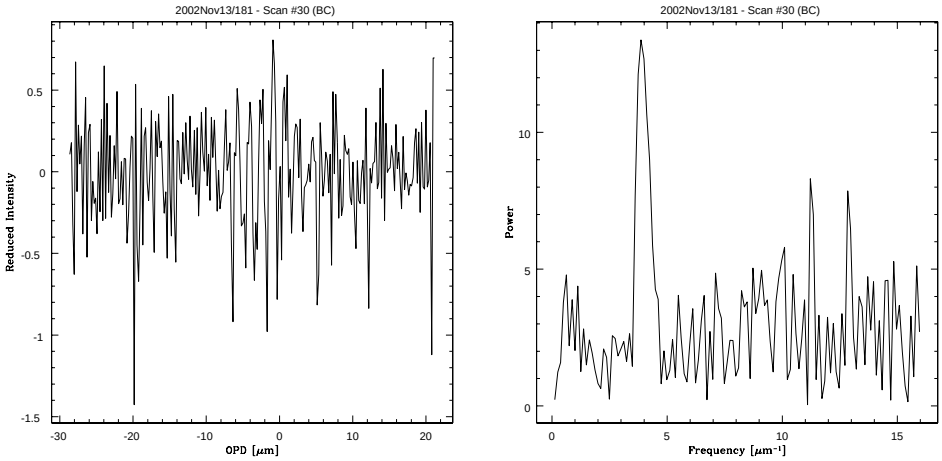

c) The "Resonance Effect" (Example: α Lyn):

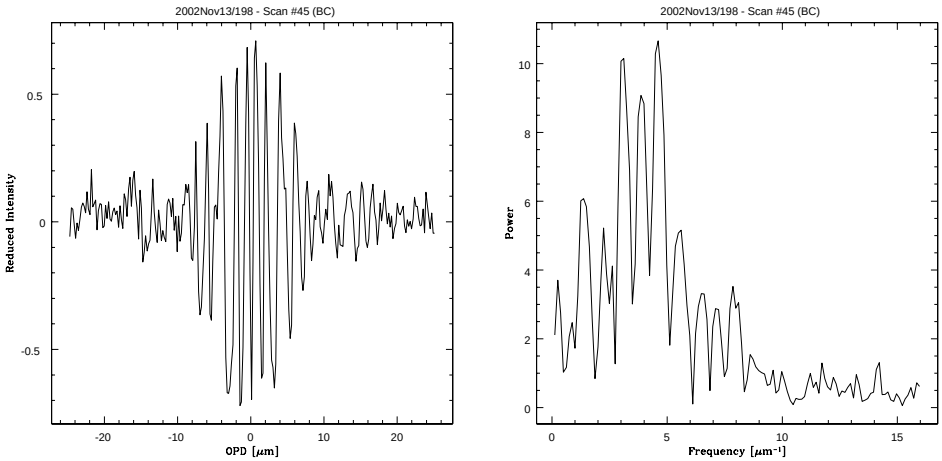

Figure 5.1: Representative Scans from November 13, 2002. The left column shows the reduced intensities, the right one the power spectra.

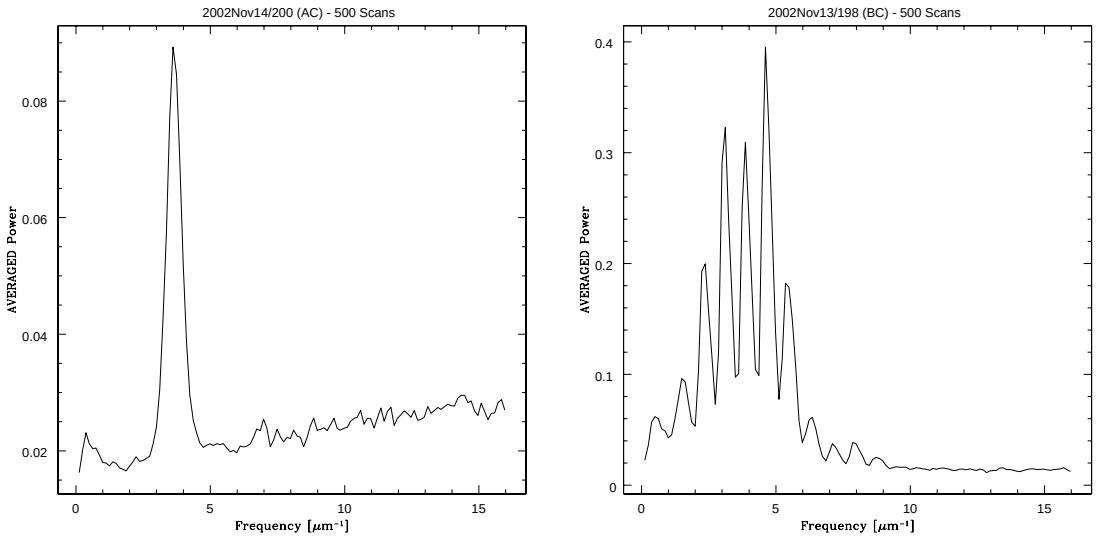

a) **b)**

Figure 5.2: Averaged power spectra with weak and strong resonance. In the right figure the resonance peaks are even stronger than the fringe peak.

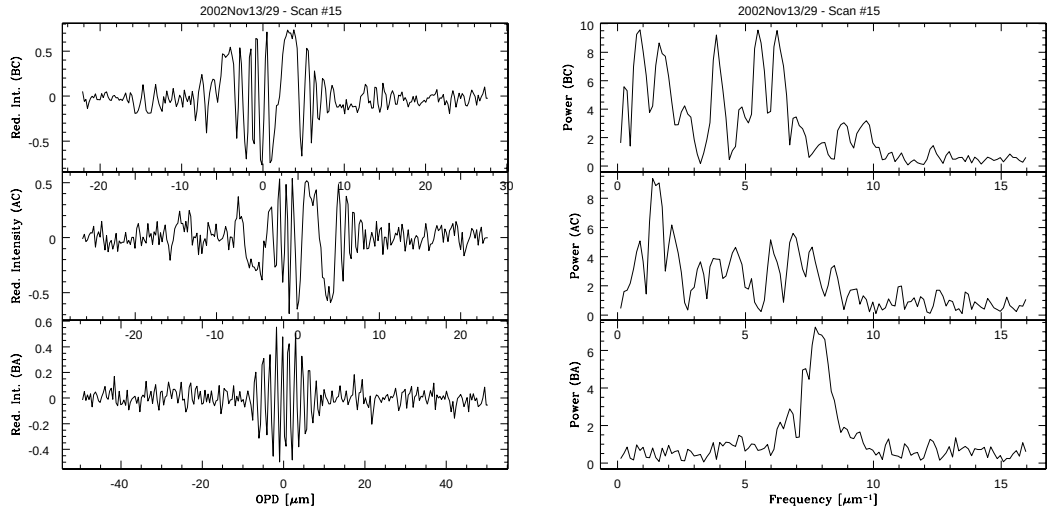

Figure 5.3: Case with extreme distortion in two of the three fringes (Source: α Cas).

5.3 From the Raw Data to the Visibility

In the following sections we will present different methods to estimate the amplitude of a fringe μ (also called the *Fringe Visibility* or the *Coherence Factor*). To correlate those measured quantities to the visibility as defined in equation (2.15) we have to correct two important effects:

- The telescopes or the beam combiner might be *unbalanced*, i. e. the light intensity reaching the camera pixels from two telescopes may not be equal.
- The interferometric efficiency of the systems must be measured on a reference source. This instrumental response is given by the *transfer function* T and may change during the observation.

Therefore the fringe amplitude must be corrected for both effects to obtain the visibility V:

$$V = \frac{U\mu}{T} \tag{5.2}$$

where U is a correction factor for the imbalance between the two telescopes. The calculation of U will be discussed in section 5.4.

The value T is defined as the fringe visibility when observing a point source with a balanced system. Therefore this factor can be easily obtained for one particular time by reducing the observed calibrators in the same way as the target stars. For an unresolved source $T \equiv \mu_{calib,unres.}$ whereas for a resolved calibrator with an a priori known uniform disk diameter Θ_{UD} the correction becomes $T = \mu_{calib,res.}/V_{UD}(\Theta_{UD})$ (using equation (2.22)). Ideally, the calibrator source should be from the same spectral type as the target.

In general, the most promising concept to determine the transfer function for an observation at a particular time t is the interpolation between neighbouring groups of calibrators. First all contiguous measurements of one calibrator are grouped and the average $\langle T \rangle$ is calculated for each group. To calibrate a fringe visibility $\mu(t)$ one may just interpolate linearly between the neighbouring calibrator groups. Let's call the averaged transfer functions of the two groups $\langle T_l(t_l) \rangle$ and $\langle T_r(t_r) \rangle$ then

$$V(t) = U\mu(t) \left(T_l + \frac{T_l - T_r}{t_l - t_r}(t - t_l) \right)^{-1} \tag{5.3}$$

Sometimes directly neighbouring calibrator groups might be not available. Then one can make the assumption that T is quite stable over the night. Thus the fringe visibility of all calibrators for that night can be just averaged to obtain $\langle T \rangle$. Fortunately it can be checked empirically how good the assumption is just by

looking at the scattering of the estimated fringe visibilities of unresolved stars during that night. This procedure might be also useful to measure resolved calibrators against other less resolved calibrators to obtain stellar diameter estimations. This happened in our observation run in November 2002 for the calibrator stars α Lyn and α Cas. To use them for the calibration of target objects we used the fitted stellar radius Θ and corrected the measured fringe visibility by dividing with $V_{UD}(\Theta)$.

5.3.1 Extracting the Fringe Visibility using the Power Spectrum

According to PARSEVAL's theorem the power of a signal is the same whether computed in time or frequency space. Since we may choose an arbitrary normalization, we can define the power spectrum as the absolute square of the fourier transform $\mathcal{P}(\nu) := |\mathcal{F}(\nu)|^2$. In practice, the power spectrum is calculated with a fast Fourier transform (FFT) and the relation $\mathcal{P}(\nu) := \Re(\mathcal{F}(\nu))^2 + \Im(\mathcal{F}(\nu))^2$. To avoid aliasing, the data is multiplied by a window function (e. g. the Welch window (Pre92)) before the computation.

A very nice property of power spectra is that in averaging, real signals add constructively in the power spectrum while it decreases noise. Thus this method is useful, especially for the measurement of the fringe power in cases of low SNR.

The width of the fringe peak in the power spectrum is given by the bandwidth but it might also be broadened by atmospheric piston. In addition, there is a noise background which has a positive, but quite constant, slope in most of the cases. To fit the fringe peak the background is first estimated by measuring the lowest power $P_l(\nu_l)$ in a window on the lower-frequency end of the covered frequency range. The same is done for P_r, measured at ν_r in a window on the high-frequency end of the power spectrum.

This averaged background level with constant slope is subtracted such that mainly the signal remains:

$$\mathcal{P}_{\text{bgsub}}(\nu) = \mathcal{P}(\nu) - \left(\mathcal{P}_l + \frac{\mathcal{P}_l - \mathcal{P}_r}{\nu_l - \nu_r}(\nu - \nu_l) \right) \tag{5.4}$$

Finally a Gaussian is fitted to the data. The fit was realized with a least square fit based on the LEVENBERG-MARQUARDT-algorithm presented in (Pre92). The amplitude, width and central frequency of the Gaussian are free parameters. With reasonable initial guesses this algorithm works well on data with single peaks as figure 5.4 a) shows. But the appearance of additional strong resonance peaks can confuse this fitting algorithm and lead to incorrect results (as in figure 5.4 b)).

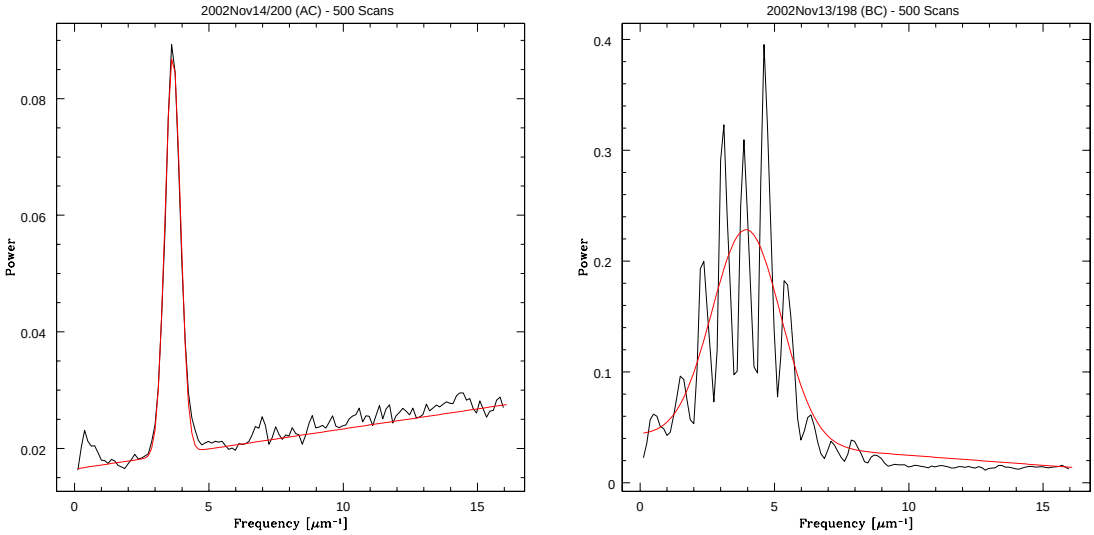

a) **b)**

Figure 5.4: Averaged power spectra with weak and strong resonance (black) and the fitted Gaussian with background (red).

The fringe visibility estimated with this method for all nights of our observation run in November 2002 is shown in figure 5.5. It is worth noticing that the abscissa shows the file number and not time as in some other plots. This way all nights (separated by vertical lines) can be shown in just one plot. The thin horizontal lines show the transfer function averaged over all calibrators observed during one night. Since the calibrators scatter dramatically about those averages, this method seems not to be adequate to estimate the fringe visibilities for our data due to the disturbing influence of the resonance peaks.

Also the attempt just to integrate the signal above the noise level within a reasonable-sized window around the fringe peak frequency (in the hope the total power would be conserved even with resonances) did not yield satisfying results. Therefore below we consider new methods which do not require use of the power spectrum.

5.3.2 Extracting the Fringe Visibility by Fringe Envelope Fitting

The *Fringe Envelope Fitting algorithm* avoids all trouble which may rise from the disturbing resonance or any piston effects by ignoring the internal structure of the fringe packet. To our knowledge, this new method

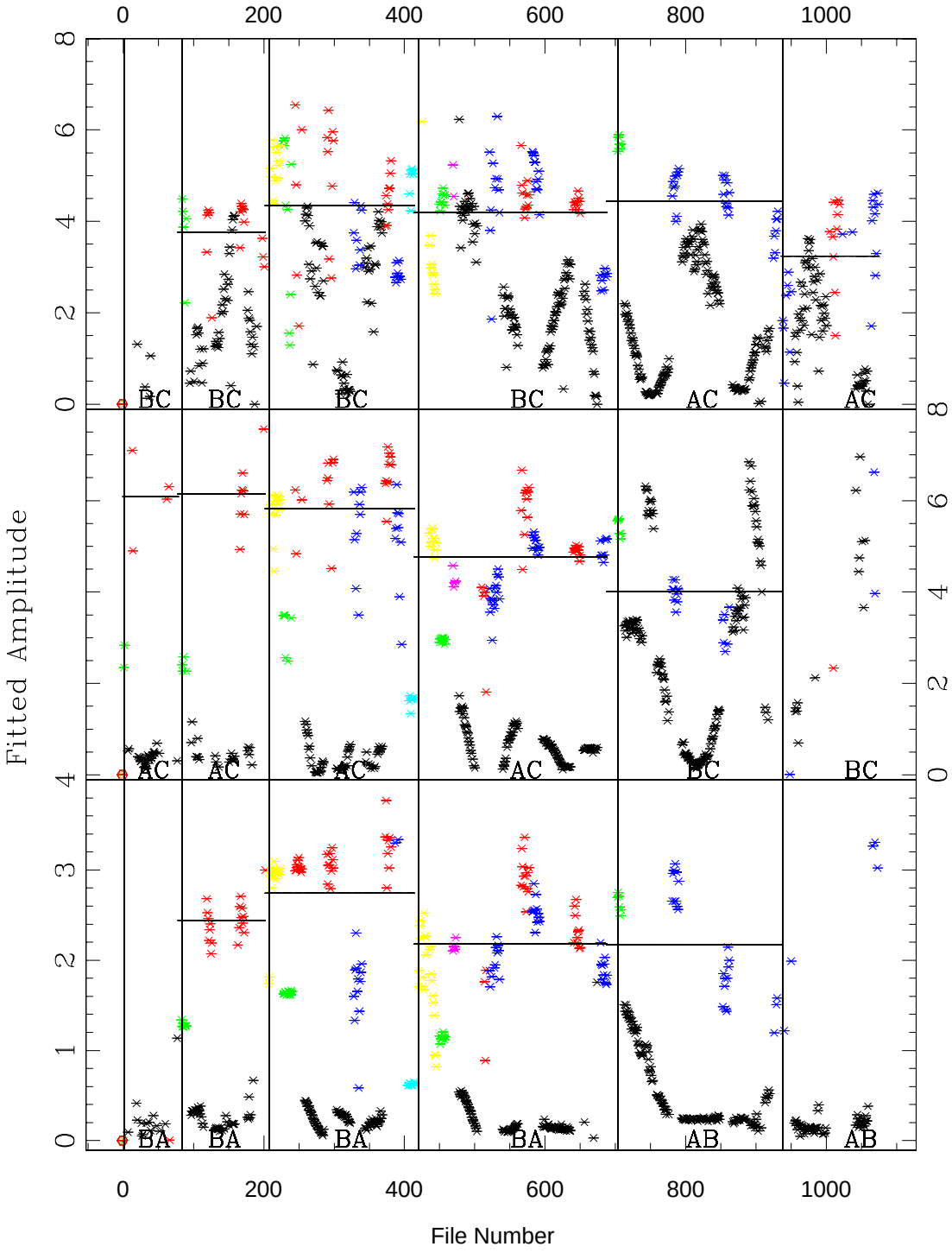

Figure 5.5: The data from our observation run November 2002 reduced using the Power Spectrum Method. The vertical lines separate the different nights whereas the horizontal lines give the average of the unresolved calibrator stars. Points with negative fi tted amplitude were rejected during the reduction process. Color Code: see table 4.2

has not been reported in previous work on this subject. Instead of fitting the response function from equation (2.12), this algorithm just picks the local maxima and minima and fits this envelope to the sinc-envelope function.

To determine the fringe envelope, the algorithm runs through all points of a scan and identifies those points which are local extremes. To ensure that it is not only a small-scale fluctuation, we used for a local maximum at the point $I_{\mathrm{red}}(\tau)$ the criteria $I_{\mathrm{red}}(\tau) \geq 0$ and $I_{\mathrm{red}}(\tau - 2\delta\tau) \leq I_{\mathrm{red}}(\tau - \delta\tau) < I_{\mathrm{red}}(\tau) > I_{\mathrm{red}}(\tau + \delta\tau) \geq I_{\mathrm{red}}(\tau + 2\delta\tau)$. By replacing $I_{\mathrm{red}}(\tau)$ with $-I_{\mathrm{red}}(\tau)$, we get the criterion for the negative envelope points. Applying these criteria to the data provides a set of points for the positive envelope $\mathcal{E}_{\mathrm{pos}} := \{(\tau_i, I_{\mathrm{red}}(\tau_i))\}$ as well as a set of points for the negative envelope $\mathcal{E}_{\mathrm{neg}} := \{(\tau_j, I_{\mathrm{red}}(\tau_j))\}$. Instead of fitting those two sets of envelope points separately, we may calculate the set union $\mathcal{E} := \mathcal{E}_{\mathrm{pos}} \cup \mathcal{E}_{\mathrm{neg}}$ and fit this to the sinc-envelope function to obtain a more physically meaningful result since the two envelopes are not independent.

Our algorithm fits the function

$$I_{\mathrm{red}}(\tau) = \mu \cdot \mathrm{sinc}\left(\frac{W}{2\pi}(\tau - C)\right) \tag{5.5}$$

To get reasonable results, the fit algorithm needs an initial estimate for the three fit parameters μ, W and C. For the width W of the envelope one may just use a typical value for this specific baseline. The fringe center C can be localized by the *IOTA-Ames Fringe Tracker* (Wil02) with sufficient precision. This program determines whether or not there is a fringe packet within a scan using the power spectrum and some symmetry criteria. Additionally it provides an estimate of the position of the fringe and the Gaussian noise. In the final fit all three parameters may be varied. However the overall result seems to improve when a second fit is performed with W as fixed parameter, since high noise tends to bias the algorithm to fit wider envelopes. The χ^2 provided by the fit algorithm is used as the criterion to decide whether the fit with free or fixed width is better.

Figure 5.6 shows the same examples as figure 5.1 but with the extracted envelopes and the fitted sinc functions. As demonstrated in case c) this algorithm is not affected by the resonance effect. The noise-case b) shows how important it is for this algorithm to choose reasonable rejection criteria to eliminate noisy scans. Good criteria are χ^2 and the aberration of the fitted values from the estimations. So case b) would be rejected because of the high χ^2 and of the unrealistic large fitted W parameter.

To verify the proper behaviour of this algorithm and justify the step of averaging, we did a Kernel Density Estimation (KDE) of one group of continuous observations of α Cas. As Figure 5.7 a) shows, is μ for the

a) Good Conditions (Example: α Cas):

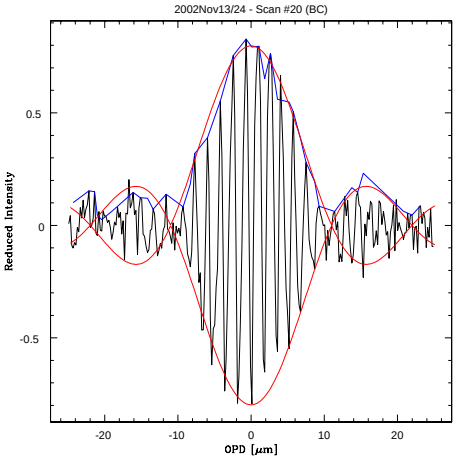

b) Bad Signal-Noise (Example: δ Aur):

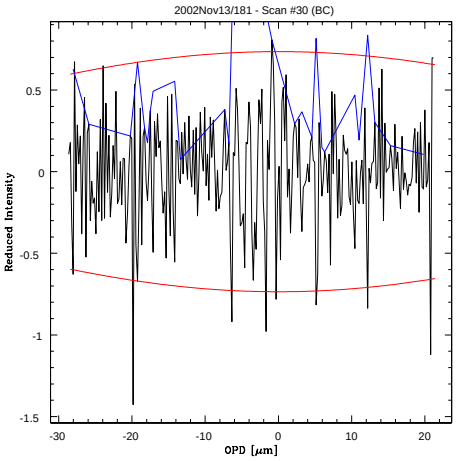

c) The "Resonance Effect" (Example: α Lyn):

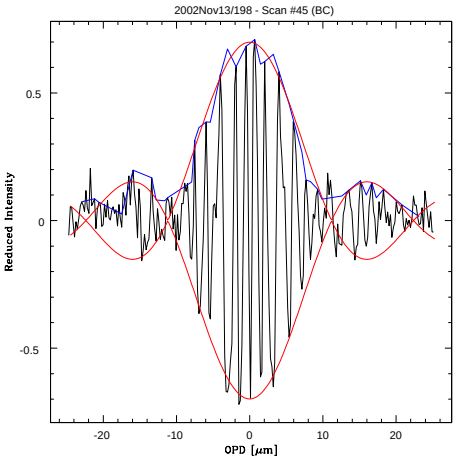

Figure 5.6: The same example as in figure 5.1 with the extracted envelope (blue) and the fitted envelope function (red). The set of negative envelope points $\mathcal{E}_{neg}$ had be inverted to obtain $\mathcal{E}$!

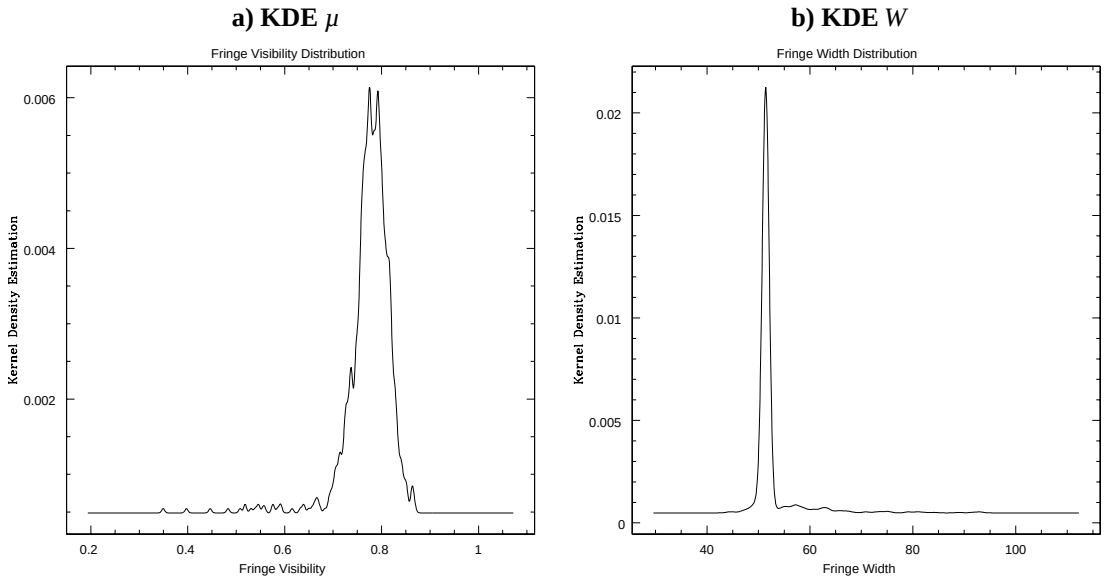

Figure 5.7: Distribution of the fitted μ and W for 6500 scans from 2002Nov13/21..37 of the resolved star α Cas on the *BC* baseline. A Gaussian Kernel with width 4.0 was used for the μ-KDE. For the W-KDE the Kernel width was 0.1.

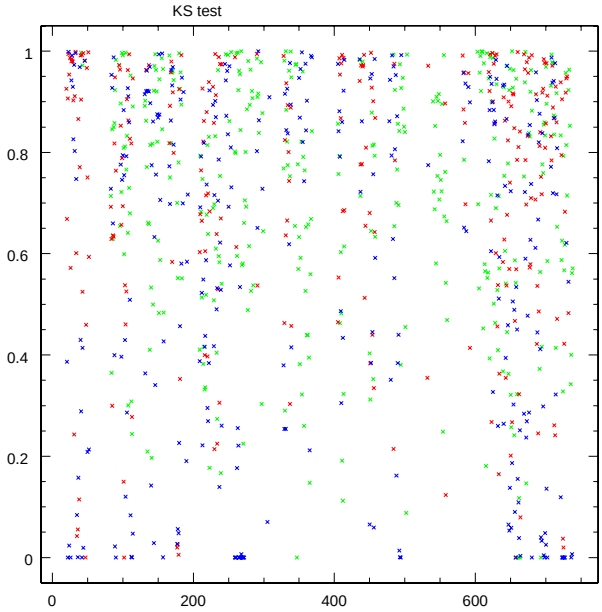

Figure 5.8: Results of a KS-test with the Null hypothesis that the distribution of the fitted amplitudes is Gaussian (1=it is Gaussian, 0=it is not Gaussian). 870 data sets are sampled. The colors are representing different channels.

processed 6500 scans quite Gaussian distributed. Also the distribution of W seems to be well behaved as figure 5.7 b) shows. A Kolmogorov-Smirnov (KS) test (Pre92) gave the result that for 42 of 870 data sets the Null hypothesis, that the fringe visibility distribution is Gaussian, must be rejected on a 3σ-level (see figure 5.8). So it seems to be justified to take the mean as an estimation of μ for a whole datafile. The error is then given by the standard deviation for N independent scans $\sigma/\sqrt{(N-1)}$.

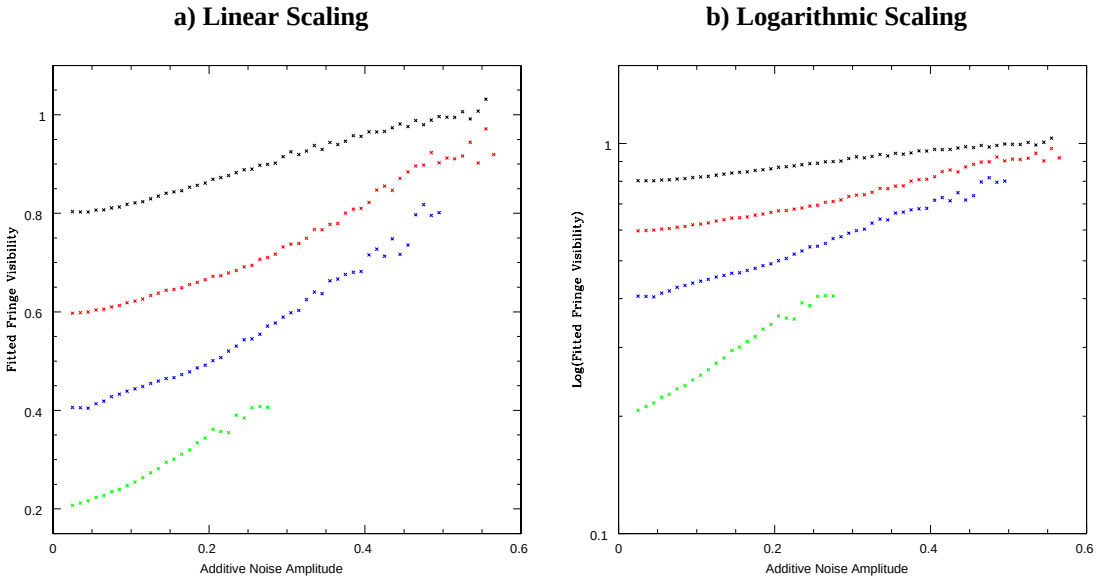

Figure 5.9: Response of the fringe envelope fitting algorithm to additive Gaussian noise. Simulated fringes with amplitudes of 0.2 (green), 0.4 (blue), 0.6 (red) and 0.8 (black) were generated and then fitted in the same way as real data. The ordinate gives the amplitude of the added noise.

One might expect that the algorithm would tend to overestimate the Fringe Visibility as soon as the noise level becomes high. To examine the behaviour of the algorithm under controlled conditions we simulated fringes with additive Gaussian noise of amplitude ε. The typical result for such a simulation can be seen in figure 5.9: The fitted Fringe Amplitude stays quite stable for low noise and shows then an inclining bias till the envelope cannot be fitted anymore. Since the bias seems to follow a comprehensible law we tried to apply corrections. Two different attempts were taken: Since the logarithmic plot in figure 5.9 b) shows straight lines, we tried first a simple exponential law for the correction

$$\mu_{unbias} = \mu \cdot e^{-\varepsilon\rho} \tag{5.6}$$

where ε is provided by the *weight*-parameter from the *IOTA-Ames Fringe Tracker* (Wil02) and ρ must be

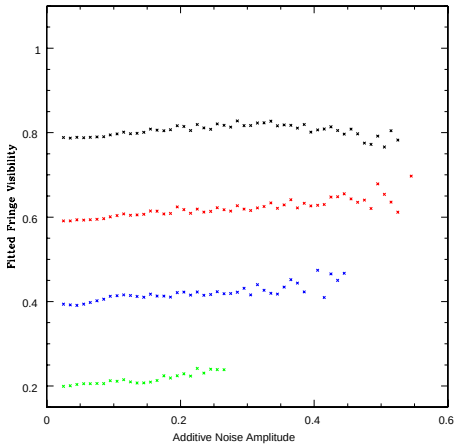

Figure 5.10: Same data as in 5.9 with the correction from equation (5.6) and the parameter $\eta = 0.5$ applied. The noise ε was measured independently from the noise value used for the generation of the Gaussian noise.

determined from the average slope of the lines in figure 5.9 b). The result of this correction can be seen in figure 5.10. The bias is removed up to a few percent. Since the slopes are not the same for all fringe visibilities some residuals remain. Therefore a correction was attempted using a 2-D correction matrix which would supply the correction factor for each unique noise versus fitted fringe amplitude combination. This matrix was calculated with the generation of simulated fringes for thousands of different parameters. Unfortunately the corrections from this matrix tend not to be very smooth so we observed undesirable steps within the corrected fringe visibilities and rejected this method.

Figure 5.11 shows the fringe envelope fitting algorithm applied on the data from November. Bias-corrections using equation (5.6) were done. The scattering of the calibrator stars around the average value is quite low and it is easy to perceive that the stars α Cas (green) and α Lyn are resolved compared to other calibrators.

5.3.3 Extracting the Fringe Visibility using the Continuous Wavelet Transform

The wavelet transformation is a common tool in some special branches of medicine, meteorology and computer science where it is used e. g. for arrythmia diagnostics, the analysis of El Niño phenomena and for video signal compression. We found the first mention of wavelets for the purposes of astronomical interferometry in (Que02) where DAMIEN SÉGRANSAN mentions this method for the use of the reduction of noisy interferograms. Since no further details are given and this method appears only as a footnote in the journals,

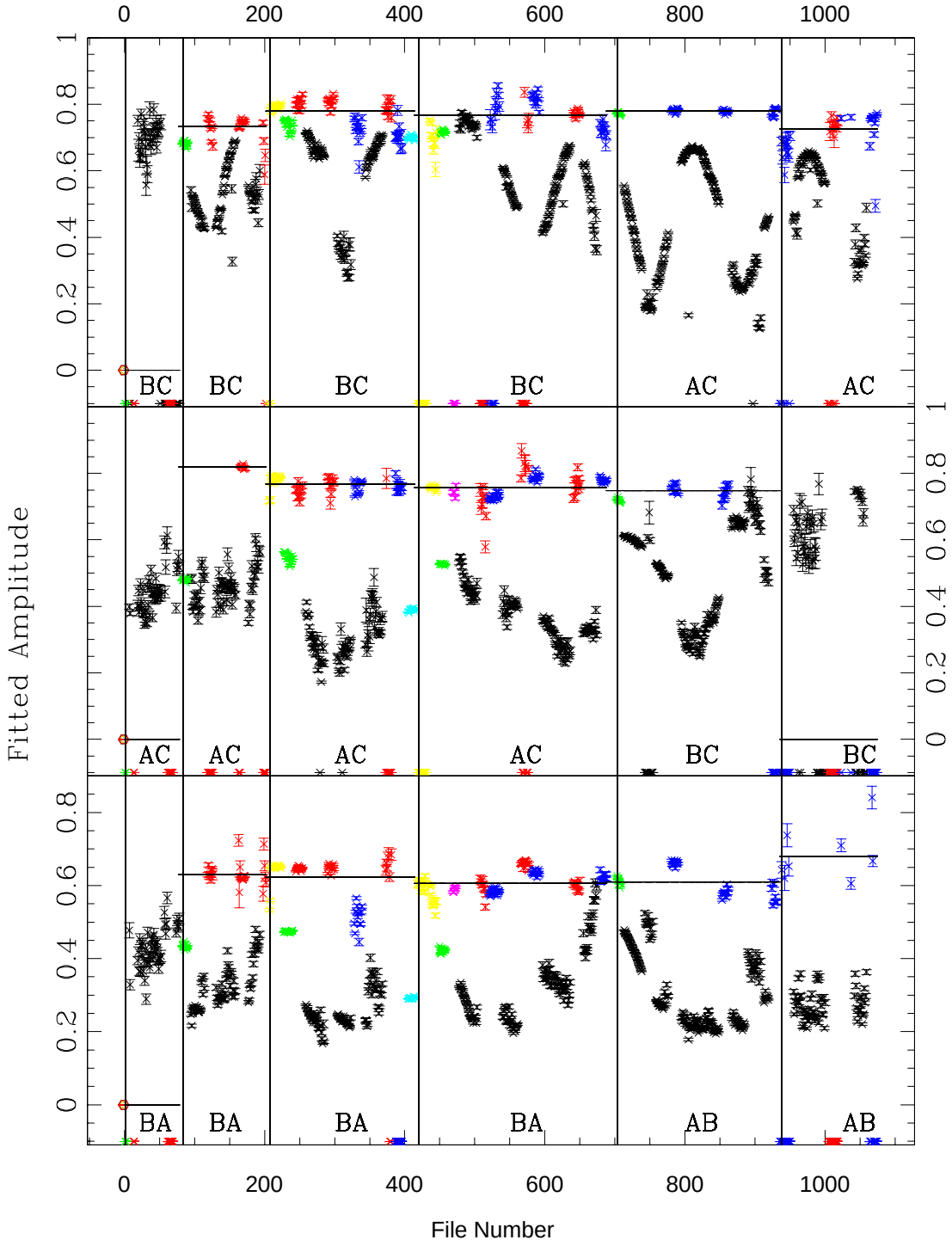

Figure 5.11: The data from our observation run November 2002 reduced using the Envelope Fitting Algorithm. Same settings as in figure5.5. Color Code: see table 4.2

we developed our own reduction procedure based on the CWT. In the mathematical formulation of wavelet theory we follow (Tor98). Unfortunately, for the CWT, there is no analogue to PARSEVAL's theorem for Fourier analysis.

In wavelet analysis, the time signal is decomposed into the two-dimensional time-frequency space which allows localization of the signal. The one-dimensional Fourier transform (FT) measures a signal against periodic, but non-localized sine and cosine waves, therefore it is not possible to localize the power within the signal. But instead of just shifting a window over the data and then calculating the FT (what is done in the windowed Fourier transform WFT), the wavelet transform replaces the sinusoidal waves of the FT with a function called the *mother wavelet* $\psi(\eta)$. The choice of this mother wavelet is quite arbitrary even if this function has to comply with some normalization conditions (see (Tor98)). Since we are going to measure the response of this mother wavelet to our interferograms, it is definitely advantageous to choose a mother wavelet which shows similarities to the fringe function (equation 2.12). Therefore a proper choice might be the Morlet wavelet, which is a sine wave modulated with a Gaussian

$$\psi(\eta) = \pi^{-1/4} e^{ik_0\eta - \eta^2/2} \tag{5.7}$$

where k_0 is the wavenumber to be adjusted such that the number of fluctuations within ψ roughly fits the number of fluctuations within a typical fringe package (so we choose $k_0 = 6$).

Now the CWT is defined as a convolution of the signal $I_{\mathrm{red}}(\tau)$ with the complex conjugate of a *wavelet* (which is just a translated and dilated/contracted version of the mother wavelet)

$$\mathbb{W}(\tau, s) = \frac{1}{\sqrt{s}} \int_{-\infty}^{\infty} I_{\mathrm{red}}(t) \psi^* \left(\frac{\tau - t}{s} \right) dt \tag{5.8}$$

By varying s and τ one obtains a two-dimensional image with real and imaginary part. It is worth mentioning that the *scale s* should not be identified with the frequency since the time frequency resolution depends on the scale s! Finally, we obtain the wavelet power spectrum with $\mathcal{P}_W(\tau, s) := |\mathbb{W}(\tau, s)|^2$.

Since the direct computation of the integral (or summation) in equation 5.8 is very time consuming we implemented the algorithm by (TorCo) which makes use of the FFT to accelerate the computation. Since we

a) Good Conditions (Example: α Cas):

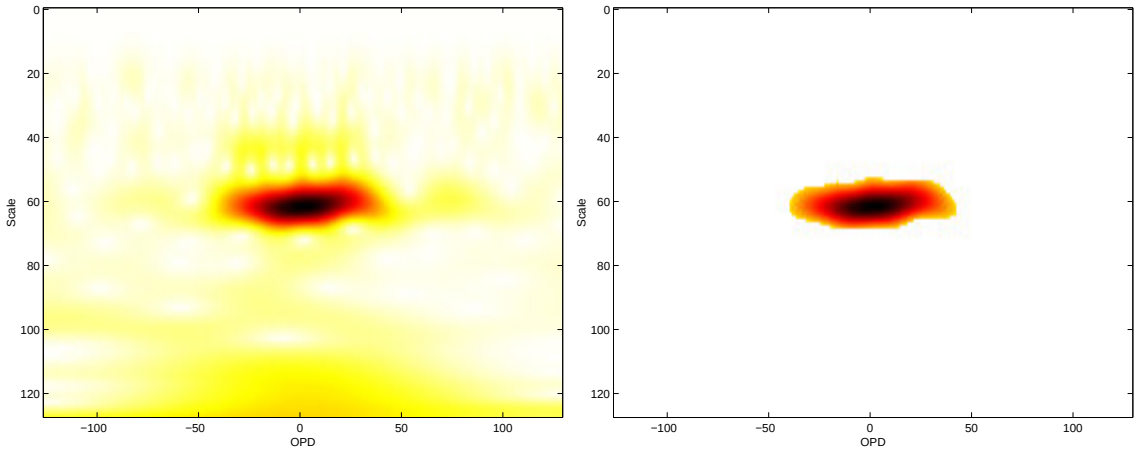

b) Bad Signal-Noise (Example: δ Aur):

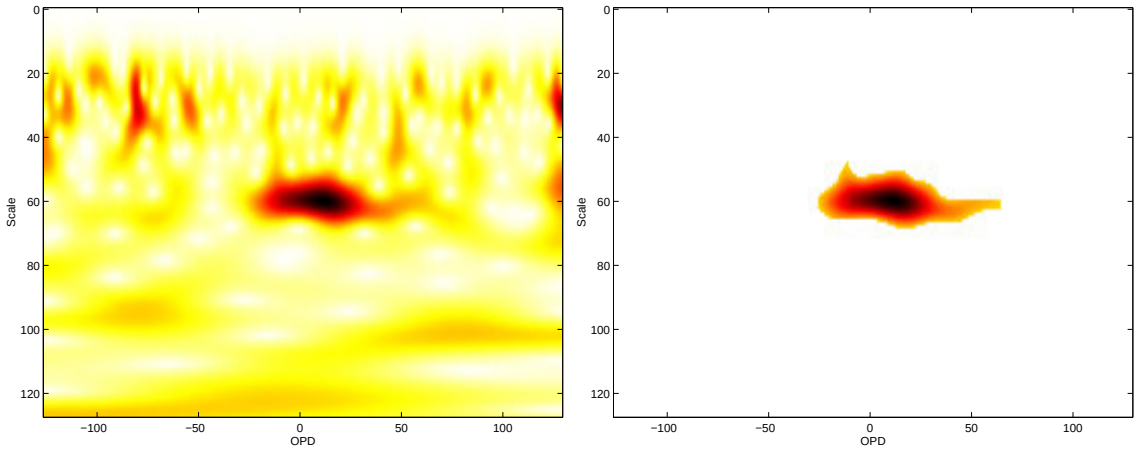

c) The "Resonance Effect" (Example: α Lyn):

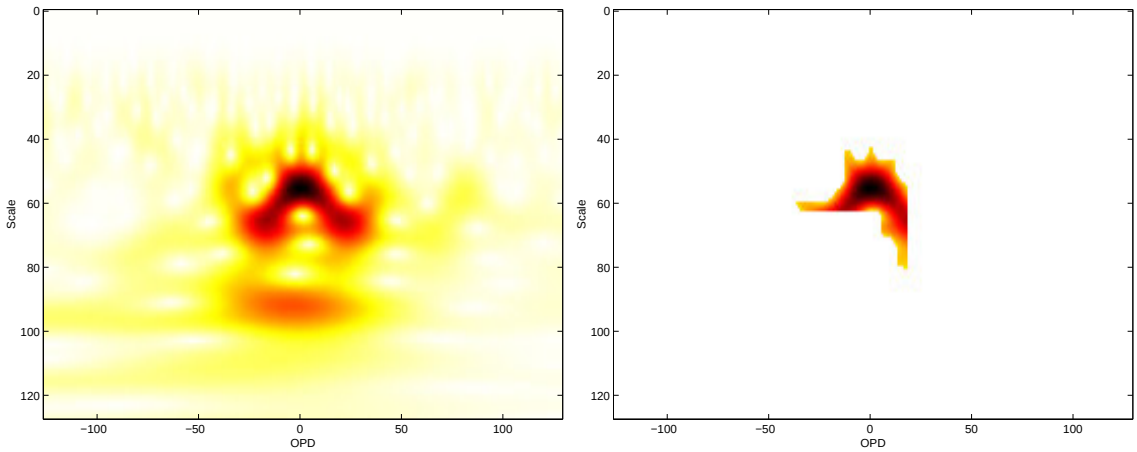

Figure 5.12: *Left:* The CWT of the same examples as in figure 5.1. Dark red stands for the highest intensity, white and yellow are low intensities. *Right:* After applying our filter

a) Good Conditions (Example: α Cas):

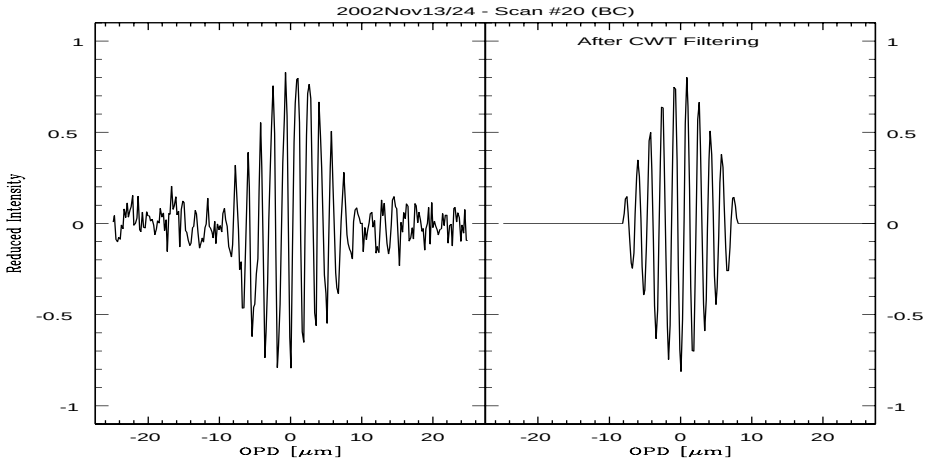

b) Bad Signal-Noise (Example: δ Aur):

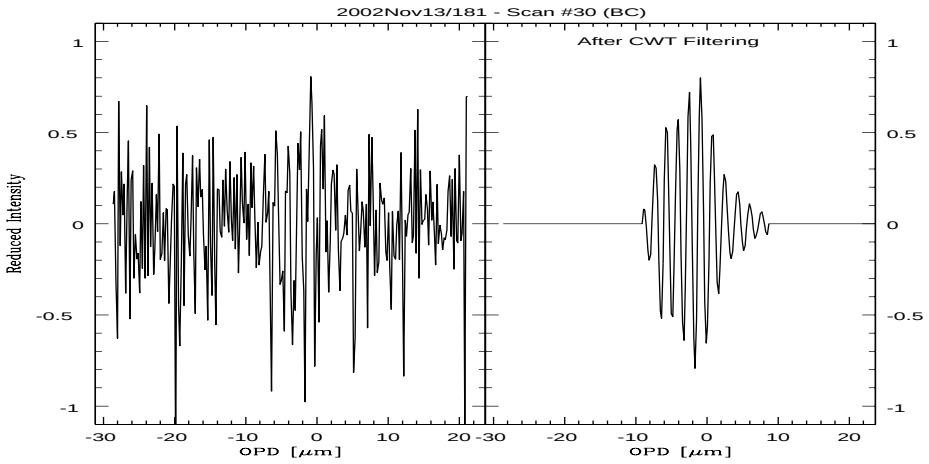

c) The "Resonance Effect" (Example: α Lyn):

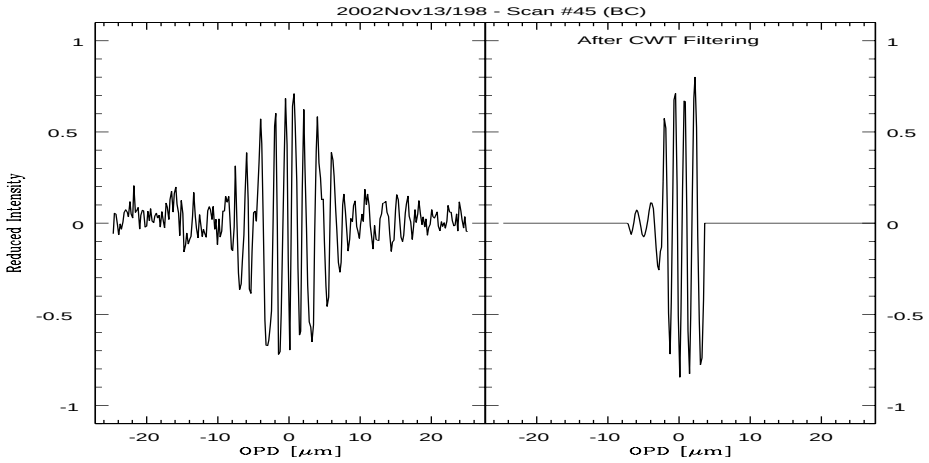

Figure 5.13: The examples from figure 5.1 after applying our CWT filter algorithm.

can neglect normalization factors, the inverse transformation is simply given by

$$I_{\mathrm{red}}(\tau) = \int_{-\infty}^{\infty} \Re(\mathbb{W}(\tau, s))ds \tag{5.9}$$

The CWT of the sample data can be seen in figure 5.12. Resonance as well as noise causes the highly localized fringe power to spread over a larger area. To isolate the fringe itself we apply a filter which removes all signal below some significance level (e. g. 60%). In addition we implemented a routine which filters out all those areas that are separated from the partition with the highest intensity in it. The spread of this remaining partition is used as a rejection criteria. When the spread along the scale or time axis or the whole area is too large then the scan is rejected. The same applies when the partition lies too close to the borders. For good scans, the power of the fringe is estimated as the integral over the partition.
After the filtering it can be also desirable to perform the inverse transformation as given by equation 5.9. This way one may evaluate how well the algorithm picks the right area around the fringe. The inversed filtered CWT is shown in figure 5.13, and it seems that our algorithm works excellently in all cases of good as well as bad SNR. Also in cases with resonance the algorithm picks the fringe much better than the FT algorithm (compare to figure 5.2). The partition desegmentation routine tends to cut the offshoots of resonance fringes away. Therefore the routine may tend to underestimate the fringe power in cases with resonances.

In figure 5.14 and 5.15 we present the data from both of our observation runs reduced with the CWT algorithm. Two groups on November 15, 2002 extend the calibrator levels (BC baseline). Those are the scans which were obtained with the 1.65μm narrowband filter (see Log in Appendix A) and had to be rejected due to the lack of calibrators with the same configuration.

5.4 Correcting Imbalances between the Telescopes

Each observation on one target is completed by the acquisition of the four *matrixfiles*. The purpose of three of those files is to measure the individual intensities without any interference. This is achieved just by shuttering out the light of two telescopes alternately. In the following, I will refer to those three files with M1 (only the shutter for the fixed delay is open), M2 (only the shutter for SD1 is open) and M3 (only the shutter for SD2 is open). The fourth matrixfile (M4) measures (comparable to a darkframe) the intensity with all shutters closed. Normally only 100 scans are saved in the matrixfile. The PICNIC camera on IOTA measures six pixels all in all or three pairs with complementary interferometric outputs, each pair

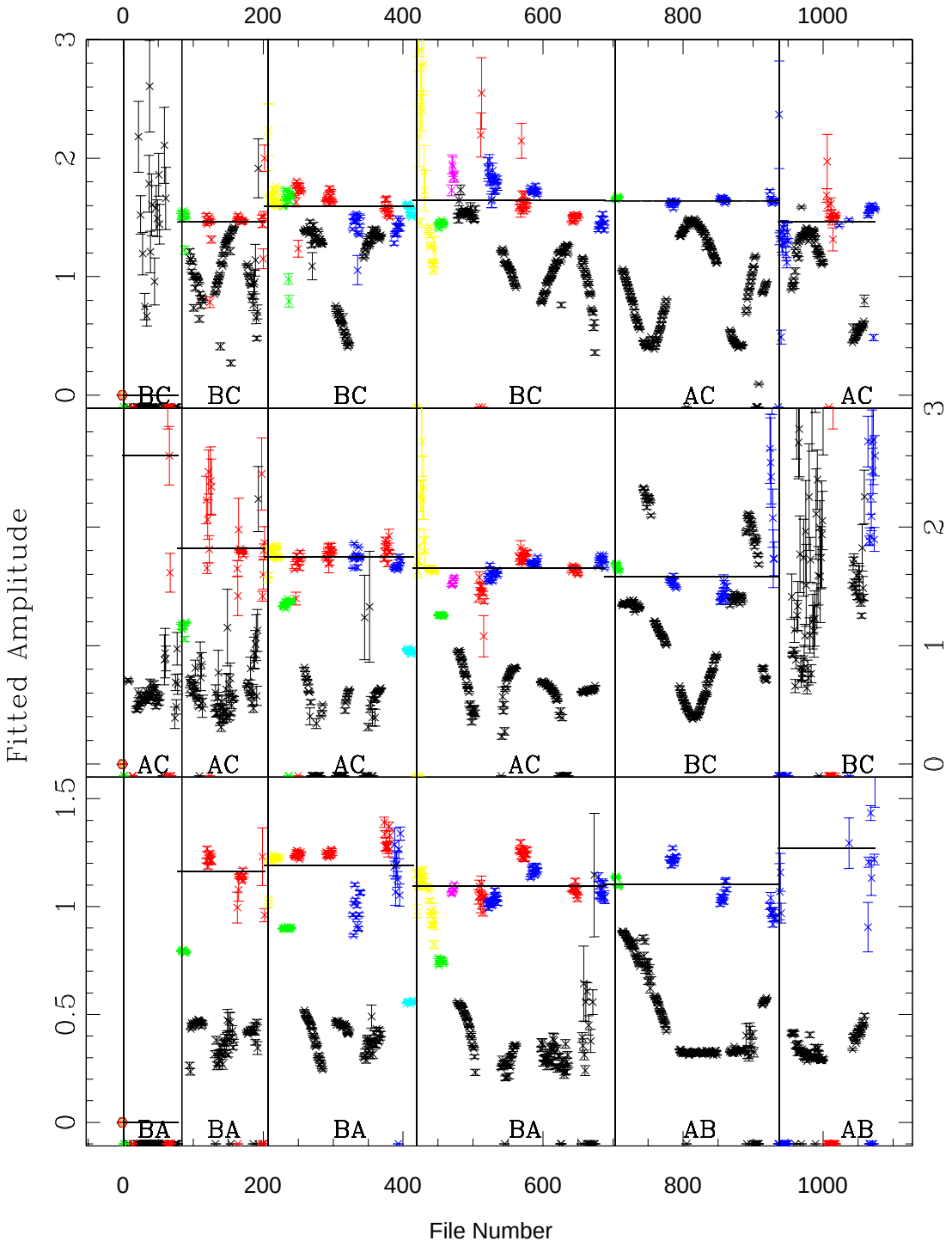

Figure 5.14: The data from our observation run in November 2002 reduced using the CWT algorithm. Same settings as in fi gure5.5. Color Code: see table 4.2

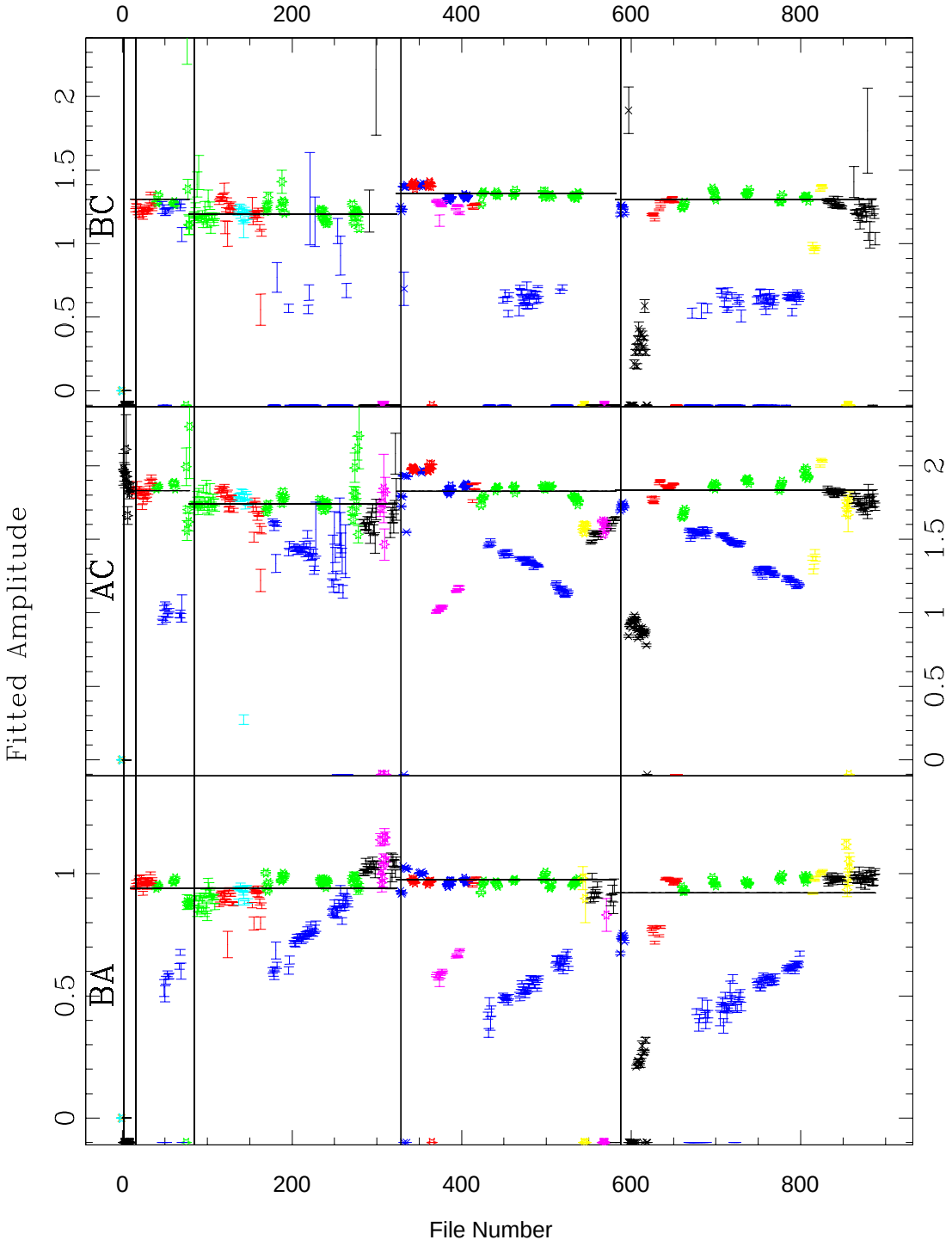

Figure 5.15: The data from our observation run in March 2002 reduced using the CWT algorithm. Same settings as in figure5.5. Color Code: see table 4.2

corresponding to one baseline combination. As described in chapter 3 the specific allocation of the individual pixels to the telescopes depends on the configuration (North/South Delayed Case). To keep the following equations general we will just refer to the notation already used in equation (5.10) such that X and Y denote two different telescopes which are producing the interferometric output $I_{XY}(\tau)$ and $I'_{XY}(\tau)$. But in contrast to the earlier definition we distinguish now between the individual intensities I_X^a, I_X^b, I_Y^a, I_Y^b as measured by the pixel pair a, b on the PICNIC camera. Then it yields that

$$\begin{aligned} I_{XY}(\tau) &= I_X^a + I_Y^a + 2VTR_F\sqrt{I_X^a I_Y^a} \\ I'_{XY}(\tau) &= I_X^b + I_Y^b - 2VTR_F\sqrt{I_X^b I_Y^b} \end{aligned} \tag{5.10}$$

where VT is the visibility which would be measured by a perfect balanced instrument. Calculating the reduced intensity as defined in equation 5.1 (but ignoring arbitrary offsets for simplicity) we obtain the general formulae

$$I_{\text{red}} = \frac{I_X^a + I_Y^a - I_X^b - I_Y^b + 2VTR_F\left(\sqrt{I_X^a I_Y^a} + \sqrt{I_X^b I_Y^b}\right)}{I_X^a + I_Y^a + I_X^b + I_Y^b + 2VTR_F\left(\sqrt{I_X^a I_Y^a} - \sqrt{I_X^b I_Y^b}\right)} \tag{5.11}$$

Normally this relation is simplified with the assumption of a perfect beam combiner ($\left(I_X^a = I_X^b \equiv I_X\right) \wedge \left(I_Y^a = I_Y^b \equiv I_Y\right)$ and perfectly balanced telescopes $I_X = I_Y$ therefore equation 5.11 could be simplified to $I_{\text{red, perf2}} = VTR_F$. Of course, this assumption is not justifiable, instead we should assume a more general case and separate the V-dependent term in equation (5.11). But it is reasonable to assume at least $I_X^a I_Y^a \approx I_X^b I_Y^b$, so we can make the good approximation

$$\begin{aligned} I_{\text{red}} &\approx \frac{I_X^a + I_Y^a - I_X^b - I_Y^b + 2VTR_F\left(\sqrt{I_X^a I_Y^a} + \sqrt{I_X^b I_Y^b}\right)}{I_X^a + I_Y^a + I_X^b + I_Y^b} \\ &= 2VTR_F\left(\frac{\sqrt{I_X^a I_Y^a} + \sqrt{I_X^b I_Y^b}}{I_X^a + I_Y^a + I_X^b + I_Y^b}\right) + \text{constant} \end{aligned} \tag{5.12}$$

Since we are using the measured I_{red} to obtain the fitted fringe visibility μ, we can calibrate our data just by multiplying μ with a correction factor U to get the corrected visibility V as formalized in equation (5.2) with

Table 5.1: The correction equations for the different pixel pairs and the different cases.

Reduced Intensity	North Delayed Case	South Delayed Case
$I_{\text{red}}^{P0,P1}$	$U_{AC} = \frac{I_A^{P0}+I_C^{P0}+I_A^{P1}+I_C^{P1}}{\sqrt{I_A^{P0}I_C^{P0}}+\sqrt{I_A^{P1}I_C^{P1}}}$	$U_{BC} = \frac{I_B^{P0}+I_C^{P0}+I_B^{P1}+I_C^{P1}}{\sqrt{I_B^{P0}I_C^{P0}}+\sqrt{I_B^{P1}I_C^{P1}}}$
$I_{\text{red}}^{P2,P3}$	$U_{BC} = \frac{I_B^{P2}+I_C^{P2}+I_B^{P3}+I_C^{P3}}{\sqrt{I_B^{P2}I_C^{P2}}+\sqrt{I_B^{P3}I_C^{P3}}}$	$U_{AC} = \frac{I_A^{P2}+I_C^{P2}+I_A^{P3}+I_C^{P3}}{\sqrt{I_A^{P2}I_C^{P2}}+\sqrt{I_A^{P3}I_C^{P3}}}$
$I_{\text{red}}^{P4,P5}$	$U_{AB} = \frac{I_A^{P4}+I_B^{P4}+I_A^{P5}+I_B^{P5}}{\sqrt{I_A^{P4}I_B^{P0}}+\sqrt{I_A^{P1}I_B^{P1}}}$	$U_{BA} = \frac{I_B^{P4}+I_A^{P4}+I_B^{P5}+I_A^{P5}}{\sqrt{I_B^{P4}I_A^{P4}}+\sqrt{I_B^{P5}I_A^{P5}}}$

$$U_{XY} = \frac{I_X^a + I_Y^a + I_X^b + I_Y^b}{\sqrt{I_X^a I_Y^a} + \sqrt{I_X^b I_Y^b}} \tag{5.13}$$

In table 5.1, we present the correction equations for all possible cases. The values for all intensities must be estimated from the matrixfiles, which is the topic of the following subsection.

5.4.1 Reducing the Matrixfiles

The matrixfiles have exactly the same structure as the data files. So the first step in data reduction is again taking the derivative of the raw data supplied by PICNIC. A more negative signal corresponds to a higher measured flux on the CCD. Since the light intensity which reaches the camera from the baseline with open shutter is supposed to be constant for the individual pixels, we expect a stable signal. But as the example in figure 5.16 shows, there is a small drop in the intensity in the beginning of each scan (enlarged in figure 5.17). We suppose that this drop is caused by the initial reset of the camera.

Figure 5.16 shows the inequality we want to correct for: The averaged intensity $\langle I_{P2}^{M1} \rangle$ measured on pixel P2 (blue) in M1 is significantly stronger than the intensity $\langle I_{P2}^{M3} \rangle$ in M3. Possible reasons for these inequalities will be discussed in chapter 8.

Both of the above mentioned intensities still contain the dark current background due to the instrument alone. We have to subtract this background to obtain the quantity I_A^{P2} as required by the equation in table 5.1

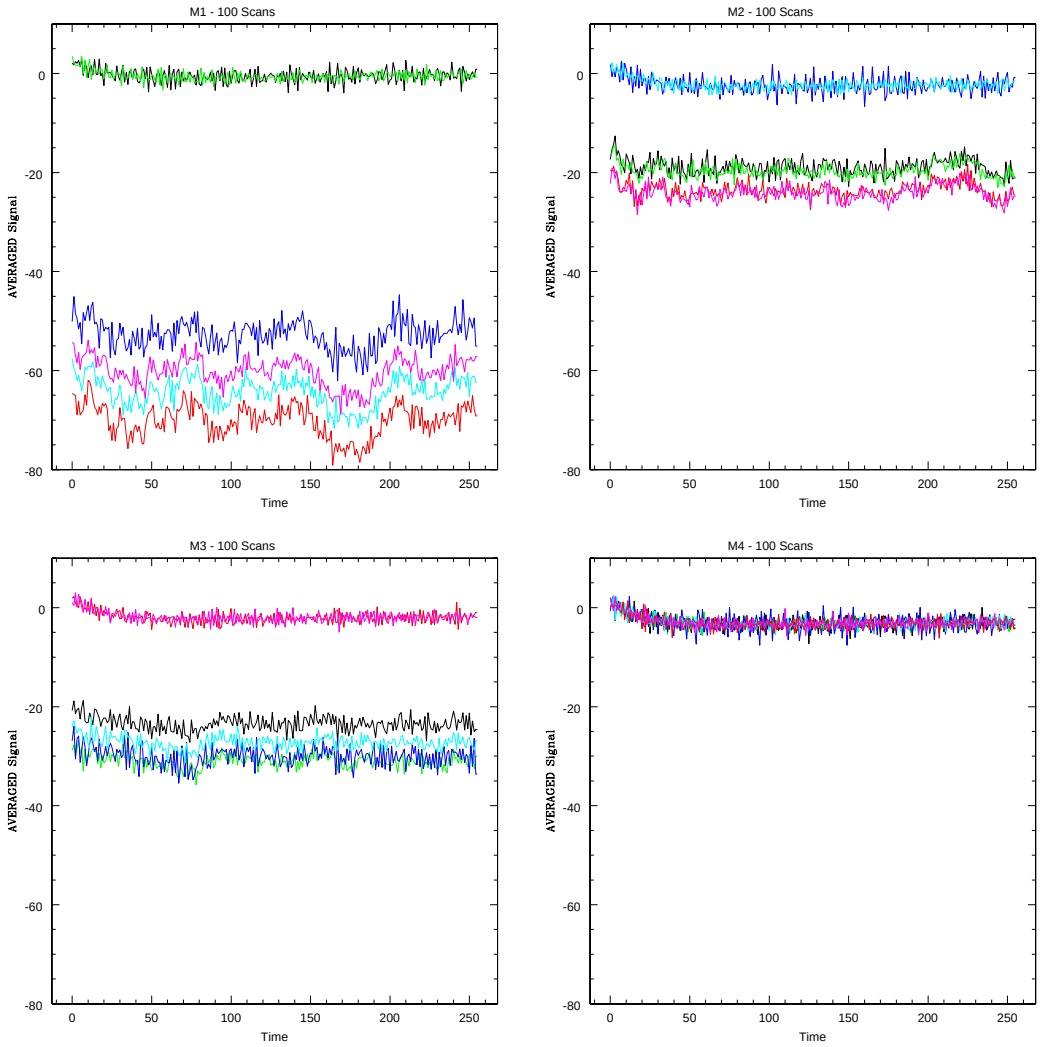

Figure 5.16: A sample for the signals in the matrixfi les (here 2002Nov14/117..120). Each signal was averaged over 100 scans. The abscissa have an arbitrary unit. Different colors represent the different pixels on PICNIC: P0=black, P1=green, P2=blue, P3=cyan, P4=red, P5=magenta

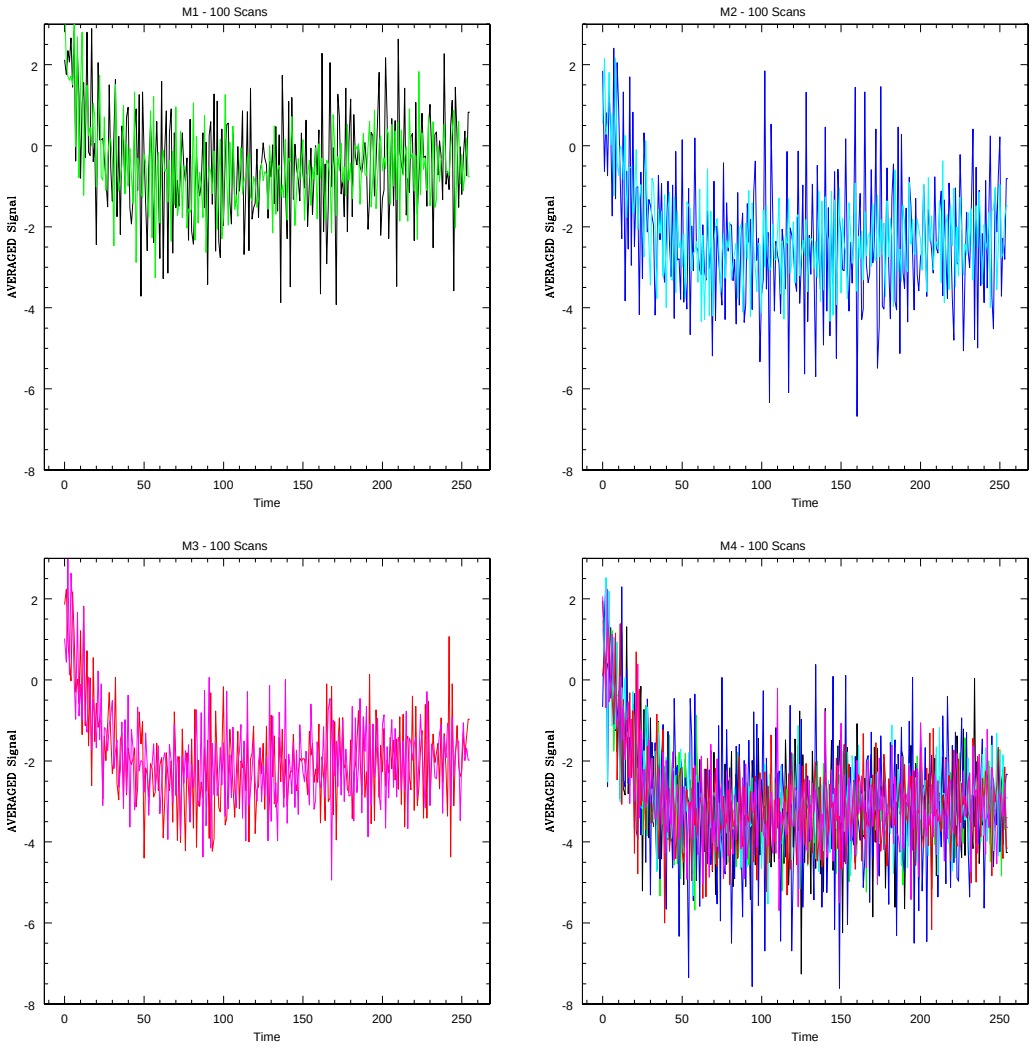

Figure 5.17: Same matrixfi les and options as in fi gure5.16, but with a different scale on the ordinate.

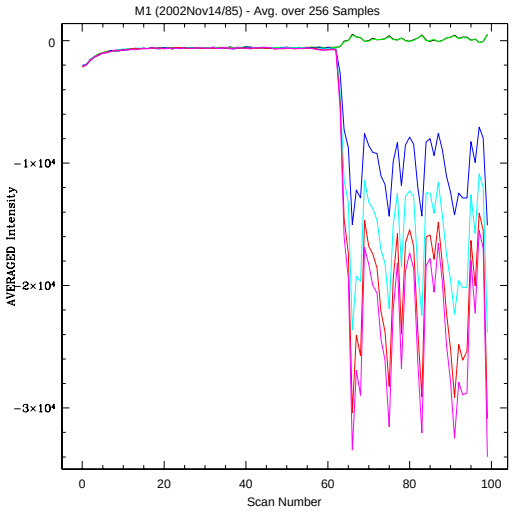

Figure 5.18: The intensity of each of the six pixels (different colors), averaged over all 256 samples within a scan. The ordinate gives the number of the scan within the matrixfile from 2002Nov14/85. It seems that the star light was not falling on the detector before Scan #65, but the user reacquired the star later during the acquisition of the matrix file manually. Please notice that the intensity in the "null"-levels (green and black) changes as soon as star light illuminates the other four pixels.

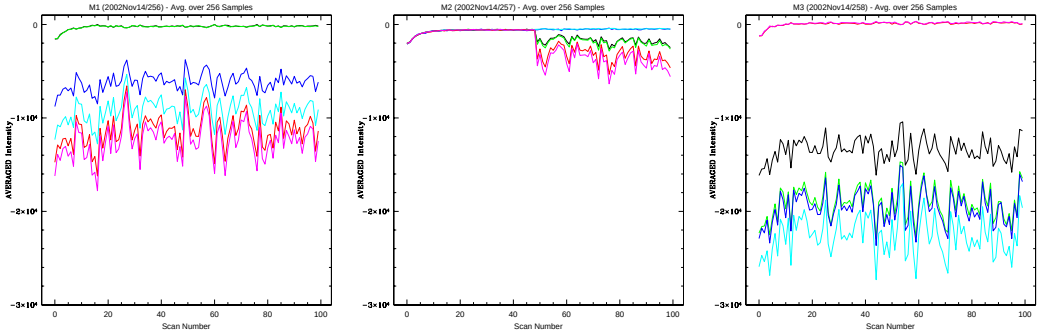

Figure 5.19: Same settings as in figure 5.18 but with the data from 2002Nov14/256..259. The ratio of flux in the BC (black/green) and BA (red/magenta) baseline between the different matrixfiles is so different that it must be assumed that the star was not being properly tracked during the acquisition of M2. Even when the algorithm ignores in M2 the scans before #49, the flux ratios between the six signals stays 1 : 9, 1 : 12, 1 : 3.4, 1 : 2.6, 1 : 3.5, 1 : 3.2!

(for this particular case the equation for the south-delayed case applies). Usually the "null-matrix" M4 would be used to obtain the average noise level for the individual camera pixels. However we discovered a peculiar effect which can be seen in figure 5.17: The averaged intensity in the null-matrix is significantly higher than in the other matrixfiles - even if the baselines are shuttered off in exactly the same way! Extended investigations showed that this relation always holds ($I_{M4} > I_{MX}$ for the shuttered out pixels on $X = 1,2,3$). There is a very illustrative case which confirms this effect as well: During the acquisition of the matrixfile shown in figure 5.18 the star was not being tracked by the star-tracker initially and the star light did not reach the camera pixels during the first 60 scans. Then the star tracker locked onto the star and simultaneously to the increase of the intensity on two baselines, the background falls off at the completely shuttered out baseline! Therefore the intensity measured by the six pixels is not independent! Since the intensity drops it can be ruled out that this behaviour is caused by light scattered from the illuminated pixels onto the dark pixels. Therefore we suspect the camera electronics as the originator of this undesirable effect. To avoid the situation that the real signal level may become lower than the background level we do not use the null-matrix M4 but the background levels in the remaining matrixfiles. So for the South Delayed Case (as in the earlier presented example) the relations for noise-subtraction become

$$
\begin{aligned}
I_A^{P2} &= \langle\langle I_{M1}^{P2}\rangle - \langle I_{M2}^{P2}\rangle\rangle & I_A^{P3} &= \langle\langle I_{M1}^{P3}\rangle - \langle I_{M2}^{P3}\rangle\rangle \\
I_A^{P4} &= \langle\langle I_{M1}^{P4}\rangle - \langle I_{M3}^{P4}\rangle\rangle & I_A^{P5} &= \langle\langle I_{M1}^{P5}\rangle - \langle I_{M3}^{P5}\rangle\rangle \\
I_B^{P0} &= \langle\langle I_{M2}^{P0}\rangle - \langle I_{M1}^{P0}\rangle\rangle & I_B^{P1} &= \langle\langle I_{M2}^{P1}\rangle - \langle I_{M1}^{P1}\rangle\rangle \\
I_B^{P4} &= \langle\langle I_{M2}^{P4}\rangle - \langle I_{M3}^{P4}\rangle\rangle & I_B^{P5} &= \langle\langle I_{M2}^{P5}\rangle - \langle I_{M3}^{P5}\rangle\rangle \\
I_C^{P0} &= \langle\langle I_{M3}^{P0}\rangle - \langle I_{M1}^{P0}\rangle\rangle & I_C^{P1} &= \langle\langle I_{M3}^{P1}\rangle - \langle I_{M1}^{P1}\rangle\rangle \\
I_C^{P2} &= \langle\langle I_{M3}^{P2}\rangle - \langle I_{M2}^{P2}\rangle\rangle & I_C^{P3} &= \langle\langle I_{M3}^{P3}\rangle - \langle I_{M2}^{P3}\rangle\rangle
\end{aligned}
$$

The all-embracing brackets denote the averaging over the whole 100 scans which are contained in one matrixfile whereas the inner brackets refer to the averaging over the 256 readouts within one scan. Especially the averaging over the 100 scans must be done carefully. It may happen that the star is lost by the star trackers (as in the case in figure 5.18). In those cases, simple averaging will result in an underestimation of the overall averaged intensity and therefore in a correction factor which is too large! My data reduction program reconstructs those matrixfiles by separating over those scans which contain clearly signal. When the star was lost during the whole or a dominant part of the matrixfile acquisition, the matrixfile is rejected

and the correction factor cannot be calculated. There are other cases like the one from 2002Nov14/256..259 (Figure 5.19) where the flux in the baselines between the different matrixfiles is such as unbalanced (in this case 1 : 12) that one must suppose that the star was not properly locked by the star tracker during the acquisition of at least one of the matrixfiles. Therefore we had to choose a threshold ratio beyond which matrixfiles are rejected (e. g. 1 : 4).

5.4.2 Applying the Correction

When all four averaged intensities are known for one baseline, the correction factor U_{XY} can be calculated using table 5.1. To demonstrate that for the sample case, we may calculate the specific values for U_{BC}:

$$\begin{aligned} I_B^{P0} &= 18.46 \qquad I_B^{P1} = 22.99 \\ I_C^{P0} &= 19.12 \qquad I_C^{P1} = 30.48 \end{aligned}$$

so the correction becomes

$$U_{BC} = \frac{22.99 + 18.46 + 19.12 + 30.48}{\sqrt{22.99 \times 18.46} + \sqrt{19.12 \times 30.48}} = 1.0175$$

The other baselines are working analogously. For the North Delayed Case another set of equations comparable to equations 5.14 must be used but those can be easily obtained applying the same underlying concept.

If we recall the fringe visibilities in figures 5.11 and 5.14, obtained with two completely different methods leading to remarkably similar results, one may come to the conclusion that the remaining small scale ($\approx 5\%$) fluctuations are the result from imbalances between the telescopes. Therefore we calculated the correction factors for all baselines and all observations, setting no threshold for extreme flux ratio imbalances (as discussed in the last section in context with Figure 5.19). The resulting correction factors can be seen in figure 5.20. Those corrections are too large obviously, so the earlier mentioned problem of unrealistic flux ratios cannot be neglected (figure 5.19). It seems that in a large fraction of our observations the star tracker was not able to lock the star properly. But it is also problematic to reject those files and simply to assume $U = 1$ because this will just increase the scattering between the measurements. For the following chapters we used therefore the uncorrected data assuming $U = 1$ for all scans. Nevertheless we present also the result when one sets the arbitrary flux ratio threshold for rejection to 1 : 4 (see figure 5.21). Since a large fraction

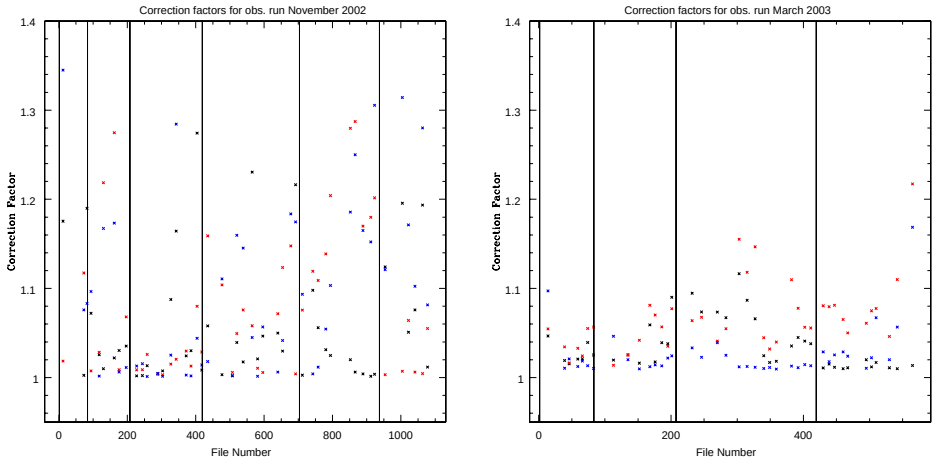

Figure 5.20: Calculated correction factors U for the observation runs in November 2002 (left) and March 2003 (right). The different colors correspond to the three baselines. Some individual values exceeded even the 1.4 border.

of the matrixfiles were rejected, we won't expect any observable improvement concerning the scattering of the calibrators compared to figure 5.11.

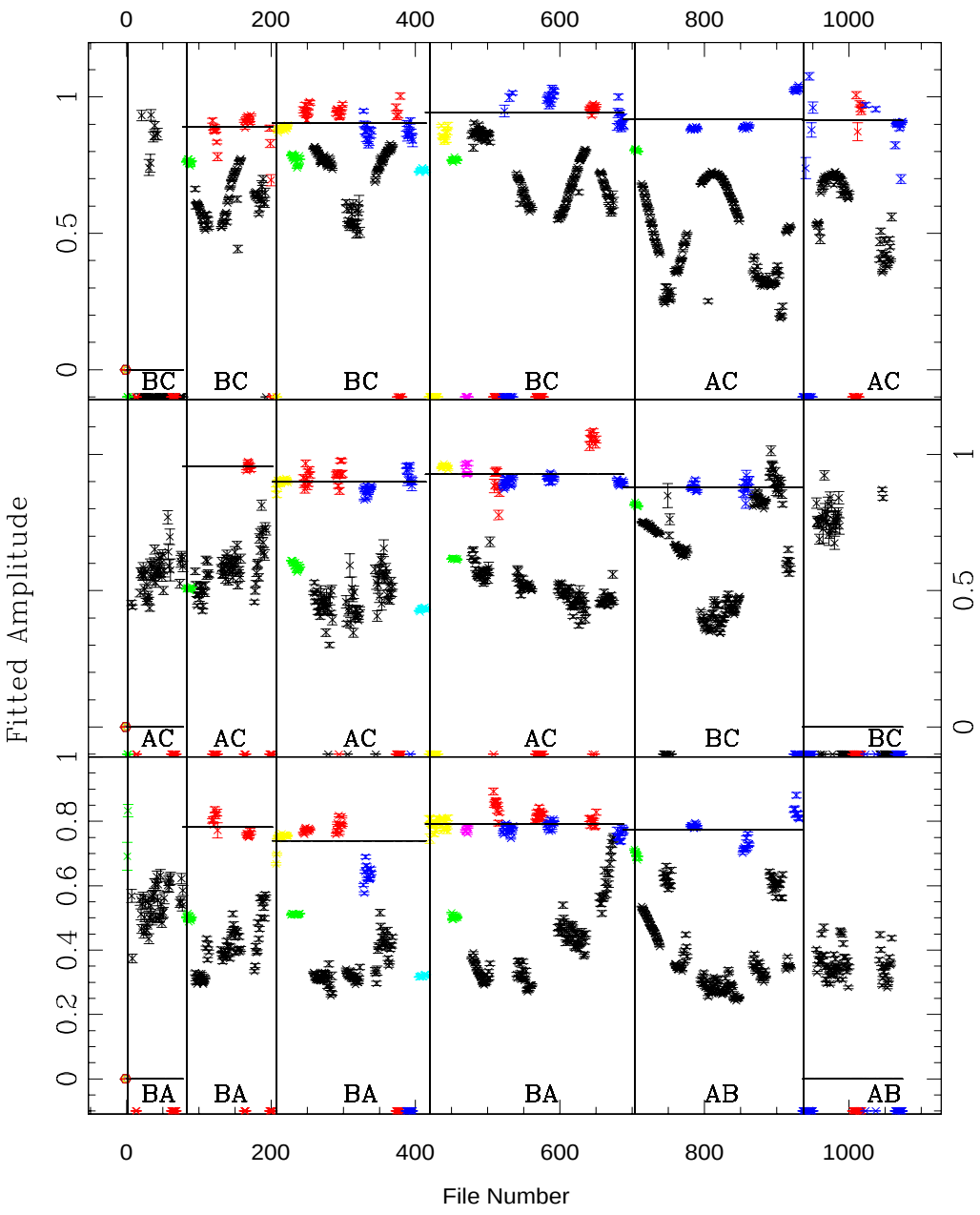

Figure 5.21: Fringe Visibilities obtained using the Envelope Fitting method after correction for imbalance between pixels. All matrixfi les with flux ratios above 1 : 4 were rejected. For comparison see fi gure 5.11

5.5 Extracting the Closure Phase

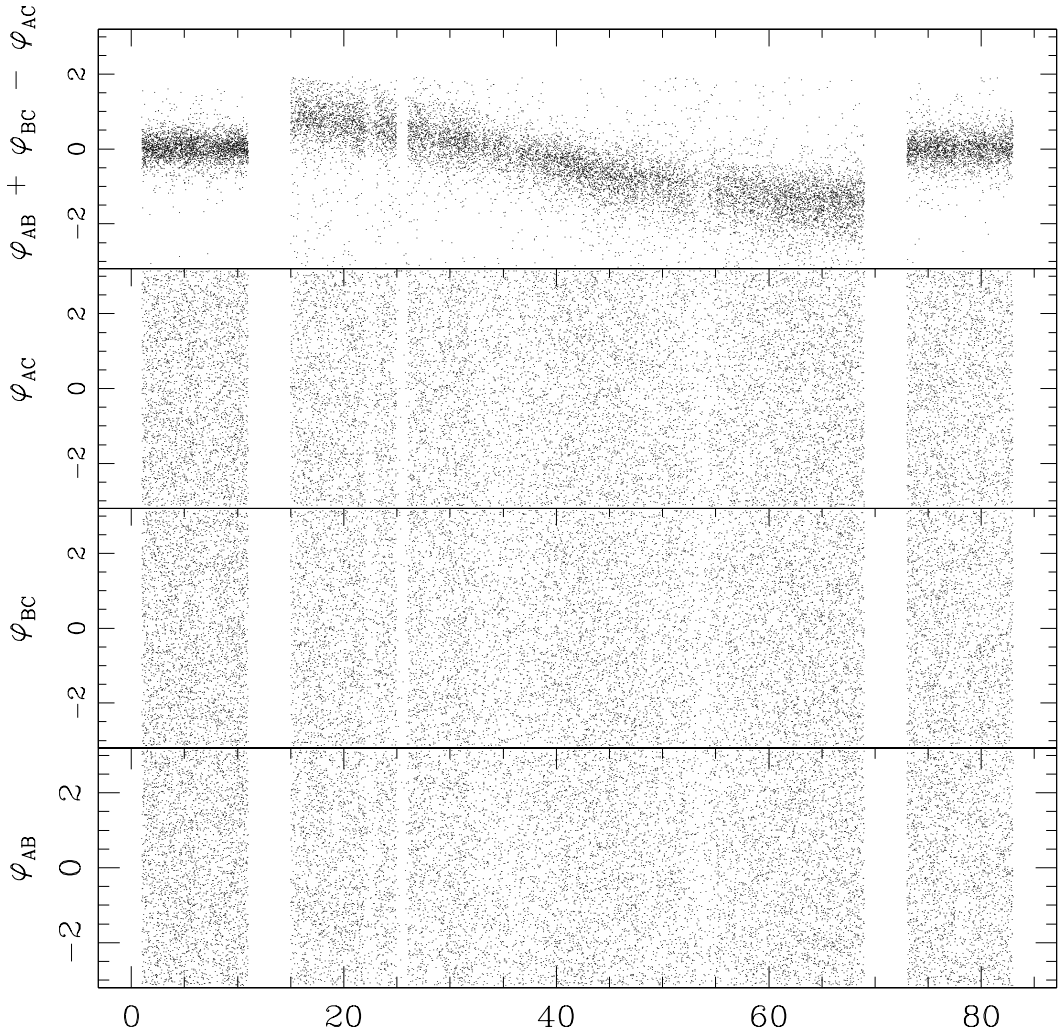

Figure 5.22: The individual phases and the closure phase of the unresolved calibrator δ Aur (left: scan 0..13 and right: scan 72..85) and the resolved binary Capella in between. Data from 2002Nov15/88..169

To estimate the closure phase, we use a quite intuitive method which provides excellent results. As discussed in chapter 2.6, the closure phase measurement has to be done within a time interval shorter than the coherence time of the atmosphere t_0. Therefore we estimate the positions of the fringes for all three baselines with the *IOTA-Ames Fringe Tracker* (Wil02) and average those positions to obtain a position within the scan which would be most likely to contain high power in all three fringes. Then we set a window around

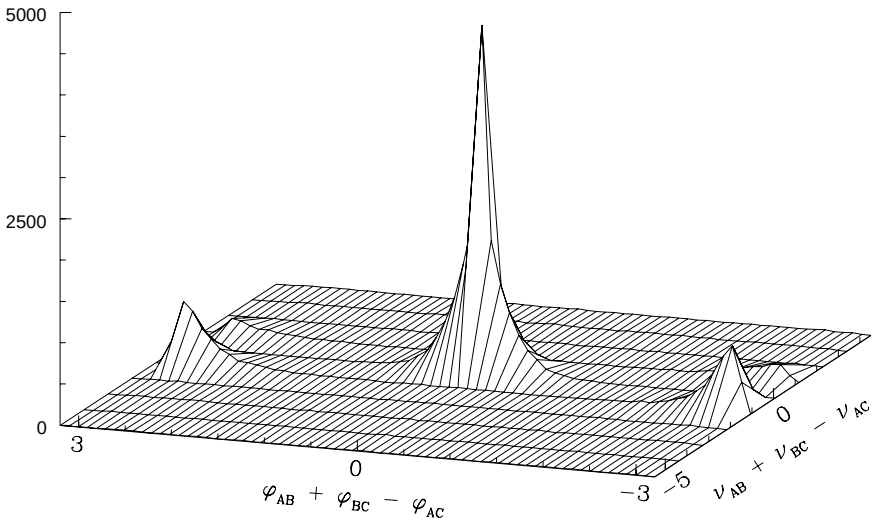

Figure 5.23: Histogram of Frequency Closure against the measured Closure Phase: The closure phase measurements which fulfi ll the frequency closure relation $\nu_{closure} = 0$ scatter less and show a nice Gaussian distribution. The histogram was produced using a large number of calibrators: 2002Nov13/166..207 and 2002Nov14/0..54

this averaged position. The size Δ_W of this window must be chosen carefully to fulfill the earlier mentioned condition $\Delta_w \delta\tau < t_0$ (we choose $\Delta_W = 32$ readouts). After calculating the FFT of all three windowed scans, one can search the position of the peak ν_{XY} within the power spectrum (so ν_{XY} will be discrete) and calculate the phases φ_{AB}, φ_{BC}, φ_{CA} with $\varphi_{XY} = tan^{-1}[\Im(\mathcal{F}(I_{\rm red}(\nu_{XY})))/\Re(\mathcal{F}(I_{\rm red}(\nu_{XY})))]$. The closure phase Φ is then given by equation 2.20. Figure 5.22 shows the individual phases and the closure phase for one calibrator-target-calibrator sequence. We expect also a frequency closure relation $\nu_{closure} = 0$ with

$$\nu_{closure} = \nu_{AB} + \nu_{BC} + \nu_{CA} \tag{5.14}$$

This frequency closure relation can be used to reject individual measurements of lower quality. As figure 5.23 shows, those points which satisfy the frequency closure relation yield a nice Gaussian distribution. Therefore our algorithm rejected those measurements where $\nu_{closure} \neq 0$.

Finally the individual closure phase estimations Φ_i ($0 \leq i \leq N_{datafile}$) for all scans within a datafile are aver-

aged. To obtain $\langle\Phi\rangle$ it is important to take the 2π periodicity of the phase into consideration. After bringing all Φ_i in the range $[0, 2\pi]$, a proper averaging method would be

$$\begin{aligned}
\langle\Phi\rangle_1 &= \frac{1}{N}\sum_{i=1}^{N}\Phi_i \\
\langle\Phi\rangle_2 &= \frac{1}{N}\left(\sum_{\forall i:\Phi_i\leq\pi}\Phi_i + \sum_{\forall i:\Phi_i>\pi}(\Phi_i - 2\pi)\right) \\
\sigma_1^2 &= \frac{1}{N-1}\left(\sum(\Phi_i^2) - N(\langle\Phi\rangle_1)^2\right) \\
\sigma_2^2 &= \frac{1}{N-1}\left(\sum_{\forall i:\Phi_i\leq\pi}(\Phi_i^2) + \sum_{\forall i:\Phi_i>\pi}(\Phi_i - 2\pi)^2 - N(\langle\Phi\rangle_2)^2\right) \\
\langle\Phi\rangle &= \begin{cases} \langle\Phi\rangle_1 & : \quad \sigma_1 \leq \sigma_2 \\ \langle\Phi\rangle_2 & : \quad \text{otherwise} \end{cases}
\end{aligned} \tag{5.15}$$

The closure phase may show an arbitrary offset so our data reduction software subtracts the average of the closure phases of all calibrators. The final result for both observation runs can be seen in figure 5.24.

a) November 2002

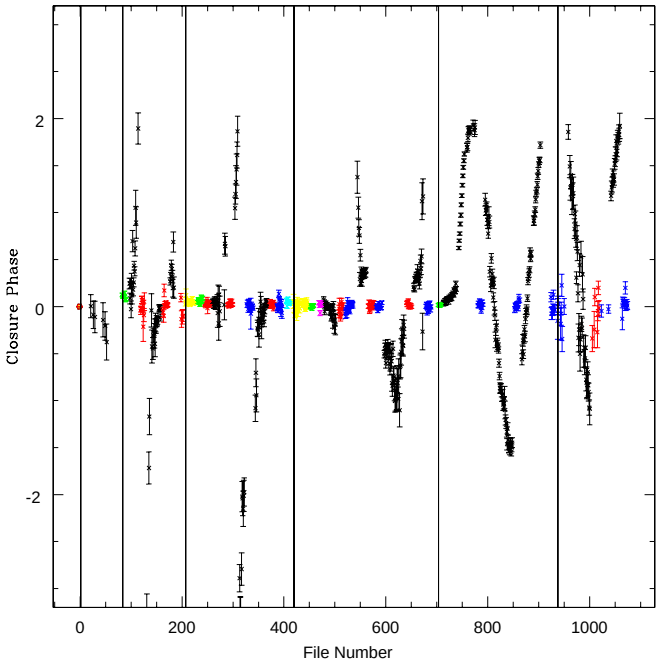

b) March 2003

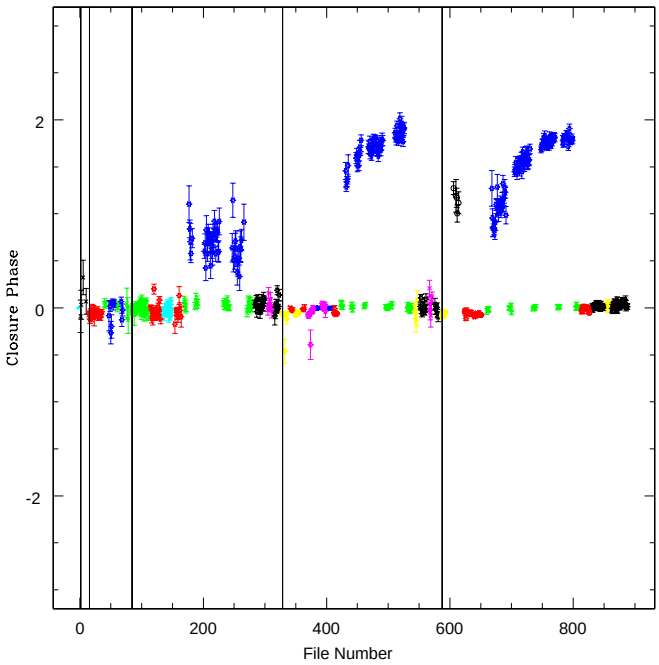

Figure 5.24: Closure Phases from the observation run in November 2002. Measurements which showed an error larger than 0.2 were rejected. The vertical lines separate the different nights whereas the horizontal lines give the average of the unresolved calibrator stars. Color Code: see table 4.2. Due to a change in the confi guration (North/South Delayed Case), the closure phase sign changes for the last two nights in November 2002.

Chapter 6

Model Fitting

6.1 Position of Components in Binary Systems

In order to obtain quantitative information about the observed targets, a first step is to fit simple sky brightness distribution models to the measured visibility and closure phase information. The fundamental mathematics for those fits was given in equations (2.22), (2.29) and (2.30). A separate modeling program was developed which fits binary star models with two uniformly bright disks directly to the output file from the data reduction software.

Our fit algorithm minimizes χ^2 which can depend both on visibilities and closure phases. To weight both independent quantities equally, we use:

$$\begin{aligned}
\chi^2 &= 2\pi\chi_V^2 + \chi_\Phi^2 \\
\chi_V^2 &= \frac{N_V}{N_V + N_\Phi} \sum_{i=1}^{N_V} \left(\frac{V_i^2 - V_{model}^2}{\sigma_V} \right)^2 \\
\chi_\Phi^2 &= \frac{N_\Phi}{N_V + N_\Phi} \sum_{i=1}^{N_\Phi} \left(\frac{\Phi_i - \Phi_{model}}{\sigma_\Phi} \right)^2
\end{aligned}$$

Including the closure phases into the fit is especially helpful in order to avoid the *quadrant error* which arises from the $V(u,v) = V(-u,-v)$ symmetry of the uv-plane. For some nights the closure phase measurement was poor so we fitted only the visibilities in those cases. Our error estimation for the visibility measurements include the statistical error as given by the scattering of the individual measurements within each datafile and an additional calibration error given by the scattering of the calibrators during one night. As a first

Table 6.1: Measured Diameter of resolved calibrators. Data from November 2002 reduced with the Fringe Envelope Fitting Algorithm.

Object	Imbalance Corr.	Data Points N_V	Fitted Diameter [mas]	Reference Diameter [mas] (Ric02)
α Cas	no	107	5.53 ± 0.12	6.25 ± 0.31
|	yes	107	6.07 ± 0.11	6.25 ± 0.31
α Lyn	no	29	6.82 ± 0.19	9.24 ± 1.02
|	yes	29	6.96 ± 0.18	9.24 ± 1.02

step, we fixed the stellar radii to fit for the positions of the components, using previously measured radii from (Hum94) as an initial guess for the Capella giants. For λ Vir we assumed point sources. The fitted positions are not very sensitive to the intensity ratio (a change in I_{Ab}/I_{Aa} of ± 0.5 results typically in a change in the position of less than 0.5 mas). This is different for fits with a small number of measurements as for our one Capella observation in March 2003. In those cases one might not perform a grid search for the global minima but rather fit with a concrete initial guess.

All nights were fitted separately with the position and intensity ratio as free parameters. Our best-fit results are listed in table 6.2 and 6.3. The positions may be compared with the predictions by (Hum94) (for orbital elements see table 4.2). The errors on those fits were estimated by fitting parabolas to the reduced χ^2_{red} of fits with modified intensity ratio (Brute Force Least Square Fit as described in (Schlo)). Calculating the weighted average and its error obtains the overall best fit intensity ratios of (1.44 ± 0.23) for Capella (using Data from November 2002) and (2.06 ± 0.19) for λ Vir.

6.2 Stellar Diameters

Just by fitting the function given in equation (2.22) to the measured visibilities one can estimate stellar diameters. We did those fits for the Capella giants as well as for the clearly resolved calibrators α Cas and α Lyn. For the resolved calibrators we had to extrapolate the transfer function since there are typically no directly neighbouring observations of unresolved calibrators. To obtain the averaged transfer function we averaged T for all unresolved calibrators from the same nights.

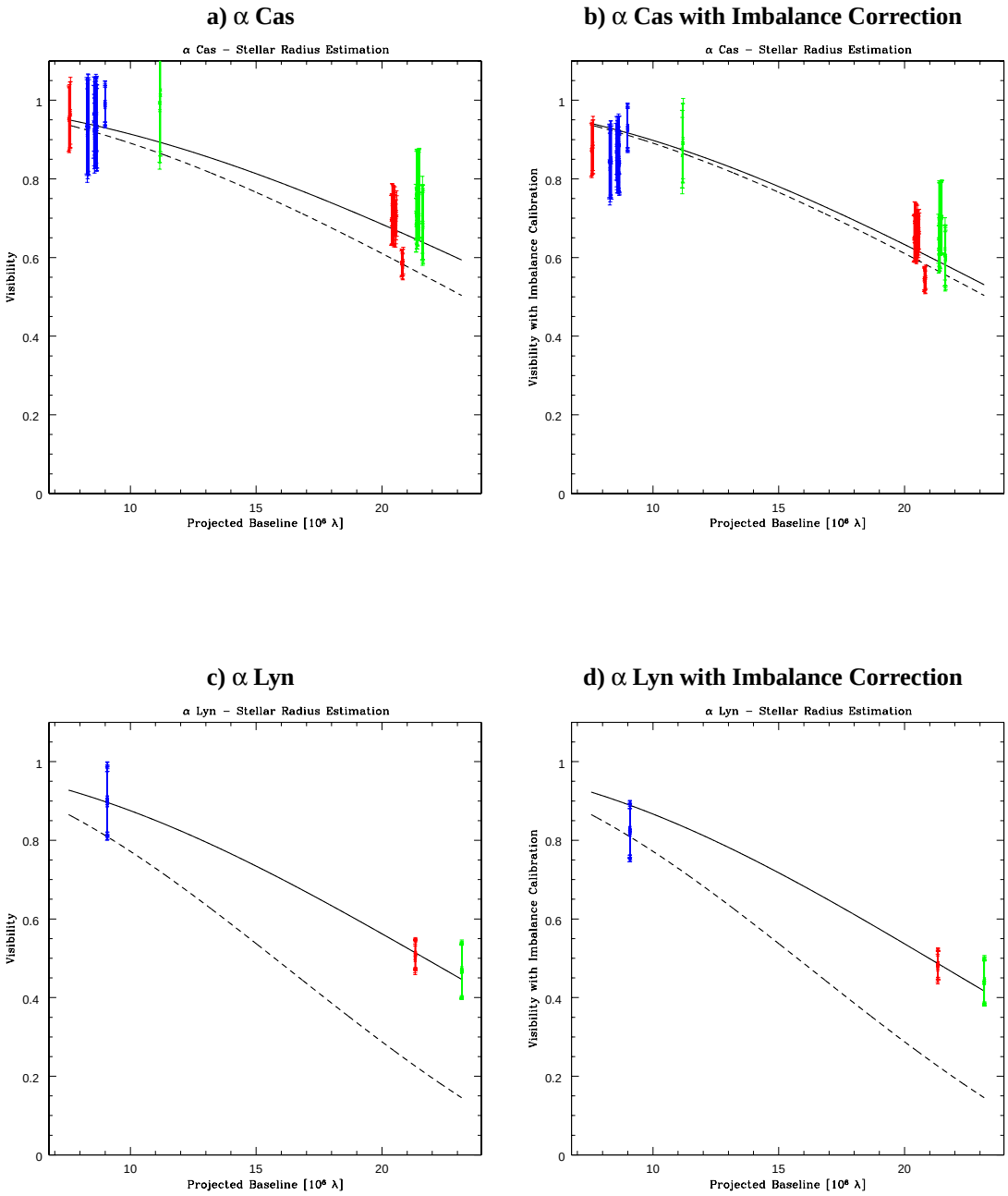

Figure 6.1: Stellar diameter fi ts for the resolved calibrators α Cas and α Lyn with data taken in November 2002, reduced with the envelope fi tting algorithm. In fi gure b) and d) the imbalance correction was applied with an arbitrary flux-ratio-threshold of 1 : 4. Different colors indicate measurements on different baselines: blue (AC/BC), red (BC/AC), green (AB/BA) for (North Delayed/South Delayed Case)

Table 6.2: Fitting Results for **Capella**. MJD=JD-2452500

Data from Night		Data Points		χ^2_{red}		Fitted I_{Ab}/I_{Aa}	Fitted Diam.		Fitted Position[1]		Ref. Pos.[1] (Hum94)	
Date	MJD	N_V	N_Φ	χ^2_V	χ^2_Φ		D_{Aa}	D_{Ab}	dRA [mas]	dDEC [mas]	dRA	dDEC
11/12/02	90.821 ... 91.046	180	52	4.8	4.9	1.28 ± 0.62	8.4 ± 1.7	5.6 ± 2.5	-9.28 ± 0.24	44.82 ± 0.11	-8.93	44.70
11/13/02	91.805 ... 91.978	261	66	5.3	28.1	1.35 ± 0.33	8.5 ± 1.1	6.5 ± 1.4	-12.81 ± 0.24	44.14 ± 0.17	-11.67	43.25
11/14/02	92.744 ... 93.026	291	105	6.1	32.5	1.28 ± 0.58	8.3 ± 0.9	5.8 ± 1.4	-13.89 ± 0.35	41.27 ± 0.18	-14.47	41.60
11/15/02	93.797 ... 94.042	369	107	8.3	12.3	1.92 ± 0.99	8.0 ± 2.9	8.0 ± 4.8	-17.87 ± 0.30	39.37 ± 0.19	-17.33	39.72
11/16/02	94.883 ... 95.034	170	57	0.4	5.0	1.88 ± 0.62	8.4 ± 0.8	7.2 ± 2.0	-20.12 ± 0.10	37.75 ± 0.11	-20.13	37.68
03/24/03	222.677 ... 222.704	47	17	2.04		1.60 ± 0.31	8.6	7.8	-44.37 ± 1.65	-27.05 ± 3.12	-46.40	-28.23

[1] Relative Positions are measured from the brighter to the fainter component.

Table 6.3: Fitting Results for λ **Vir**. MJD=JD-2452500

Data from Night		Data Points		χ^2_{red}	Fitted I_B/I_A	Fitted Position	
Date	JD	N_V	N_Φ			dRA [mas]	dDEC [mas]
03/21/03	219.852 ... 219.887	188	59		([2])	-1.75 ± 0.60	-18.07 ± 0.52
03/22/03	220.855 ... 220.950	113	55		([2])	0.64 ± 0.10	-19.32 ± 0.09
03/23/03	221.875 ... 221.956	139	54	4.93	2.18 ± 0.44	-0.99 ± 0.20	-17.40 ± 0.10
03/24/03	222.828 ... 222.937	208	90	1.01	2.03 ± 0.24	-1.09 ± 0.01	-17.29 ± 0.01
03/21/03 ... 03/24/03	219.852 ... 222.937	648	258	3.94	2.04 ± 0.08	-1.38 ± 0.08	-17.39 ± 0.02

[2] Since the intensity ratios for those fits did not converge, the fitted position for the overall best-fit $I_B/I_A = 2.06$ is given.

Our best fit diameters and statistical errors are given in table 6.1. Figure 6.1 shows the fitted data together with the visibility curves for our diameter estimations and the measured diameters given by (Ric02). For α Lyn there is a significant discrepancy between our measurement and the reference measurement. This may be explained by the lack of a proper imbalance correction as described in chapter 5.4.2. We fitted also the imbalance corrected data given in figure 5.21 which brought some points in our stellar diameter fit slightly closer to the reference measurement. It is important to mention that all α Lyn measurements were taken on the night of 11/13/02 at the break of dawn and are not followed by the measurement of an unresolved calibrator. Considering those two possible sources of error it is valid to accept a large but unknown systematical error for the α Lyn measurement. The α Cas measurement agrees with the reference measurement within the 1σ uncertainty.

For the Capella binary system we fixed the fitted positions and found the diameters with best χ^2 again for visibilities and closure phases simultaneously. The results are listed in table 6.2. After averaging all nights we obtain diameters of $D_{Aa} = (8.4 \pm 0.2)$ mas and $D_{Ab} = (6.3 \pm 0.7)$ mas which is consistent with the measurements by (Hum94) ($D_{Aa} = (8.5 \pm 0.1)$ mas and $D_{Ab} = (6.4 \pm 0.3)$ mas).

6.3 Derived Physical Parameters

Using the results from the last section, one can derive additional physical parameters. With the Hipparcos measurement of the distance d to Capella (see chapter 4.2) we can calculate the physical radii of the stars to $R_{Aa} = (11.7 \pm 0.3) R_\odot$ and $R_{Ab} = (8.8 \pm 1.0) R_\odot$.

To obtain an estimate for the effective temperatures we proceed as in (You99) and use the flux ratios measured by IOTA in the H band and COAST in the J band to obtain the $m^J - m^H$ color for each star. Starting with the fundamental equations

$$\begin{aligned} m^J_{Aa} - m^H_{Aa} &= -2.5 \log \left(\frac{I^J_{Aa}}{I^H_{Aa}} \right) \\ m^J_{Ab} - m^H_{Ab} &= -2.5 \log \left(\frac{I^J_{Ab}}{I^H_{Ab}} \right) \\ m^J_{Aa+Ab} - m^H_{Aa+Ab} &= -2.5 \log \left(\frac{I^J_{Aa+Ab}}{I^H_{Aa+Ab}} \right) \end{aligned}$$

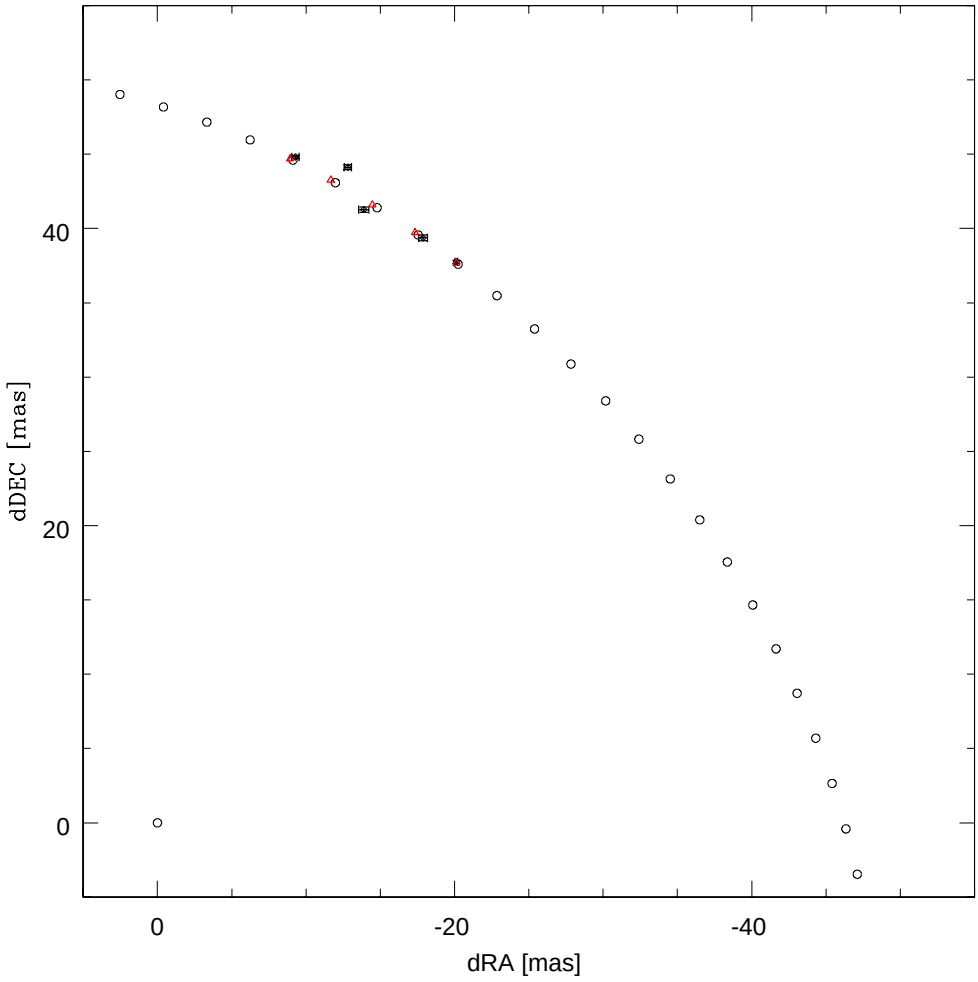

Figure 6.2: Fitted and Reference Positions (Hum94) for Capella: The circles indicate the relative position of the Aa component around the fixed Ab component (lower-left corner) along one whole orbit with one day intervals. The diameter of the circles does not represent the size of the star disks. The red triangles are the position in the middle of the observated nights and the black triangles with error bars indicate our measurements.

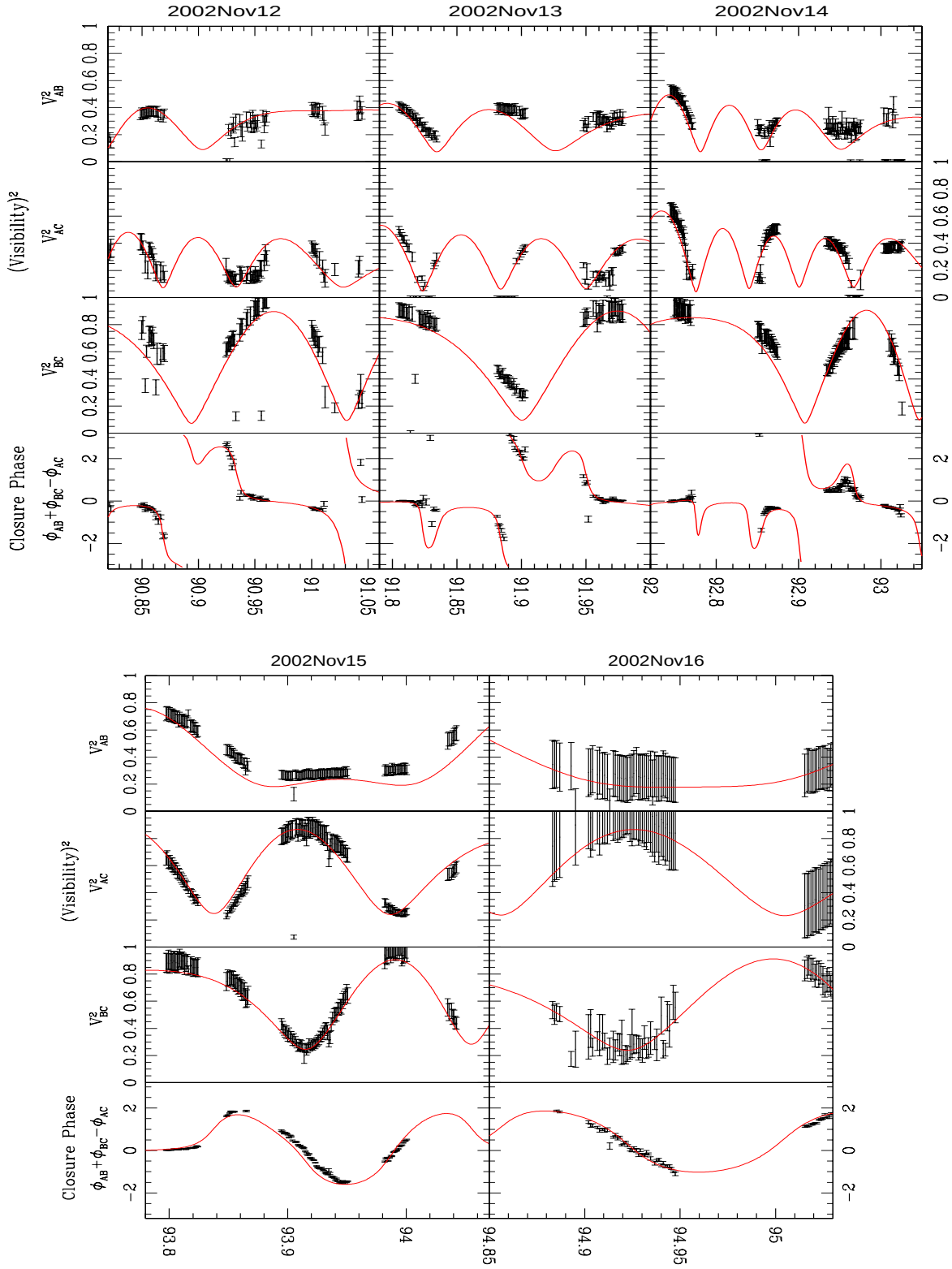

Figure 6.3: Best-fi t models for Capella assuming uniform disks with parameters as listed in table 6.2. Statistical and calibrational errors are shown. The abscissa depicts MJD=JD-2452500 and the CP is given in radians.

Table 6.4: Derived Physical Parameters for Capella

Parameter	Capella Aa	Capella Ab
Radius [$R_\odot$]	11.7 ± 0.3	8.8 ± 1.0
Absolute Brightness V-band [mag]	$0\overset{m}{.}29 \pm 0\overset{m}{.}05$	$0\overset{m}{.}18 \pm 0\overset{m}{.}06$
Effective Temperature T_{eff} [K]	5020^{+100}_{-90}	5730^{+220}_{-180}
Bolometric Luminosity L [$L_\odot$]	77.0 ± 1.8	74.0 ± 6.5

one obtains

$$m^J_{Aa} - m^H_{Aa} = m^J_{Aa+Ab} - m^H_{Aa+Ab} - 2.5\log\left(\frac{1+I^H_{Ab}/I^H_{Aa}}{1+I^J_{Ab}/I^J_{Aa}}\right) \tag{6.1}$$

$$m^J_{Ab} - m^H_{Ab} = m^J_{Aa+Ab} - m^H_{Aa+Ab} - 2.5\log\left(\frac{1+I^H_{Aa}/I^H_{Ab}}{1+I^J_{Aa}/I^J_{Ab}}\right) \tag{6.2}$$

We use the photometric data from (Nog81) with $m^J_{Aa+Ab} = -1\overset{m}{.}42$ and $m^H_{Aa+Ab} = -1\overset{m}{.}77$ and get $m^J_{Aa} - m^H_{Aa} = 0\overset{m}{.}44$ and $m^J_{Ab} - m^H_{Ab} = 0\overset{m}{.}20$. Since there is no error information provided by our resources we cannot provide error estimations and have to use it as a rough approximation. To relate the infrared colors to effective temperatures T_{eff} we make use of the work by (Bel89) and get rough estimates for the Capella giants: $T_{\text{eff},Aa} \approx 5500K$ and $T_{\text{eff},Ab} \approx 6500K$.

The absolute brightness of both components together can be obtained with the relation $M = m - 5\log(d/10pc)$ using the apparent brightness in the V band $m^V_{Aa+Ab} = 0.041$ (Kri90) which obtains $M^V_{Aa+Ab} = -0\overset{m}{.}52 \pm 0\overset{m}{.}03$. Averaging the V band intensity ratio from several observers (see chapter 4.2) gives $I^V_{Ab}/I^V_{Aa} = 0.90 \pm 0.03$ and $M^V_{Aa} = 0\overset{m}{.}29 \pm 0\overset{m}{.}05$; $M^V_{Ab} = 0\overset{m}{.}18 \pm 0\overset{m}{.}06$ using the overall luminosity $L^V_{Aa+Ab} = (129.4 \pm 3.6)L_\odot$. With the measured abundance $[Fe/H] = 0.43$ from (Bri00) and our diameter measurements we can apply the bolometric correction for giant stars from (Alo99) and solve for the effective temperatures and the bolometric luminosities simultaneously via iteration:

$$\begin{aligned} BC &= \frac{-5.531 \times 10^{-2}}{X} - 0.6177 + 4.420X - 2.669X^2 \\ &\quad + 0.6943X[Fe/H] - 0.1071[Fe/H] - 8.612 \times 10^{-3}[Fe/H]^2 \end{aligned} \tag{6.3}$$

$$M_{bol} = M_V + BC = -2.5\log(L/L_\odot) + 4\overset{m}{.}76 \tag{6.4}$$

$$L = 4\pi R^2 \sigma T^4_{\text{eff}} \tag{6.5}$$

where σ is the STEFAN-BOLTZMANN constant and $X = \log(T_{\text{eff}}) - 3.52$.

We obtain a bolometric luminosity of the whole system of $(151.0 \pm 6.7) L_{\odot}$ (see table 6.4). Both independent methods lead to the result that Ab is the hotter component. Those results fit very well to typical temperature scales for class III stars. (Alo99) lists typical effective temperatures of (4860 ± 130) K for G8 III stars (as Capella Aa) and (5306 ± 265) K for G2 III, which is close to G1 III (Capella Ab). The large error for the effective temperature of the Aa component results from our large uncertainty in the stellar diameter. We did not include errors due to the calibration for the bolometric correction itself as given in equation (6.3). Our results are in good agreement with (Hum94), who used completely independent resources, other equations for the bolometric correction and obtained $T_{\text{eff, Aa}} = (4940 \pm 50)$ K; $T_{\text{eff, Ab}} = (5700 \pm 100)$ K and $L_{Aa} = (78.5 \pm 1.2) L_{\odot}$; $L_{Ab} = (77.6 \pm 2.6) L_{\odot}$.

6.4 Wavelength-Dependency of the intensity ratio

As a result of the intense studies of the system over the last two decades, the intensity ratio of the Capella giants is known over a broad range of the electromagnetic spectrum. Therefore the spectral dependence of the intensity ratio can be modelled based on the parameters from our fitting results. As a simple model one can assume uniform bright disks, each emitting according to Planck's law like a black body $B_{\lambda}(T)$ of temperature T. The intensity ratio can then be written as

$$\left(\frac{I_{Aa}}{I_{Ab}}\right)(\lambda) = \frac{L_{Aa} R_{Aa}^2 B_{\lambda}(T_{Aa})}{L_{Ab} R_{Ab}^2 B_{\lambda}(T_{Ab})}$$

As can be seen in Figure 6.4, this model fits quite well with the earlier reported intensity ratios from the UV to the K-band as listed in chapter 4.2.

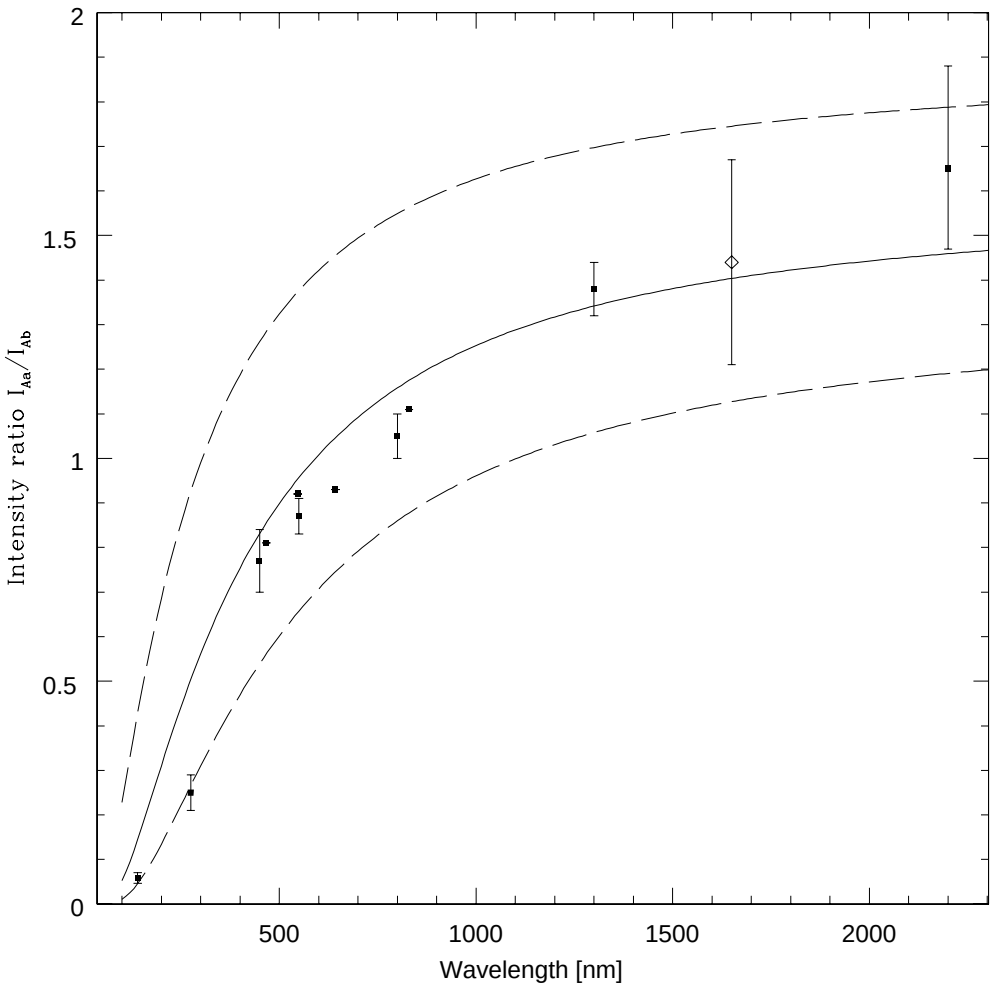

Figure 6.4: The intensity ratio I_{Aa}/I_{Ab} of the Capella giants as a function of wavelength. Our own measurement at 1650 nm (diamond) is plotted together with other data points from the literature (see text), even if not all references list errors. The lines show the modelled intensity ratio for two black bodies with the derived best-fi t temperatures and stellar diameters as given in table 6.4 (solid line) and the errors taking all uncertainties into account (dashed lines).

Chapter 7

Aperture Synthesis Mapping

7.1 Image Reconstruction Algorithms

7.1.1 Introduction

The radio astronomy community has developed many strategies to reconstruct images using measured closure phase information. In this work, we make use of the *Conventional Hybrid Mapping* (CHM) and the modified *Difference Mapping* (DFM) imaging algorithms. The underlying concept of both algorithms is the iterative self-calibration of the phases using closure phase information and a source model derived from the CLEAN algorithm applied to a map of the source or of the residuals.

Both algorithms make use of the *Clean Beam CB* (also *Point Spread Function (PSF)*) which represents the response of a point source to the uv-plane sampling obtained in the experiment. In practice we obtained the *CB* by fitting ellipses to different contour levels of the dirty beam *DB* (defined in equation (2.34)). Our fitting parameters for those ellipses are major and minor semi axes and the rotation angle. Two examples can be seen in figure 7.1.

7.1.2 Conventional Hybrid Mapping

In CHM we start without any concrete model and set two of the three phases to zero (which is equivalent to assuming a point source as source model). For each observation, the third phase is determined by the

2002 November 12..16

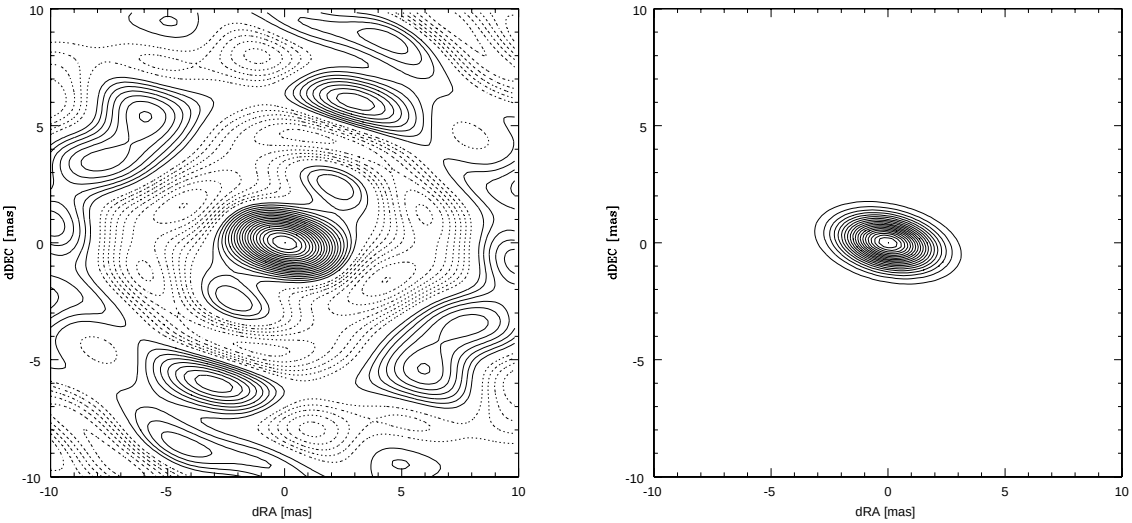

2003 March 21..24

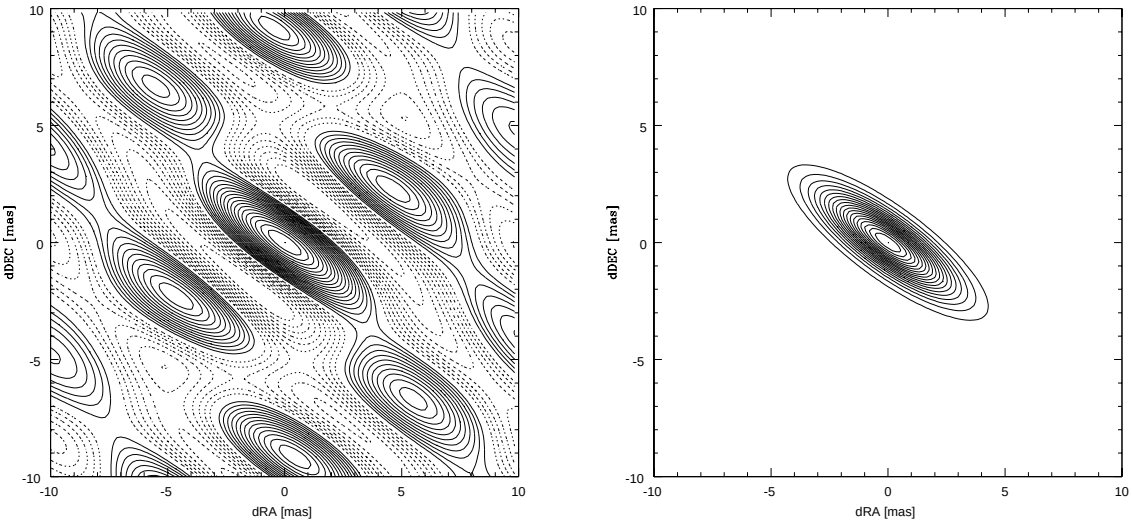

Figure 7.1: Dirty and Clean Beam for two examples. Only the central sector is shown.

closure phase relation given in equation (2.20). Using the measured visibilities we calculate the *DM* as defined by (2.32) and normalize it. In the CLEAN cycle, the weighted *DB* is subtracted iteratively from the *DM*. The weight-factor f for this subtraction is given by a constant gain-factor g times the peak intensity $DM_{max}(x_{max},y_{max})$ of the strongest feature within the map $f = g \cdot DM_{max}(x_{max},y_{max})$. The coordinates (x_{max},y_{max}) and intensities $DM_{max}(x_{max},y_{max})$ of those *Clean Components CC* are stored within a list. After a constant number N_{clean} of CLEAN steps are performed, the remaining features represent the residual *noise map NM*. By calculating the discrete Fourier transform (DFT) of the *CC*, the new phases are calculated using again the closure phase information (Self-Calibration). This procedure is repeated until convergence is reached. Finally the map may be shifted to the *center of light* since phase drifting during the hybrid mapping procedure may result in a movement of the features within the map.

7.1.3 Difference Mapping

The DFM approach tries to support the self-calibration process with an initial guess. This iterative process adds only positive or negative point sources to the *residual map RM*. Since not all phases are varied all at once, this algorithm tends to respond more smoothly and predictably. The difference to CHM is illustrated in figure 7.2: As an initial model we generate a *model map MM* which may contain two limb-darkened stellar disks. Then a DFT is performed in order to simulate the visibilities of this model map. By subtracting those modeled visibilities from the measured visibilities and performing the DFT we obtain the *RM*. Applying a small number of CLEAN steps on the *RM* will result again in clean components which can be added as δ functions in the form $RM_{max}(x_{max},y_{max}) \cdot \delta(x-x_{max},y-y_{max})$ to the *MM*. After cleaning, the remaining *RM* will be kept as noise map *NM*. With the modified model the algorithm is repeated until all residuals between the modeled and measured visibilities have vanished. Finally the *MM* is convolved with the *CB* and added to the *NM*.

7.1.4 Limiting Factors

Clearly, the advantage of the CHM algorithm is that it is completely model independent. But the proper convergence behaviour may be affected by the following effects:

a) The brightness distribution is too complex compared to the coverage of the uv-plane.

b) The source is very extended compared to the uv-plane coverage.

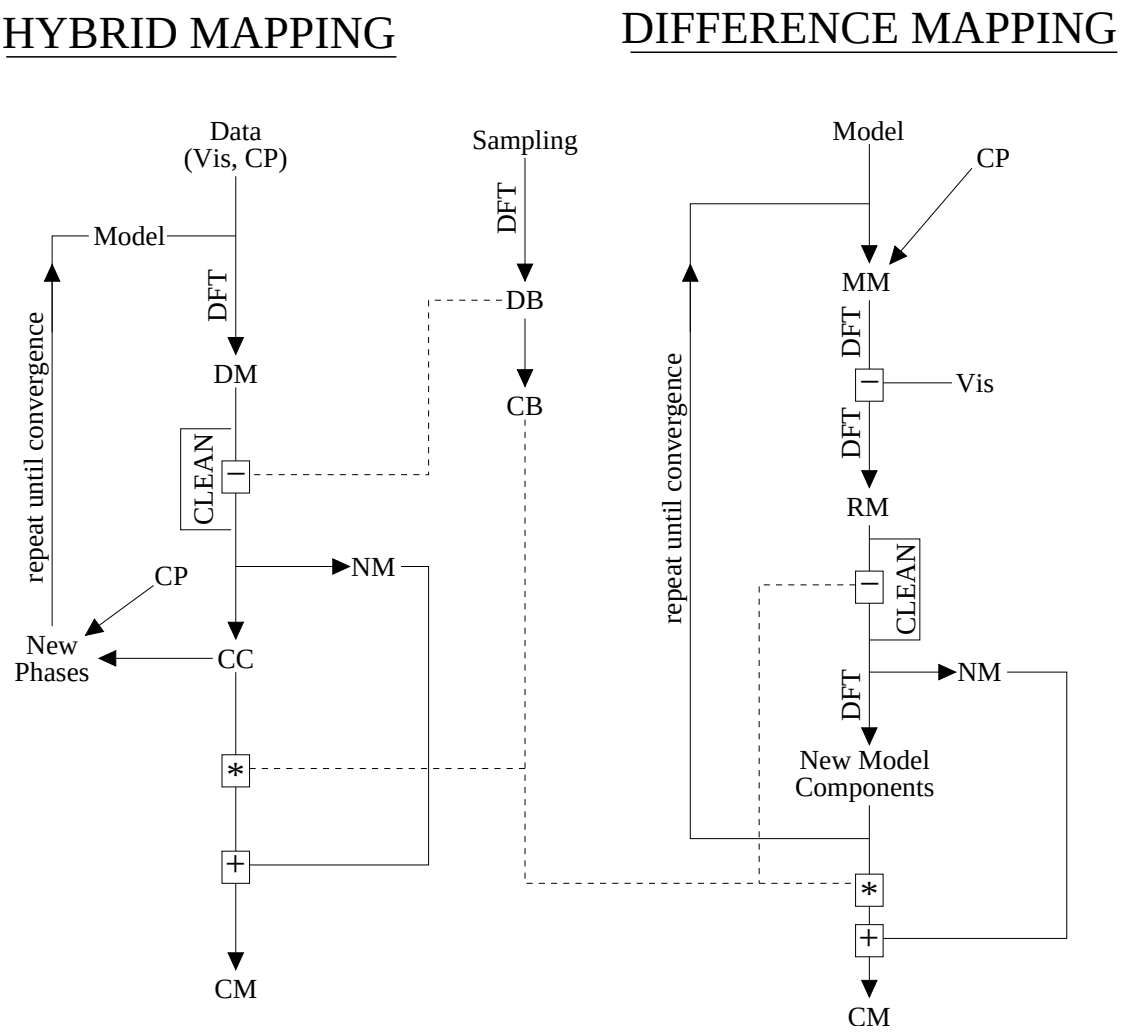

Figure 7.2: Hybrid Mapping and Difference Mapping: CP=(Measured) Closure Phase; Vis=(Measured) Visibilities; DM=Dirty Map; CM=Clean Map; CC=Clean Components; DB=Dirty Beam; CB=Clean Beam; MM=Model Map; RM=Residual Map; DFT=Discrete Fourier Transform

c) Bandwidth Smearing (see chapter 2.2) may influence the fringe visibility estimations and disturb proper mapping (may be related to the prior item).

d) Composite spectrum binaries are challenging because the brightness distribution depends not only on position but also on wavelength.

The items b) to d) may apply for Capella. For λ Vir only item d) may apply. Therefore we expect a better convergence behaviour for λ Vir which is what we observed in our mapping approaches. To accelerate the convergence of the Capella maps, one may also set clean windows to limit cleaning of the map to the positions of the most significant features. Since we are starting with null phases, which is equivalent to a point source model, a typical behaviour is that most of the power is concentrating in the origin of the uv-plane first. After a few dozen iterations this power dispenses into strong features at the expected positions of the stars. Usually less significant features at other places will remain within the map. Setting clean windows around the main features will assist the convergence of the hybrid map.

Items a) and b) are solved best by increasing the coverage of the uv-plane. To estimate the influence of Bandwidth Smearing one may compute the CWT for a large number of scans, locate and recenter the center of the fringe in the individual scans and average all CWTs. This way noise will decrease and real signals add constructively as in the power spectrum. We simulated typical properties of CWTs which are affected by Bandwidth Smearing and found the most significant feature to be that in those CWTs the fringe power is smeared over a broader range in time. Using a reliable source model, the response of the CWT algorithm to this effect might be simulated and corrected. Since our averaged power spectra apparently did not show this characteristic fringe peak broadening we did not perform this correction.

One may also correct for d), the Composite Spectrum imaging problem. Simulations by (Hum01) showed that the quality of maps with stars of significantly different spectral types can be improved noticeably by introducing two different effective temperatures as additional fit parameters. Naturally, those temperatures must be assigned to specific regions within the map.

7.2 Results

Using the introduced mapping procedures we produced a large number of maps. Since the λ Vir data can be modeled as point sources without any significant residuals, only hybrid mapping seems to be a reasonable approach. For three of the four nights the uv-plane coverage is very poor which results in a huge, elliptical *CB*. Since the modeling in chapter 6.3 confirmed that the stars do not seem to move significantly over the four days of observation, we added all nights together and obtained a map which easily converges in CHM without any model assumptions (see figure 7.7).

Since Capella is clearly resolved by IOTA, we produced hybrid maps as well as difference maps of this object. The data obtained on individual nights with shorter baselines converges without any problems in CHM due to the simpler brightness distribution. To improve the coverage of the uv-plane, we rotated the uv-coordinates as described in section 2.8.1. The rotation of the binary components was carried out such that the components appear at the medial position $(dRA(t_{ref}), dDEC(t_{ref})) = (14.05, -41.86)$ mas. To confirm that the correction was successful, we repeated the model fit that was used to obtain table 6.2 and got the overall best-fit position $(dRA, dDEC) = (14.35, -40.94)$ mas with an appreciable improvement in the overall fit. Using this correction we obtained the hybrid map shown in figure 7.4 and the difference map in 7.5. Figure 7.3 shows a hybrid map using data from an individual night. For the interpretation of maps generated with this procedure we should keep in mind that the Aa-component rotates synchronously with the orbit whereas the brighter and smaller Ab-component rotates with a period of ≈ 8.64d (see chapter 4.2).

Details for all maps presented are given in tables 7.1 and 7.2. We measured the center of light position for each star to compare the positions of the stars within the maps with the fitted and the predicted positions (as given in table 6.2). All positions agree very well within expected errors due to the finite beam size. The given beam sizes equal twice the minor and major axes of the clean beam ellipse measured to the 50% contour. Also the intensity ratios, obtained by integrating over the area of the individual stars, are in agreement with the fitted intensity ratios. To estimate the sizes of the resolved stars in the maps we convolved uniform disk models with the clean beam and measured the response of those models to the stars within the map. To determine the error on these diameter estimations we performed a Brute Force Least Square Fit (Schlo). Especially for CHM the diameters are in good agreement with our modeling results as table 7.1 shows.
Such a comparison is important since the produced CHM does not depend on any initial model and therefore allows us to confirm our earlier results completely independently.

We confirmed the movement of the Capella giants along the $\approx 14^\circ$ arc covered by the five days of our November observation run in chapter 6.2. Attempts to map the movement of the stars using CHM on data of individual nights were not successful since the uv-plane coverage is too poor for most of the nights. Therefore we applied DFM using the same initial model for each night. In the initial map we placed the stars at a medial position and observed that the DFM algorithm corrects this model by adding components with positive intensity at the real position of the star. Simultaneously the algorithm adds δ functions with negative amplitude at the place of the stellar disks in the initial model. Since the size of the beam may change, it is difficult to compare the resulting difference maps directly. It is more promising to compare residual difference maps obtained by subtracting a convolution of the initial model with the CB from the DFM for each night. Figure 7.8 shows the residual difference maps for all five nights of our observation run in November 2002. Since in some maps the residuals are only 10% we see several noise features. The clockwise movement of the Aa component appears significantly in the lower right quadrant following the color sequence black $\rightarrow$ red $\rightarrow$ blue $\rightarrow$ green $\rightarrow$ magenta. Less significant (due to the shorter arc) appears the movement of the Ab components in the upper left quadrant.

Table 7.1: Properties of the generated maps of **Capella**. MJD=JD-2452500

Data from Night		Mapping	I_{Ab}/I_{Aa}	Stellar Diam. [mas]		Position [mas]		Ref. Pos. (Hum94)	
Date	MJD	Algorithm	Comp.	D_{Aa}	D_{Ab}	dRA	dDEC	dRA	dDEC
11/15/02	93.797 ... 94.042	CHM	1.67			15.33	−39.86	17.33	−39.72
11/12/02 ... 11/16/02	90.821 ... 95.034	CHM	1.72	9.2 ± 4.8	6.5 ± 3.0	14.95	−40.20	14.05	−41.86
11/12/02 ... 11/16/02	90.821 ... 95.034	DFM	1.70	10.3 ± 3.0	6.0 ± 3.8	15.05	−40.47	14.05	−41.86

Data from Night		Data	Mapping	Steps	Rot.	Beam Size	Figure
Date	MJD	Points	Algorithm			[mas]	
11/15/02	93.797 ... 94.042	123/122/123	CHM	75	no	6.8×3.7	7.3
11/12/02 ... 11/16/02	90.821 ... 95.034	336/287/328	CHM	80	yes	5.4×2.6	7.4
11/12/02 ... 11/16/02	90.821 ... 95.034	336/287/328	DFM	200	yes	5.4×2.6	7.5/7.6

Table 7.2: Properties of the generated maps of λ **Vir**. MJD=JD-2452500

Data from Night		Data Points	Mapping	Steps	Beam Size	I_{Ab}/I_{Aa}	Position		Figure
Date	MJD	N	Algorithm		[mas]		dRA [mas]	dDEC [mas]	
03/22/03 ... 03/24/03	219.852 ... 222.937	89/173/157	CHM	30	9.1×2.4	2.6	16.84	1.44	7.7

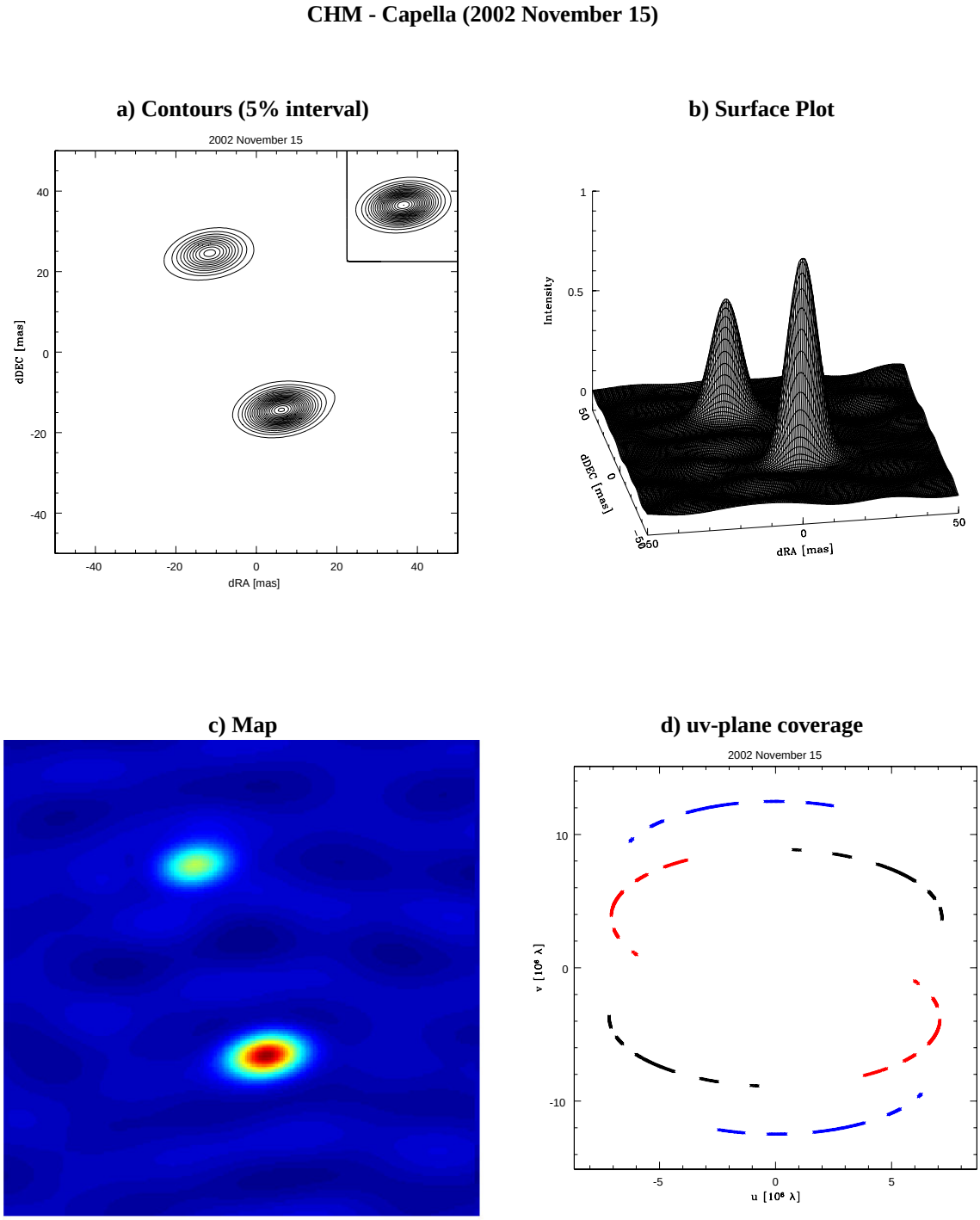

Figure 7.3: Hybrid map of Capella using the data from November 15, 2002. For more details see table 7.1. The different colors in the uv-plane plot correspond to the different baselines: Black=AC; Red=BC; Blue=AB.

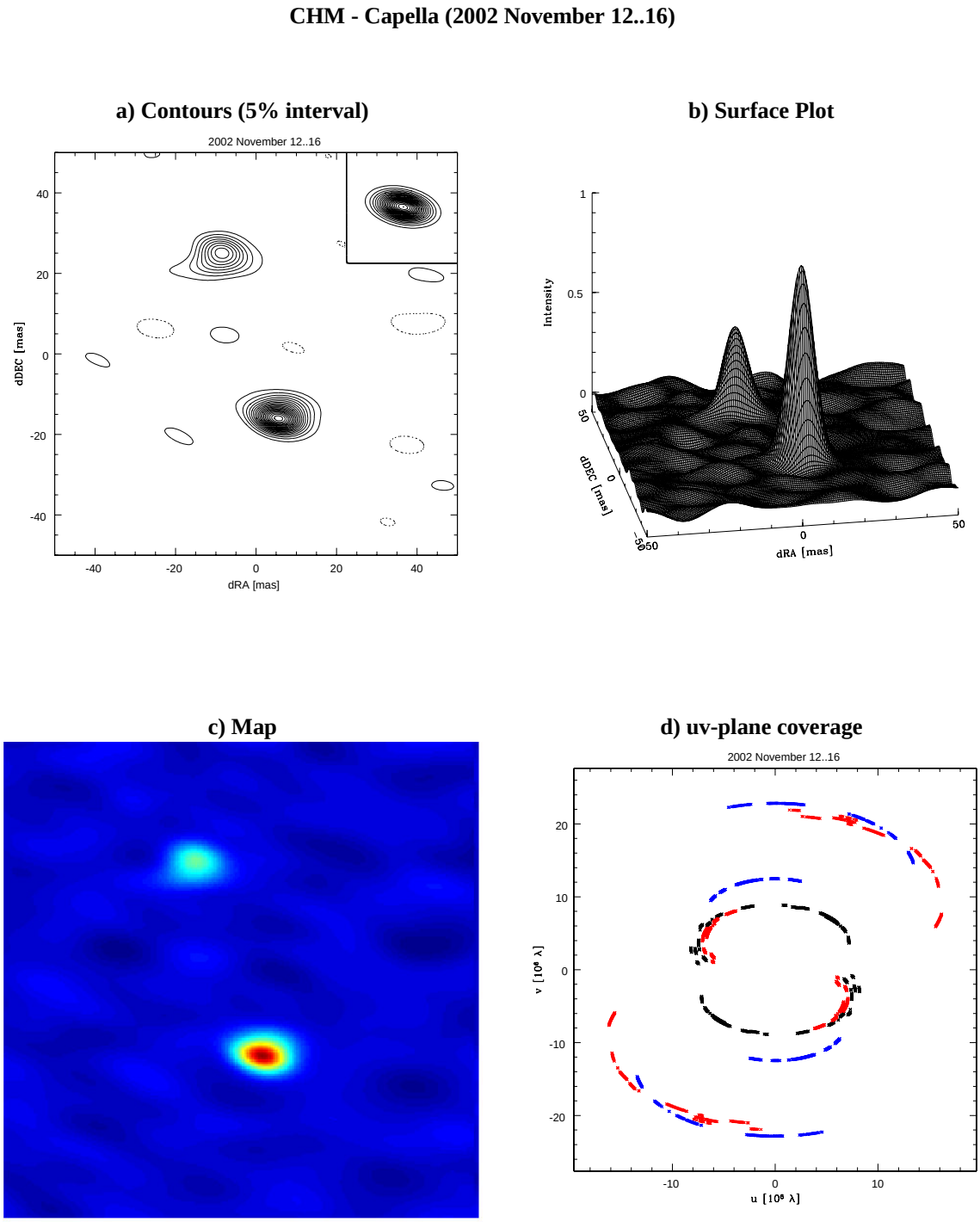

Figure 7.4: Hybrid map of Capella using the complete data from 2002 November 12..16. For more details see table 7.1. The different colors in the uv-plane plot correspond to the different baselines: Black=AC; Red=BC; Blue=AB.

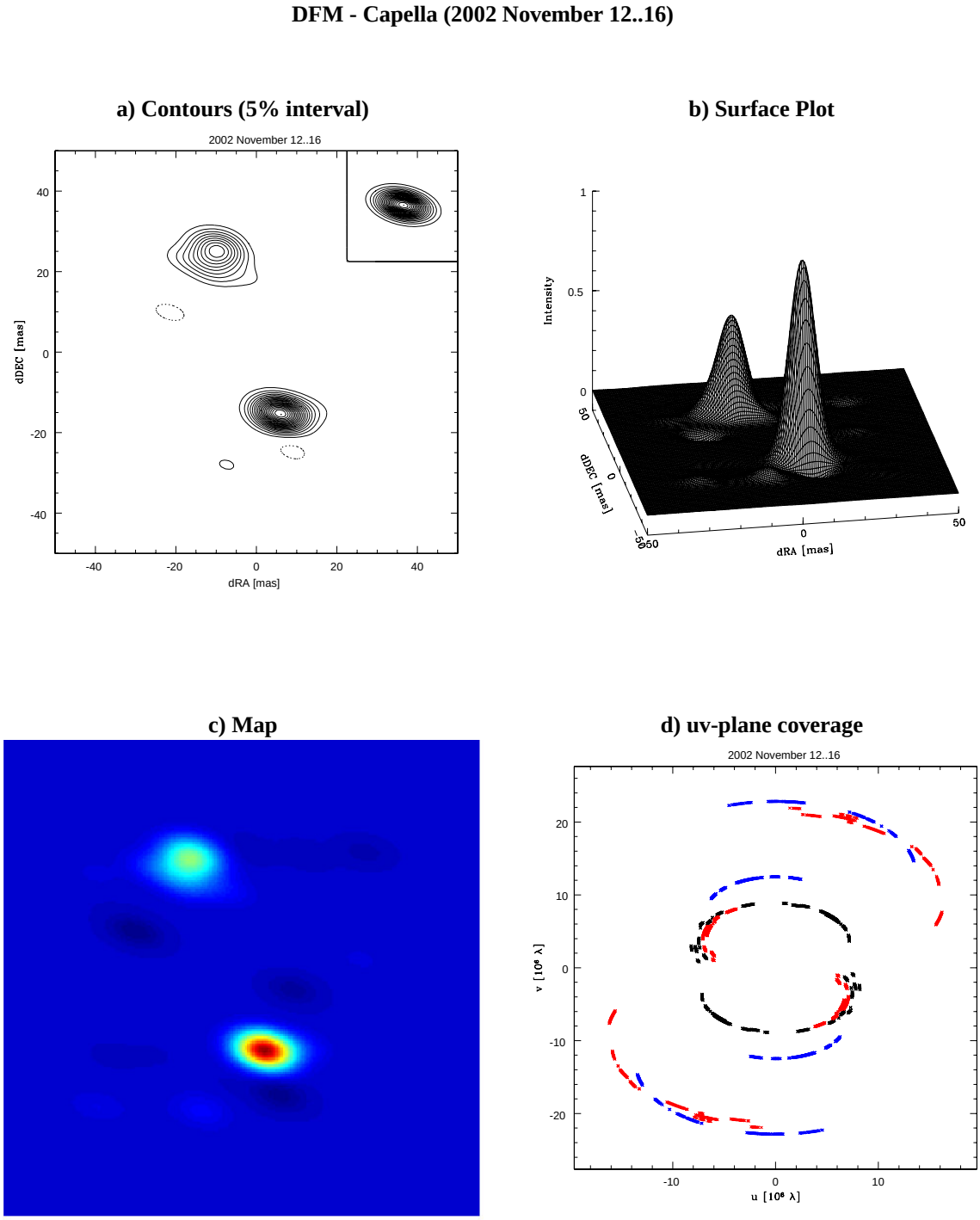

Figure 7.5: Difference map of Capella using the complete data from 2002 November 12..16. For more details see table 7.1. The different colors in the uv-plane plot correspond to the different baselines: Black=AC; Red=BC; Blue=AB.

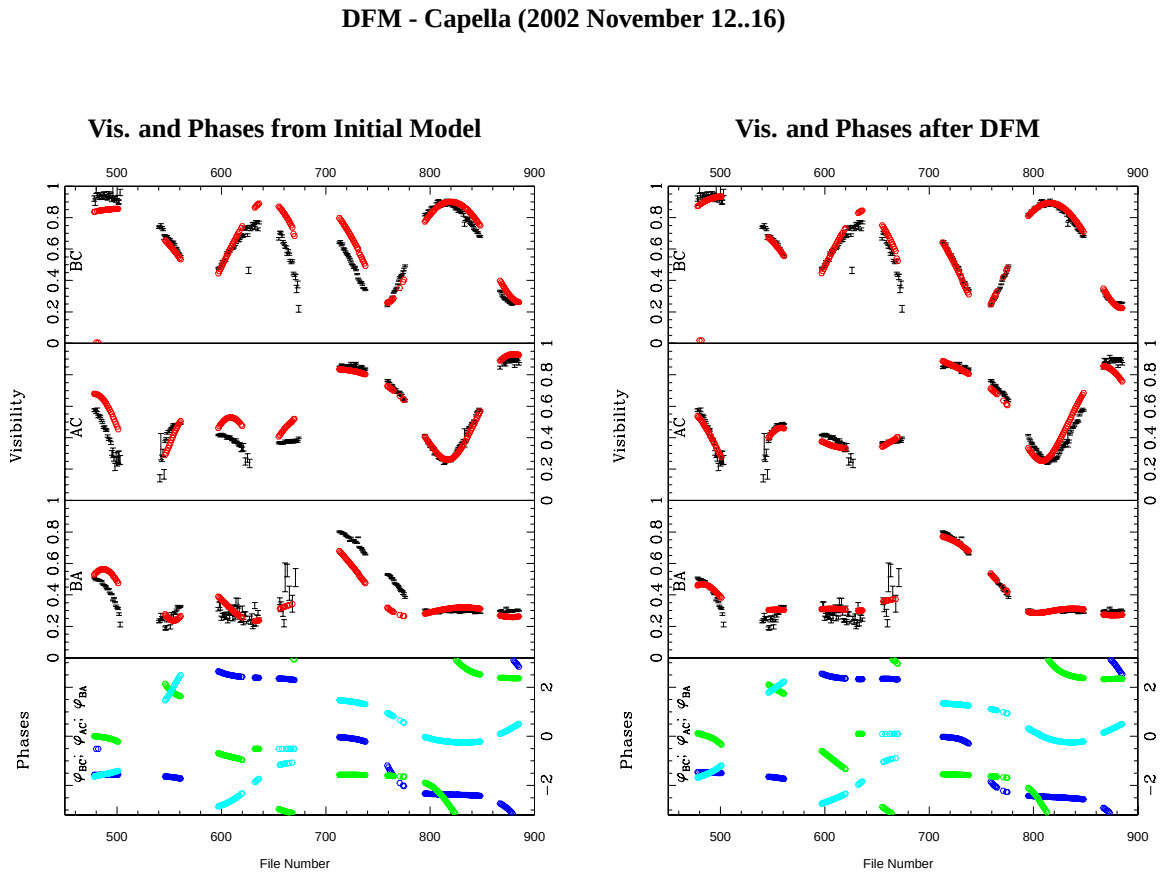

Figure 7.6: The initial model (left) and the corrected model (right) for the Difference map of Capella shown in fi gure7.5. The Self-Calibration process adjusted the phases φ_{BC} (blue), φ_{AC} (green) and φ_{BA} (cyan). Measured visibilities are black whereas the visibilities calculated from the MM are red.

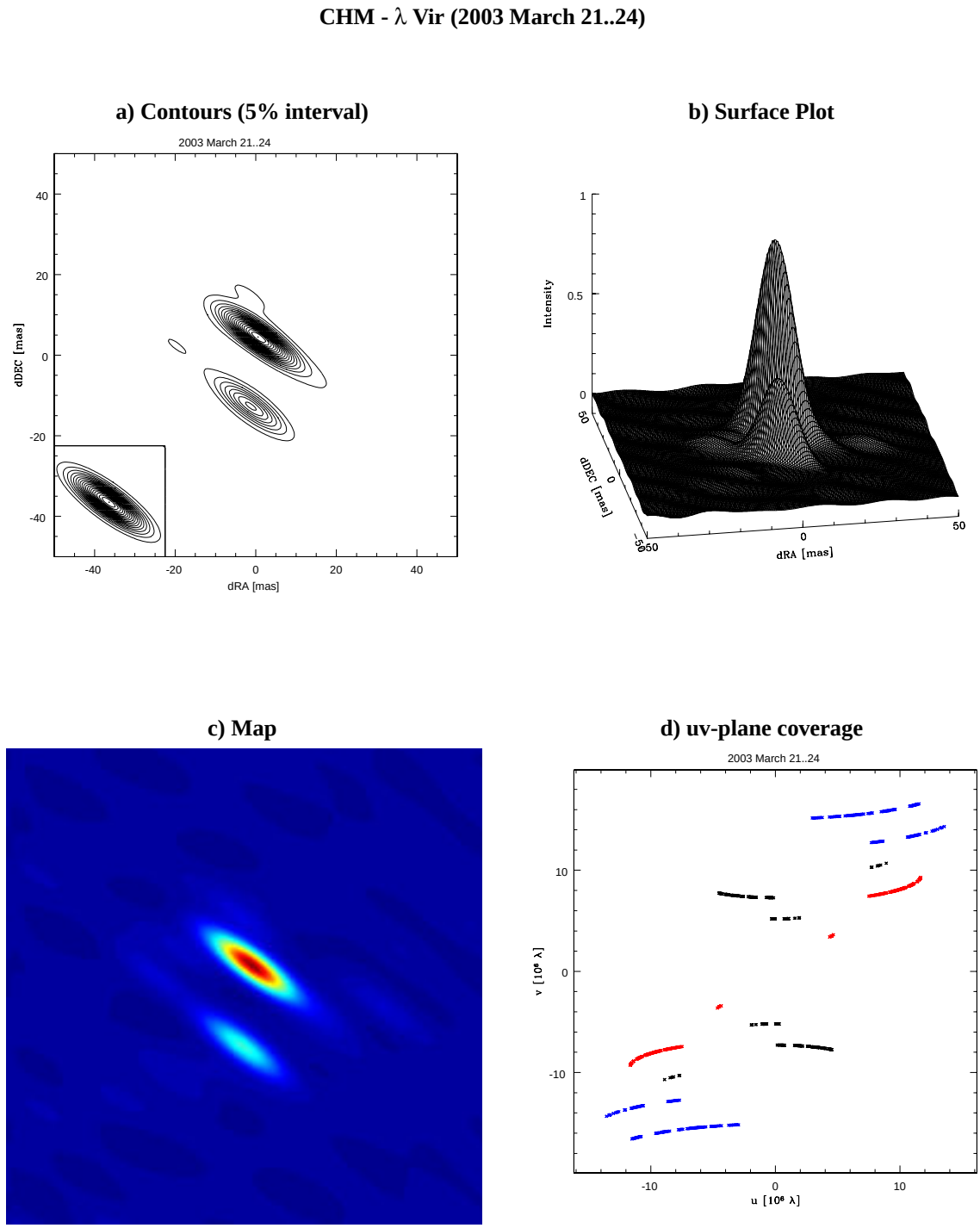

Figure 7.7: Hybrid map of λ Vir using the complete data from our observation run in 2003 March 21..24. For more details see table 7.1. The different colors in the uv-plane plot correspond to the different baselines: Black=BC; Red=AC; Blue=BA.

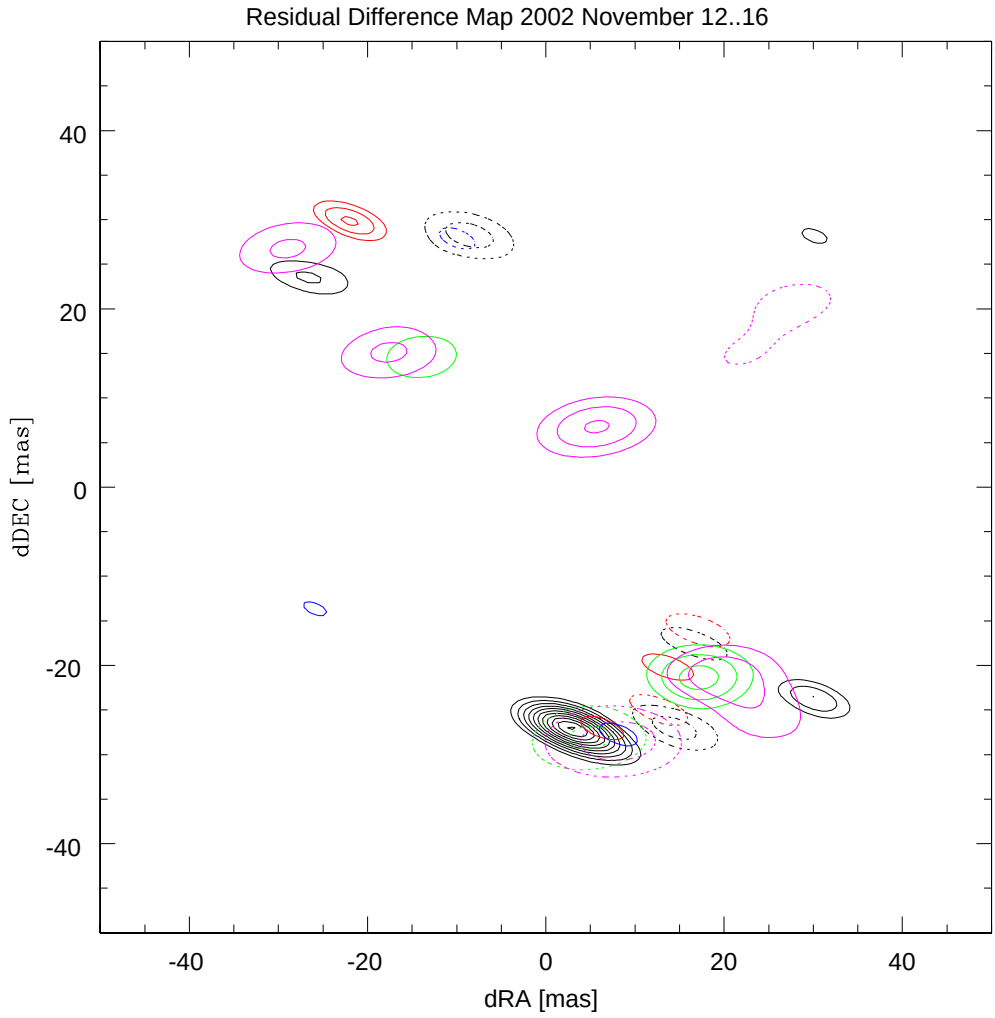

Figure 7.8: Superposition of residual difference maps for five individual nights. Each map was obtained using exactly the same initial model. To obtain the residuals between this initial model and the resulting difference map, we convolved the initial model with the CB and subtracted it from the final difference map. Following the used color sequence (Black: Nov12; Red: Nov13; Blue: Nov14; Green: Nov15; Magenta: Nov16) one can see the movement of the stars. Close to the position of the stellar disks in the initial model the DFM algorithm removed intensity by adding δ functions with negative amplitude.

Chapter 8

Remarks on the Performance of the IOTA Facility

To summarize our experience from both observation runs and our efforts for data reduction, we want to make the following remarks about the current performance of the IOTA observatory. In some cases we point out potential problems and make constructive suggestions for future improvements of this remarkable facility. Naturally we cannot incorporate most recent modifications which were carried out since our last observation run in March 2003.

- During an engineering period, the “resonance effect” should be investigated and eliminated if possible. We had found that the influence of this effect may be reduced with the development of algorithms other than the power spectrum method. But presumably all results obtained would improve when the resonance problem is eliminated.

- Arguably, the largest imbalance between the telescopes comes from an unequal positioning of the fibers on the camera-pixels. It is part of the IOTA-observation procedure to use the ”Fiber Explorer” software to maximize the flux on the PICNIC CCD-pixels. During the observation run in March 2003, we realized that a multiple repetition of this procedure during the night may improve the results significantly. So this could be an affect of temperature variations during the night. Also refraction will effect the alignment of the fibers on the camera. The refraction coefficient depends on the wavelength, so with changing altitude the star tracker will continue to track the optical position while the position

of the infrared peak on the CCD moves. In low-altitude observations, another way to get an inequality in the intensities from the different telescopes would be a reduction of the effective mirror area caused by partial occultation of the siderostats by the domes.

- Currently, the matrixfiles which are intended to be used to correct for those imbalances are inadequate for the requirements. Quite often the matrixfiles have to be rejected because the star tracker was not able to track the star correctly. A useful modification would be to include a data reduction algorithm into the data acquisition software. This algorithm should determine the flux ratio measured between the telescopes and recommend the observer to repeat the acquisition of the matrixfiles automatically if necessary. The computation time for such an algorithm is completely negligible.

- The fringe tracking algorithm based on the FFT could be replaced by a wavelet based algorithm. This may improve the performance especially in cases with bad SNR. The same holds for the function which allows to scan with the short delays for fringes. Since the computation of the CWT is more expensive than the computation of a single FFT, it must be examined if the current hardware equipment allows to run this CWT-algorithm on the IOTA site in real-time. The algorithm I implemented in the data reduction software is based on the computation of FFTs (Tor98) with an overall complexity of $O(N_{datafile} \cdot \log(N_{datafile}))$. There is a faster but also much more complex algorithm based on B-Splines (Muñ00) which follows $O(N_{datafile})$. Another very simple way to reduce the computation time is to narrow the range of computed scales close around the fringe.

- The filter algorithm presented in chapter 5.3.3 (see figure 5.12) could be implemented into the data acquisition software to present the user with the noise filtered signal on screen during acquisition. This would simplify the manual localization of the fringe and allow the user a better judgement of the quality of the data.

- A data reduction program should be installed on one of the computers on site to allow the observer to make a first appraisal of the quality of the data already during the observation run. This could help judging the extent to which extend an object is resolved and how good the closure phase measurements for this object are. In particular, the second point seems to be a limiting factor for the aperture synthesis capabilities of the instrument. Typically estimations of fast changing closure phases show large errors. So it would be better to adjust the number $N_{datafile}$ if the closure phase is changing very rapidly or to split datafiles later during the data reduction process to improve the closure phase estimations.

Chapter 9

Conclusions

The goal of my Masters project was to develop a general data reduction procedure for IOTA interferograms, to confirm the stability of the instrument and to give IOTA the capability of imaging. Since the development of a reliable data reduction procedure would have a huge influence on the other two tasks, I placed the highest emphasis on a proper visibility and closure phase estimation and implemented two different algorithms beyond the current standard routine. Both approaches provide remarkably similar results and each seem to be superior for different tasks.

The Fringe Envelope Fitting seems to be superior for less resolved objects and may be used for the estimation of stellar diameters as demonstrated for the resolved calibrators α Cas and α Lyn in chapter 6.2. For α Cas the result agrees well with earlier published works, whereas the α Lyn fit is based on only one measurement and seems to be affected by the worse conditions of this one measurement.

The CWT approach provides excellent results for low visibilities and we used those for model fits which resulted in high precision positions of the Capella giants, confirming earlier published orbital elements. In addition, we measured the diameters and the intensity ratio of the components for the first time in the H band. Those results are also in excellent agreement with other diameter measurements and the intensity ratio extrapolated from observations at shorter wavelengths. Based on the above we derived physical parameters like the densities and effective temperatures of the individual components.

Finally, we presented maps of the binary stars Capella and λ Vir. By performing a coordinate transformation we were able to compensate for the revolution of the Capella components during our observation run using the known orbit. The resulting map has excellent resolution and a beam size of just a few mas. For mapping

we used the Difference Mapping strategy which was previously used by (You99) for imaging purposes at optical and infrared wavelengths. Beside reaching this milestone for the IOTA facility we were also able, as far as known, to construct the first infrared maps based on the completely model independent Hybrid Mapping strategy.

The point of the Capella campaign was to image an object with known properties to demonstrate that the IOTA is a capable imaging instrument. We have also gone beyond this basic objective by imaging the λ Vir system for the first time. The disks of those stars are not resolved by IOTA but it will be straight forward to include other observations by the IOTA collaboration to obtain an orbit. We measured the position and intensity ratio of both components for the observed epoch and generated hybrid maps. Since we did not measure any significant movement of the components over the four-day observation period, we can reject the possibility that the 1.93017d period reported by (Abt61) and (Tok97) represents the orbital period of the observed $\approx$ 20mas separated close binary system.

Within chapter 8 we made general remarks on the current performance of the IOTA observatory and confirmed that IOTA is able to measure visibilities with a precision of the order of 5% and better. To enhance this performance we presented in section 5.4 an algorithm to correct for potential imbalances between the telescopes. The proper behavior of this correction must still be demonstrated since the quality of our matrix-files was not adequate for this purpose. The precision of the measured closure phases is of the same order even if fast changing phases are problematic.

Going ahead from this point, IOTA is one of the few facilities with imaging capabilities which may be used for further studies of close or interacting multiple stars or for the imaging of stellar surfaces and disk features around young stellar objects (YSO).

A - Observation Logs

Table 9.1: Observation Log November 2002.

Date [UT]	Time [UT] of first data acquisition	Hour Angle [h]	Source	Filter	No. of data file (without matrix file)s
BASELINE: A=ne35, B=se15, C=ne0					
11/11/02	06:03	1.32	α Cas	H	0-1
	08:00	-1.32	Capella	H	6-7
	08:34	-1.47	β Aur	H	12-13
	10:57	1.63	Capella	H	18-51, 56-60
	11:58	1.94	β Aur	H	61-68
	13:08	3.82	Capella	H	73-77
11/12/02	05:41	1.03	α Cas	H	0-7
	07:43	-1.54	Capella	H	11-31
	09:11	-0.78	β Aur	H	36-43
	10:11	0.94	Capella	H	48-75
	11:15	1.28	β Aur	H	80-89
	12:00	2.76	Capella	H	94-110
	13:22	3.41	β Aur	H	115-119
11/13/02	03:58	3.35	α Cyg	H	0-16
	04:51	0.25	α Cas	H	21-33
	06:42	-3.20	δ Aur	H	38-47
	07:19	-1.87	Capella	H + 25%-ND	52-78
	08:22	-1.53	β Aur	H	83-92
	09:09	-0.04	Capella	H + 25%-ND	97-117
	10:08	0.24	δ Aur	H	122-132
	10:45	1.57	Capella	H	137-161
	11:42	1.80	β Aur	H	166-175
	12:20	2.44	δ Aur	H	180-189
	13:14	-0.02	α Lyn	H	198-207
11/14/02	02:23	1.83	α Cyg	H	0-12
	04:08	3.58	α Cyg	H	17-26
	04:44	0.20	α Cas	H	31-40
	05:25	-1.60	κ Per	H	(45)50-54
	05:51	-3.27	Capella	H + 25%-ND	59-84
	06:54	-2.94	β Aur	H	89-98
	07:34	-2.27	δ Aur	H	102-116
	08:24	-0.72	Capella	H + 25%-ND	121-142
	09:17	-0.55	β Aur	H	147-158
	09:52	0.03	δ Aur	H	163-173
	10:25	1.30	Capella	H + 25%-ND	178-217
	11:37	1.79	β Aur	H	222
	12:06	2.98	Capella	H + 25%-ND	236-255
	13:04	3.25	δ Aur	H	260-269

Table 9.2: Continue: Observation Log November 2002.

Date [UT]	Time [UT] of first data acquisition	Hour Angle [h]	Source	Filter	No. of data file (without matrix files)
BASELINE: A=ne15, B=se15, C=ne0					
11/15/02	06:45	2.30	α Cas	H	(0)10-15
	07:08	3.36	Capella	H + 25%-ND	20-45
	07:59	-1.07	|	1.65μ-ND	50-61
	08:21	-0.70	|	H	66-83
	08:59	-0.79	δ Aur	H	88-97
	09:28	0.42	Capella	H + 25%-ND	102-155
	11:04	1.30	δ Aur	H	160-169
	11:34	2.51	Capella	H + 25%-ND	174-192
	12:08	3.09	|	1.65μ-ND	197-215
	12:50	3.80	|	H + 25%-ND	220-226
	13:19	3.56	δ Aur	H	231-238
11/16/02	08:14	-1.47	δ Aur	H	0-13
	09:12	0.21	Capella	H + ND	18-63
	11:07	1.42	β Aur	H	68-81
	11:45	2.05	δ Aur	H	86-100
	12:22	3.39	Capella	H + ND	105-122
	13:05	3.39	δ Aur	H	127-137

Table 9.3: Observation Log March 2003.

Date [UT]	Time [UT] of first data acquisition	Hour Angle [h]	Source	Filter	No. of data file (without matrix files)
BASELINE: A=ne35, B=se7, C=ne25					
03/21/03	07:32	0.71	δ Crt	H	0-20
	08:18	-1.59	HD126035	H	25-27
	08:27	-1.36	λ Vir	H	32-40
	09:05	-0.81	HD126035	H	45-47
	09:15	-0.57	λ Vir	H	52-55
	10:21	0.47	HD126035	H	60-64
BASELINE: A=ne35, B=se7, C=ne10					
03/22/03	04:40	1.77	β CMi	H	0-25
	05:47	-0.99	δ Crt	H	30-47
	06:23	0.77	λ Hya	H	52-64
	06:48	0.04	δ Crt	H	69-80
	08:11	-1.63	HD126035	H	85-88
	08:31	-1.23	λ Vir	H	93-98
	08:41	-1.13	HD126035	H	103-107
	08:54	-0.86	λ Vir	H	112-113
	09:25	-0.33	|	H	118-144
	09:56	0.12	HD126035	H	149-158
	10:29	0.74	λ Vir	H	163-182
	10:55	1.11	HD126035	H	187-195
	11:59	-0.91	HD158352	H	200-215
	12:32	-0.45	HD159170	H	220-227
	12:50	-0.06	HD158352	H	232-239

Table 9.4: Continue: Observation Log March 2003.

Date [UT]	Time [UT] of first data acquisition	Hour Angle [h]	Source	Filter	No. of data file (without matrix files)
BASELINE: A=ne35, B=se15, C=ne10					
03/23/03	03:23	2.01	δ Aur	H	0-8
	03:59	2.44	HR2152	H	13-17
	04:19	2.94	δ Aur	H	22-27
	04:40	3.12	HR2152	H	32-37
	05:35	1.06	75 Cnc	H	42-50
	06:06	1.60	HR3621	H	55-60
	06:32	2.01	75 Cnc	H	65-70
	06:55	2.42	HR3621	H	75-79
	07:45	1.06	δ Crt	H	84-89
	08:51	-0.91	HD126035	H	95-98
	09:00	-0.68	λ Vir	H	103-107
	09:09	-0.60	HD126035	H	112-115
	09:27	-0.23	λ Vir	H	120-128
	09:41	-0.07	HD126035	H	133-135
	09:48	0.13	λ Vir	H	140-163
	10:15	0.50	HD126035	H	168-171
	10:35	0.83	"	H	176-178
	10:43	1.03	λ Vir	H	183-198
	11:01	1.27	HD126035	H	203-210
	11:57	-0.84	HD157856	H	215-219
	12:08	-0.71	HD158352	H	224-233
	12:35	-0.33	HD159170	H	238-244
	12:56	0.10	HD158352	H	248-254
03/24/03	03:11	1.87	δ Aur	H	0-5
	04:15	3.66	Capella	H	10-32
	06:17	-0.34	δ Crt	H	37-41
	06:24	-0.22	"	H	46-48
	06:41	0.05	"	H	53-68
	07:24	-2.29	HD126035	H	73-77
	07:52	-1.76	λ Vir	H	81-104
	08:20	-1.35	HD126035	H	109-113
	08:43	-0.90	λ Vir	H	118-143
	09:16	-0.43	HD126035	H	148-152
	09:37	0.00	λ Vir	H	161-183
	10:05	0.40	HD126035	H	188-191
	10:13	0.61	λ Vir	H	196-212
	10:35	0.90	HD126035	H	217-222
	11:03	-1.52	41 Oph	H	227-231
	11:09	-1.42	"	H	235-239
	11:31	-1.25	HD158352	H	244-262
	12:17	-0.43	HD157856	H	267-271
	12:30	-0.27	HD158352	H	276-301

B - Data Reduction Software Manual

We provide a brief overview about the functionality of the developed data reduction software. All programs are written for Linux gcc and allow the complete data reduction as presented in this thesis. The software package consists of three applications which are normally used in the following order:

IDRS: Estimates the visibilities and closure phases from the IOTA data files and writes them into an output file.

ModelBin: Fits binary models to the IDRS output file.

Map: Produces maps from the IDRS output files and allows to analyze those maps.

The programs are developed for functionality and are not consequently optimized with respect to the computation time. When used to process data for publication, we ask to give credit to this thesis. In the following we present the different programs in more detail.

B.1 IDRS - Interferometry Data Reduction Software

IDRS estimates visibilities and closure phases using one of the three presented algorithms. To select which algorithm is used and to enable different corrections, there is a declaration section within the program file `idrs.c` that contains beside others the following parameters:

`fitampmethod`: Selects the algorithm for visibility estimation.

`docalib`: Enables the imbalance correction using the matrix files.

`dobiascorr`: Enables the BIAS correction for the fringe envelope fitting algorithm as formalized in equation (5.6).

`simfringe`: Generates simulated fringes instead of using the data. Further parameters must be set within the code.

`calibmethod`: Allows to switch between averaging of the transfer function over the whole night and the interpolation with equation (5.3).

`doplot1..3`: Enables up to three PGPLOT windows which show detailed plots during the data reduction process. These options may be set for debugging and confirming the correct performance of the algorithms.

`repdetails`: Reports details of the running process on screen.

`repfiles`: Writes several report and debugging files on disk. Those files may be used to generate miscellaneous plots with SM or MATLAB.

`filterdata`: Filters the obtained visibility and closure phase data using different error thresholds and scattering criteria.

The declaration section is grouped into subsections where all parameters are collected that affect the performance of the different algorithms. The user may check out those sections for finetuning. After setting those parameters and compiling the code, the user must generate a text file which lists the location of the IOTA data file on the local hard disk. The following file `nov02.ini` may be used as example:

```
/home/skraus/iota/Data/
0 /home/skraus/iota/Data/2002Nov15/ 0 0 0 0
0 /home/skraus/iota/Data/2002Nov16/ 1 2 50 200
```

Using this file, IDRS will assume that `/home/skraus/iota/Data/` (called [DataRootDir]) contains further initiation files and will process all data files in directory `/home/skraus/iota/Data/2002Nov15/` and scans 50 to 200 within the files `iota1.data` and `iota2.data` in the directory `/home/skraus/iota/Data/2002Nov16/`.

The initiation files assumed in [DataRootDir] are text files named `objid.ini` and `sre.ini`. `objid.ini` correlates the Object Designations in the IOTA header files with the IDRS intern pure numerical object ID, for example

```
13Alp_Aur -> ID 1
34Bet_Aur -> ID 2
33Del_Aur -> ID 3
18Alp_Cas -> ID 4
40Alp_Lyn -> ID 5
27Kap_Per -> ID 6
50Alp_Cyg -> ID 7
```

The file `sre.ini` specifies which of those objects serves as calibrator and which may be used as target for stellar radius estimation (SRE) as described in chapter 6.2. Objects which are targets but not used for SRE are not listed! The file may look like

```
Calibrators: 2 3 6 7
Targets: 4 5
Diameters: 4.68 6.46
```

The program runs through a cycle which consists of the reduction of the matrix files, the visibility estimation, the closure phase estimation and the SRE which is followed by the filtering of the data. The program itself can be started using different command line parameters to skip some of those stations assuming that the earlier cycles were already processed

`./idrs comp -f nov02.ini`: Performs the complete data reduction cycle as described above on the data specified in the initiation file `nov02.ini`.

`./idrs vis -f nov02.ini`: Starts the cycle with the visibility estimation.

`./idrs cp -f nov02.ini`: Starts the cycle with the closure phase estimation.

`./idrs sre 4 -f nov02.ini`: Performs only the SRE on the object with ID 4 and finishes with the filtering step.

The major output file of IDRS which is processed by the other applications is called `vis.dat` and includes all measured visibility and closure phase data.

B.2 ModelBin - Fitting Binary Models

This application models visibilities and closure phases for binary sources and applies a least square fit to the IDRS output file. The file `general.h` defines with the parameters `MJDfrom`, `MJDto` and `target_id` which object should be fitted and what's the temporal window for the fit (MJD=JD-2452500). Important parameters for the fit are `weightfunc1` and `weightfunc2` which correspond to the parameters W_V and W_Φ in chapter 6. `max_guess` and `step_guess` determine what the sizes of the initial guess grid and its spacing are. With `Iratio_from`, `Iratio_to` and `Iratio_step` one may perform the fit for a whole range of intensity ratios. This will produce the output file `intratio.dat`. Starting the program with the command line parameter `./modelbin intratio` a parabola is fitted to the obtained $\chi^2(I_2/I_1)$ ratios and the application will provide the best fit intensity ratio with an error estimation.

To perform a diameter fit of the disks as well, one has to fix the positions of the stars with `fitdiameter_dRA`, `fitdiameter_dDEC` and enable this fit with the option `fitdiameter`.

The program can also be used to rotate the (u,v) plane as described in chapter 2.8.1. The corresponding orbital elements have to be set in the file `model.c` and the rotation itself is performed with `./modelbin rotate`. The rotated (u',v') coordinates are written within the file vis.dat such that `map` will use the rotated data for mapping. To restore the unrotated data one can just copy the file `visnorot.dat` to `vis.dat`.

B.3 Map - Mapping Software

Our Mapping Software uses the DFT and is therefore quite inefficient for large data files. The map is produced for the object and with data within the temporal window as defined in `general.h`. Important parameters within the declaration section are `clean_gain` and `max_cleansteps` which specify the gain and the number of clean steps performed in each CLEAN cycle (reasonable values are 0.02 as gain and 400 cleansteps for CHM or 20 cleansteps for DM). Beside that the user may choose between two rectangular or two circular clean windows by setting `clean_window_type`. `hybridsteps` determines how many CHM or DM steps are performed before the iteration ends. For CHM one may use `use_model_vis`, `use_model_phase` and `use_model_phase_guess` either to use only modeled visibility and closure phase data or to use the model phases from `modelbin` as initial guess for the hybrid map on the real data. For DM the parameters `model_I1`, `model_I2`, `model_dRA`, `model_dDEC`, `model_R1` and `model_R2` must be set.

The dimensions of the maps in pixels are set with `size_x` and `size_y` where the conversion factor from pixel to mas is given by `spacing`. To start mapping the application is started with `./map hybrid` or `./map diff`. The iteration can be interrupted by the user to end mapping or to relocate the clean windows, which is done directly in the PGPLOT window. The final maps are named `map.dat` and `mapbeam.dat` where the latter contains the beam in the corner of the map. The output format is float binary with two integers in the beginning of the file giving the dimensions along both axes.

After a map is generated successfully, it may be analyzed running `./map analyse`. This part of the program allows to select two regions. After this selection the fluxes within those regions and the center of light-positions are calculated. With `./map center` one may center one star or the center of light in the middle of the map. The output file with centered star is called `cenmap.dat`. Analogous performs the command `./map diameter` a convolution of a uniform disk model with the dirty beam (from file `db.dat`) and measures the response to a star in the map `map.dat`. This routine generates a output file with the χ^2 values for different diameters which may be used by `./modelbin intratio` to obtain the best-fit diameter and its error by performing a Brute Force Fit.

Bibliography

[Abt61] ABT, H.: "The Frequency of Binaries among Metalmc-Line Stars."
ApJ Supp. 6, pp37-74 (1961)

[Alo99] ALONSO, A.; ARRIBAS, S.; MARTINEZ-ROGER, C.: "The effective temperature scale of giant stars (F0-K5)"
Astron. Astrophys. Suppl. Ser. 140, 261-277 (1999)

[And20] ANDERSON, J. A.: "Application of Michelson's interferometer method to the measurement of close double stars"
ApJ 51, pp263 (1920)

[Bal96] BALDWIN, J. E.; BECKETT, M. G.; BOYSEN, R.C.; BURNS, D.; BUSCHER, D. F.; COX, G. C.; HANIFF, C. A.; MACKAY, C. D.; NIGHTINGALE, N. S.; ROGERS, J.; SCHEUER, P. A. G.; SCOTT, T. R.; TUTHILL, P. G.; WARNER, P. J.; WILSON, D. M. A.; WILSON, R. W.: "The first images from an optical aperture synthesis array: mapping of Capella with COAST at two epochs"
A&A 306, L13-L16 (1996)

[Bel89] BELL, R. A.; GUSTAFSSON, B.: "The effective temperatures and colours of G and K stars"
Mon. Not. R. astr. Soc. 236, pp653-708 (1989)

[BelTh] BELLE, G. VAN; THOMPSON, R. R.: "Astronomical Interferometry in the Optical and Infrared"
Scriptum

[Bor02] BORDÉ, P.; DU FORESTO, V. C.; CHAGNON, G.; PERRIN, G.: "A catalogue of calibrator stars for long baseline stellar interferometry"
A&A 393, 183-193 (2002)

[Bri00] BRICKHOUSE, N. S.; DUPREE, A. K.; EDGAR, R. J.; LIEDAHL, D. A.; DRAKE, S. A.; WHITE, N. E.; SINGH, K. P.: "Coronal Structure and Abundances of Capella from Simultaneous EUVE and ASCA Spectroscopy"
ApJ, 530, I1, pp387-402 (2000)

[Bus88] BUSCHER, D. F.: "Optimizing a ground-based interferometer for sensitivity at low light levels"
Mon. Not. R. astr. Soc. 235, pp1203-1226 (1988)

[Bus90] BUSCHER, D. F.; HANIFF, C. A.; BALDWIN, J. E.; WARNER, P. J.: "Detection of a bright feature on the surface of Betelgeuse"
Royal Astronomical Society, Monthly Notices, 245, pp7-11 (1990)

[Car96] CARROLL, B. W.; OSTLIE, D. A.: "An Introduction to Modern Astrophysics"
Addison-Wesley Publishing Company, Inc. (1996)

[Cam1899] CAMPBELL, W. W.: "The spectroscopic binary Capella"
ApJ 10, 177 (1899)

[Cha96] CHA, G.; GONG, Z.; XU, J.; ZHAO, Z.: "High Resolution $H\alpha$ and Ca II K Spectroscopic Observations of Capella and the Analysis"
PASP 108, pp594-602 (1996)

[Dav00] DAVIS, J.; TANGO, W. J.; BOOTH, A. J.: "Limb-darkening corrections for interferometric uniform disc stellar angular diameters"
Monthly Notices RAS 318, Issue 2, pp387-392 (2000)

[deS03] DE SOUZA, A. D.; KERVELLA, P.; JANKOV, S.; ABE, L.; VAKILI, F.; FOLCO, E. DI; PARESCE, F.: "The spinning-top Be star Achernar from VLTI-VINCI"
preprint: astro-ph/0306277

[duF96] DU FORESTO, V. C.; PERRIN, G.; MARIOTTI, J.-M.; LACASSE, M.; TRAUB, W.: "The FLOUR/IOTA Fiber Stellar Interferometer"
Astrofib: Integrated Optics for Astronomical Interferometry, pp115-125 (1996)

[DiB91] DI BENEDETTO, G. P.; BONNEAU, D.: "Near-infrared observations of Capella by Michelson interferometry"
A&A 252, pp645-650 (1991)

[Gub91] GUBOCHKIN, A. N.; MIROSHNICHENKO, A. S.
Kin. and Phys. of Cel. Bodies, 7, 59 (1991)

[Hes97] HESTROFFER, D.: "Centre to limb darkening of stars"
A&A 327, pp199-206 (1997)

[Hub03] HUBIN, N.; ARSENAULT, R.; KASPER, M.: "ESO Press Release 11/03: Sharper and Deeper Views with MACAO-VLTI"
from http://www.eso.org/outreach/press-rel/pr-2003/pr-11-03.html (2003)

[Hof82] HOFFLEIT, E. D.; WARREN JR. W. H.: "Yale Bright Star Catalog (5th revision)"
(1982)

[Hum94] HUMMEL, C. A.; ARMSTRONG, J. T.; QUIRRENBACH, A.; BUSCHER, D. F.; MOZURKEWICH, D.; ELIAS II, N. M.; WILSON, R. E.: "Very high precision orbit of Capella by long baseline interferometry"
ApJ 107, No. 5 (1994)

[Hum95] HUMMEL, C. A.; ARMSTRONG, J. T.; BUSCHER, D. F.; MOZURKEWICH, D.; QUIRRENBACH, A.; VIVEKANAND, M.: "Orbits of small angular scale binaries resolved with the Mark III Interferometer"
ApJ 110, No. 1 (1995)

[Hum01] HUMMEL, C. A.: "Applied Binary Research"
Michelson Interferometry Summer School, Viewgraphs (2001)

[Joh02] JOHNSON, O.; DRAKE, J. J.; KASHYAP, V.; BRICKHOUSE N. S.; DUPREE, A. K.; FREEMAN, P.; YOUNG, P. R.: "The Capella Giants and coronal evolution across the Hertzsprung Gap"
ApJ 565, L97-L100 (2002)

[Kri90] KRISCIUNAS, K.; GUINAN, E.: "Photometry of Capella"
Information Bulletin on Variable Stars, 3548, 1. (1990)

[Lüh01] LÜHE, OSKAR VON DER: "Interferometrie in der Astronomie"
Scriptum, Albert-Ludwig-Universität Freiburg (2001)

[Mas99] MASSI, M.; AARON, S.: "Hybrid mapping in VLBI and spurious symmetrization"
A&A 136, pp211-216 (1999)

[Mic1891] MICHELSON, A. A.: "Measurement of Jupiters satellites by interference"
Nature 45, pp160 (1891)

[Mil99] MILLIAN-GABET, R.: "Investigation of Herbig Ae/Be stars in the near-infrared with a long baseline interferometer"
Dissertation at UMass, Amherst (1999)

[Mon01] MONNIER, J. D.: "Asymmetric Beam Combination for Optical Interferometry"
PASP 113, pp639-645 (2001)

[Muñ00] MUÑOZ, A.; ERTLÉ, R.; UNSER, M.: "Fast Continous Wavelet Transform Based on B-Splines"
Biomedical Imaging Group, Swiss Federal Institute of Technology Lausanne (2000)

[Nog81] NOGUCHI, K.; KAWARA, K.; KOBAYASHI, Y.; OKUDA, H.; SATO, S.: "Near-Infrared Photometry of Carbon Stars"
Publ. Astron. Soc. Japan 33, 373-397 (1981)

[Pan98] PANT, P.; STALIN, C. S.; SAGAR, R.: "Microthermal measurements of surface layer seeing at Devasthal site"
A&A Suppl 136, pp19-25

[Pedre] PEDRETTI, E.; MILLAN-GABET, R.; MONNIER, J. D.; TRAUB, W. A.; CARLETON, N. P.; BERGER, J.-P.; LACASSE, M. G.: "CPLD-Controlled PICNIC Camera at IOTA"
Technical Memorandum: http://cfa-www.harvard.edu/cfa/oir/IOTA/PUBLI/MEMOS/ms.pdf

[Pou03] POURBAIX, D.; BOFFIN, H. M. J.: "Reprocessing the Hipparcos Intermediate Astrometric Data of spectroscopic binaries"
A&A 398, 1163-1177 (2003)

[Pre92] PRESS, W.; TEUKOLSKY, S.; VETTERLING, W.; FLANNERY, B. et al: "Numerical Recipes in C"
Cambridge University Press (1992)

[Rar] RAROGIEWICZ, LU: "MWO Hooker Telescope: the 20-foot Interferometer"
from http://www.mtwilson.edu/Tour/100inch/20ftI/

[Ric02] RICHICHI, A.; PERCHERON, I.: "CHARM: A Catalog of High Angular Resolution Measurements"
A&A 386, 492-503 (2002)

[Schlo] SCHLOERB, F. P.: "Data, Errors and Model Fitting"
Scriptum

[Sch93] SCHLOERB, F. P.: "Imaging Interferometry: Lessons from the ground"
SPIE 1947, pp249-260 (1993)

[Sha92] SHAO, M.; COLAVITA, M. M.: "Long-baseline optical and infrared stellar interferometry"
Ann. Rev. A&A 30, pp457-498 (1992)

[Simbad] SIMBAD Astronomical Database
Centre de Données astronomiques de Strasbourg

[Str01] STRASSMEIER, K. G.; REEGEN, P.; GRANZER, T.: "On the rotation period of Capella"
Astron. Nachr. 332, pp115-124 (2001)

[Tok97] TOKOVININ, A. A.: "MSC - a catalogue of physical multiple stars"
A&A Suppl. 124, pp74-84 (1997)

[Tor98] TORRENCE, C.; COMPO, G. P.: "A Practical Guide to Wavelet Analysis"
Bulletin of the American Meteorological Society (1998)

[TorCo] TORRENCE, C.; COMPO, G. P.: "Wavelet Analysis & Monte Carlo"
http://paos.colorado.edu/research/wavelets/wavelet3.html

[Tra00] TRAUB, W. A. et al.: "The Third Telescope Project at the IOTA Interferometer"
SPIE 4006, pp715-722 (2000)

[Tra01] TRAUB, W. A.: "Delay Line Geometry (ver. 5: 4. Nov. 01)
Technical Memorandum: http://cfa-www.harvard.edu/cfa/oir/IOTA/PUBLI/MEMOS/wes.mc.pdf (2001)

[Tra02] TRAUB, W. A. et al.: "New Beam-Combination Techniques at IOTA"
Proc. of SPIE meeting on Astronomical Telescopes and instrumentation (2002)

[Col99] COLDWELL, C.: "IOTA Baseline Vector"
Technical Memorandum: http://cfa-www.harvard.edu/cfa/oir/IOTA/PUBLI/MEMOS/baseline.pdf (1999)

[Que02] QUELOZ, D.: "ESO Press Release 11/03: How Small are Small Stars Really?"
http://www.eso.org/outreach/press-rel/pr-2002/pr-22-02.html (2002)

[Qui01] QUIRRENBACH, ANDREAS: "Astronomical interferometry, from the visible to sub-mm waves"
Europhysics News 32 No. 6 (2001)

[Weiss] WEISSTEIN, E. W.: "Phase Closure Relations"
from http://scienceworld.wolfram.com/physics/PhaseClosureRelations.html

[Weg03] WEGENER, FRANZ: "Classical Electrodynamics"
Scriptum, Ruprecht-Karls-Universität Heidelberg (2003)

[Wil02] WILSON, EDWARD: "IOTA-Ames Fringe Tracking Status"
(2002)

[You99] YOUNG, J. S.: "Infrared Imaging with COAST"
Dissertation, St. John's College, Cambridge and Cavendish Astrophysics (1999)

[You02] YOUNG, P. R.: "Capella: Separating the Giants"
ApJ 565, pp598-607 (2002)